Rock Magnetic Studies of the CY-4 Drill Hole
Through the Troodos Ophiolite, Cyprus

By

Dawn-Ann Trebilcock

Submitted in partial fulfillment of the requirements for the degree of

Master of Science

November 2006

Supervisor: Dr. G.J. Borradaile

Department of Geology
Lakehead University
Thunder Bay, ON P7B 5E1

Your file Votre référence
ISBN: 978-0-494-21521-0
Our file Notre référence
ISBN: 978-0-494-21521-0

Abstract

Rock magnetic properties of 50 specimens from a continuous section through the lower layers of the Troodos ophiolite in the CY-4 drill hole, reveal an alteration and palaeomagnetic history consistent with ocean spreading. Anisotropy of magnetic susceptibility (AMS), low temperature demagnetization (LTD), high temperature demagnetization (TD), distinct Curie and Néel temperatures and hysteresis were the main rock magnetic techniques and were supplemented by thin section microscopy.

The steeply dipping CY-4 drill hole has a total depth of 2263 m from the surface through the sheeted dike complex, upper and lower gabbro rocks and ultramafic rocks. CY-4 was part of the Cyprus Crustal Study Project in the 1980s as a Cyprus Geological Survey of Canada-NATO collaboration.

The AMS results showed primarily oblate magnetic fabrics reflecting plutonic ductile flow and strain dominated by chlorite, magnetite, biotite and amphiboles. The bulk susceptibility (κ) discriminates the four lithological zones very well, with the highest κ in the diabase dikes. The AMS tensor means showed the overall magnetic fabric to be a strong L>S fabric with L ~ vertical and the diabase dikes being the main contributor. The magnetic fabric became less pronounced with depth through the gabbros down to the mantle rocks, indicating weaker strain or flow influences on the fabric in the upper mantle.

Palaeomagnetism was studied by thermal demagnetization, low temperature demagnetization and detailed measurements of natural remanent magnetism (NRM) on 45 specimens. Characteristic and secondary magnetizations were isolated and palaeolatitudes were compared on the apparent polar wander path (APWP) of the Troodos microplate. Two main vector components were identified from NRM results, a stable and primary component A, with an unblocking temperature (T_{ub}) >550°C and a secondary viscous remanent magnetism (VRM) component D, with a T_{ub} <140°C. NRM palaeopoles for the diabase dikes were anomalous and did not contribute to the conclusions. Palaeopoles for the upper gabbros plot on the APWP as the oldest rocks suggesting that they cooled first, followed by the lower gabbros at about 75 Ma and the ultramafic rocks acquired their characteristic remanence at 55 Ma. Hydrothermal alteration on the NRM of Troodos varied with time and spreading distance from the ridge. The upper gabbros cooled and acquired their magnetizations before the anticlockwise rotation of the Troodos microplate. However, the lower gabbros were affected during the first rotation of about 60° whereas the ultramafic rocks were magnetized in the final approximately 30° rotation.

Curie and Néel temperatures identified specific iron and iron-titanium oxide magnetic minerals. These temperatures also indicate the degree of hydrothermal seafloor alteration vertically down the CY-4 drill hole. Magnetic hysteresis determined the grain size of magnetic minerals and their capacity for palaeomagnetization. Curie Balance results showed magnetite was most common followed by hematite, throughout CY-4. Ti-rich magnetite (TM_{60}) was present as unoxidized and oxidized grains within the diabase dikes and upper gabbro rocks to a depth of 1060 m. Hysteresis results show an obvious trend of decreasing grain size with depth. However, the majority of samples fell within the psuedosingle domain (PSD) range. The ferromagnetic minerals at the bottom of the drill hole had strong, stable remanence value whereas the top of the hole had minerals with weaker memories (H_{cr}/H_c). These results help to explain the large influence of the diabase dikes on the AMS fabric. Strong magnetization in the diabase dikes is due to TM_{60}, which is identified to the base of the diabase dikes and into the top of the upper gabbroic rocks. The Curie temperatures also identified the hydrothermal alteration boundary at about 1060 meters; this alteration boundary is found 3500 meters below the sea floor in modern ocean-floor stratigraphy.

A hydrothermal circulation cell model was used to explain the variations in magnetic properties of the four lithological groups found in CY-4. As the crust spreads further away from the spreading ridge the convection cell is repeatedly established in the same relative proximity to the spreading axis. Therefore, variations in remanent magnetization are largely due to the alteration over time and range in temperatures with depth and distance from the ridge, as the ocean crust moves through the ridge-parallel zone of appropriate temperature and fracture permeability.

Acknowledgments

This study was financially assisted by the Natural Sciences and Engineering Research Council of Canada (NSERC) by a research grant awarded to Dr. G. Borradaile. The Cyprus Geological Survey Department, Dr.G. Petrides and Dr. I. Panayides offered their assistance and allowed access to the core.

I wish to thank and acknowledge Dr. Borradaile for all of his valuable comments and criticisms, enthusiasm, guidance and expertise throughout this thesis. Also, thank you to Anne Hammond for all her hard work on my cores, thin sections and magnetic separations, Bjarne A. for all of his help and the geology professors at Lakehead University who were always willing to answer my questions.

I would like to thank my parents and family for their interest and support. Last but not least, special thanks to Riku M.

Table of Contents

List of Tables

List of Figures

Chapter 1. Purpose

Ophiolites provide the easiest and most complete access to the upper layers of ocean crust and are readily researched. The objective of this study was to analyse the rock magnetic properties of a continuous section through the lower layers of the Troodos ophiolite in order to add to the knowledge of the magnetic stratigraphy of the oceanic crust, and to understand its palaeomagnetic and metamorphic history.

This study used the CY-4 drill hole, designed as a research project, to sample the lower part of the Troodos ophiolite in Cyprus, situated in the Eastern Mediterranean Sea. Hole CY-4 is located 1 km south of the village Palekhori on the road to Agros (Fig. 1.1). It was the last of a series of five holes, drilled for the Cyprus Crustal Study Project (CCPS) by Bradley Brothers, with the intent of recovering a complete section of the Troodos ophiolite from the top of the extrusive sequence to the base of the cumulate section. This section through the Troodos sequence was accomplished with relatively shallow holes due to subsequent doming and the fact that the Troodos is one of the least deformed ophiolites.

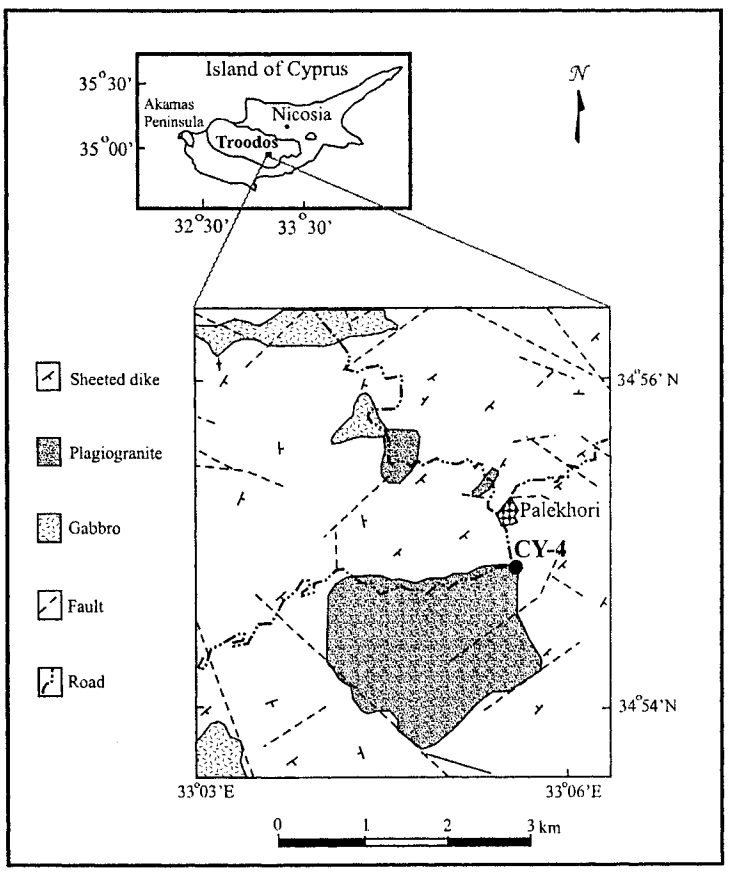

Figure 1.1 Schematic map showing the location of the CY-4 drill hole on the Troodos ophiolite, Cyprus (Modified after Robinson, 1989).

The CCSP was started under the direction of the International Crustal Research Drilling Group (ICRDG). The ICRDG was comprised of scientists and funding sources from Canada, Denmark, the United Kingdom, Iceland, United States and West Germany. P.T. Robinson was appointed the project director for the drilling operations and field mapping that took place on the Troodos ophiolite for CCSP.

The Geological Survey of Canada printed a set of three volumes on behalf of the CCSP to report the findings from the research drill holes. The first of the volumes was on holes CY-1 and CY-1a. These two holes sampled the extrusive section of the Troodos ophiolite.

A second volume was for the CY-2 and CY-2a drill holes, which were drilled in the Agrokipia ore deposits of the Troodos ophiolite to explore the hydrothermal circulation and ore formation in oceanic crust (Fig. 1.2). CY-2 was drilled into the Agrokipia '***A***' deposit and CY-2a was drilled through the Agrokipia '***B***' deposit.

As a part of the CCSP, the ICRDG had the following objectives for CY-4:

a) to determine the intrusive and compositional relationships within the sheeted dike complex;
b) to determine the nature of the transition between the dikes and the gabbros;
c) to investigate the age relationships of the dikes, gabbros and the near by intruded body of plagiogranite;
d) analyse differences in chemistry and mineralogy within the plutonic section to find out if these rocks evolved from a single magmatic sequences or a number of plutons; and
e) to determine the nature and degree of hydrothermal alteration within the dikes and gabbros (P.T Robinson, I.L Gibson and C. Xenophontos, 1989).

The steeply dipping CY-4 drill hole had a total depth of 2263 m from the surface through the sheeted dike complex, upper and lower gabbro rocks and terminated in layered ultramafic rocks. The relationships between rock units, as well as the extent of alteration, were found to be more complex then originally thought by Robinson (1989). It was thought that the CY-4 drill hole would intercept the gabbro at or before 600 m since the area surrounding CY-4 showed good exposure of the gabbro outcrops. However, the drill hole was located in a dike swarm more than 600 m in vertical thickness, previously thought to be the maximum depth of the sheeted dike complex (Robinson, 1989).

The core recovery for CY-4 was 99.9% and each piece of core was fitted together tightly with an 'up' arrow along the side of the core to indicate its relative orientation in the drill hole. This permitted meaningful palaeomagnetic vector directions and magnetic fabric axes to be recovered, not only scalar information on the magnetic mineralogy. Precise re-orientation in geographic coordinates is not possible since the drill core rotated and the orientation of the drill hole was never reported although it was attempted to keep the drill hole near-vertical.

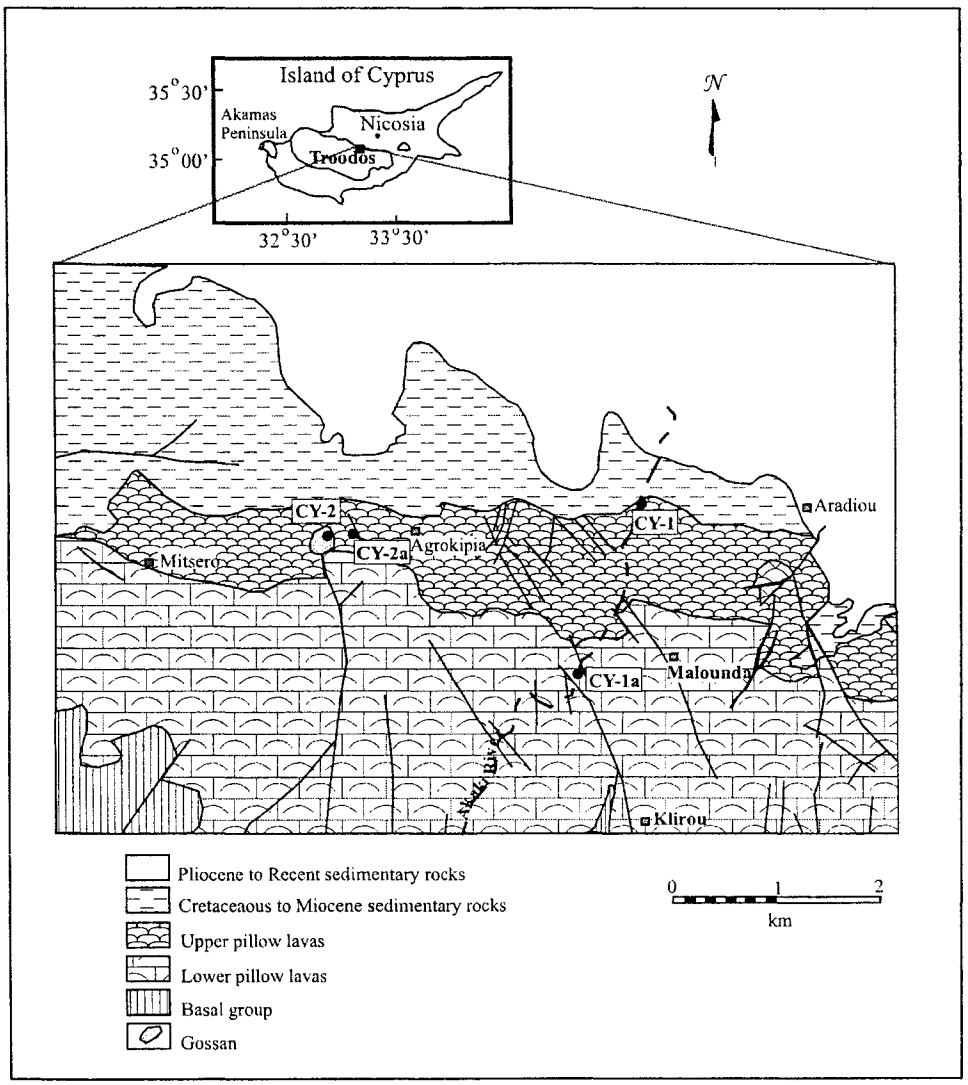

Figure 1.2 Simplified geology of the area surrounding drill holes CY-1, CY-1a, CY2, and CY-2a of CCSP the Troodos ophiolite (Modified after Robinson, 1987).

The Cyprus Geological Survey Department has allowed this study of these lower layers of the Troodos ophiolite by making available 46 samples of the CY-4 drill core. Dr. G. Petrides, director of the Geological Survey Department of Nicosia, and Dr. I Panayides offered their assistance and access to the core. These samples were taken approximately at 50 m intervals. Studying these rocks will help to understand the oceanic geophysical processes and the plate tectonics of Cyprus by using methods of palaeomagnetism and rock magnetism.

One of the methods used was the Anisotropy of Magnetic Susceptibility (AMS). AMS was used to determine the magnetic fabrics within the rocks. AMS is always measured before any palaeomagnetic techniques, since it is non-destructive to all other magnetic information.

AMS was first used to verify that natural remanent vectors record the palaeofield orientations accurately (Borradaile and Jackson, 2004). AMS can indicate structural evolution features, such as the direction of flow magma and implications for the effects of tectonic processes on the Troodos ophiolite.

The palaeomagnetism was studied by thermal demagnetization, low temperature demagnetization and detailed measurements of natural remanent magnetism (NRM) in 15 increments in temperature of 45 specimens. After demagnetization, appropriate characteristic and secondary magnetizations were isolated and then palaeolatitudes were compared with the apparent polar wander path (APWP) to infer any latitudinal motion of the Troodos ophiolite over its cooling and metamorphic history. Of course only the palaeolatitude can be precisely determined from rotated drill core. However, the core was precisely fitted together and it's viscous magnetic overprint allowed the recognition of its N-orientation.

The Curie and Néel temperatures were used to determine the iron and iron-titanium oxide magnetic mineralogy of the rocks. These temperatures were indicative of the degree of hydrothermal seafloor alteration vertically down the CY-4 drill hole. Magnetic hysteresis was also used to determine the grain size of magnetic minerals. Knowing the magnetic mineralogy helps to fully interpret the NRM data.

In this study the palaeomagnetism and AMS record the processes and history of the lower layers of oceanic crust while the defined magnetic mineralogy through critical temperature points and hysteresis measurements support these findings. Each method used and their results are explained in its own chapter. To help understand the magnetic mineralogy, background information on the non-magnetic mineralogy as well as the tectonics of Cyprus and the Eastern Mediterranean are found in the earlier chapters. Chapter 8 summarizes the results and the conclusions.

Chapter 2. Tectonics of Cyprus

2.1 Introduction

This chapter reviews the tectonics of the Eastern Mediterranean Sea, Cyprus and the emplacement of the Troodos ophiolite. The tectonics of the Eastern Mediterranean Sea region is discussed in section 2.2. This is important in explaining the regional geology of the area and the origins of the Troodos ophiolite. Section 2.3 details the tectonic history of Cyprus. Illustrations in this section establish the subduction zones and relative motions of the continents surrounding Cyprus that resulted in the uplift and emplacement of Troodos. Section 2.4 compares the different emplacement mechanisms of the ophiolites in the Eastern Mediterranean Sea. Section 2.5 describes the Troodos ophiolite stratigraphy in comparison to the "typical" oceanic crust.

2.2 Tectonics of the Eastern Mediterranean Sea

The Eastern Mediterranean is a complex area consisting of microcontinents and abundant ophiolites, the latter being defined as fragments of oceanic crust exposed on land (Fig. 2.1). Morris and Tarling (1996) stated that the tectonics and palaeogeography from the Late Tertiary to Quaternary could be explained moderately well. However, overall consensus about the Mesozoic to the Early Tertiary cannot be made, due to its complex history and fragmentary information. Yet, possible scenarios for the relative locations of continents, microcontinents and the openings of ocean basins before the Tertiary, have been made. Van Der Voo (2004) explains that the overwhelming complexity of the mobile zones in the Eastern Mediterranean Sea has allowed a plethora of contradicting palaeogeographic models to be proposed. Robertson (2000) summarized the tectonics and selected models of palaeographic reconstruction from the Mesozoic forwards.

The Easternmost Mediterranean region may have originated as a small Neotethyan ocean basin (Robertson and Woodcock, 1986), which refers to ocean crust located adjacent to the Gondwana content lying to the south (Sengor, 1985; Ustaomer and Robertson, 1994; Stampfli et al., 2001; Robertson, 2004). Development of the Eastern Mediterranean involved Gondwana and Laurasia rifting apart through the Late Permian, Early-Mid and Late Triassic, followed by Gondwana drifting across the Tethys Ocean, becoming amalgamated with Eurasia (Robertson and Dixon, 1984). Ophiolites throughout the Eastern Mediterranean may be remnants of the Mesozoic Neotethys ocean floor. Rarely these ophiolites, such as Troodos, formed above supra-subduction zones (SSZ) (Murton and Gass, 1986; Pearce et al., 1984). Many scientists do not accept this idea on the basis of limited geochemical characterization of a SSZ origin (Robertson,

2004). The Tethys ocean basin closed in the Early Tertiary forming the Mediterranean Sea. Microcontinental collisions occurred during the closure causing the rotation of tectonic units. Figure 2.2 illustrates the tectonic units in the Eastern Mediterranean.

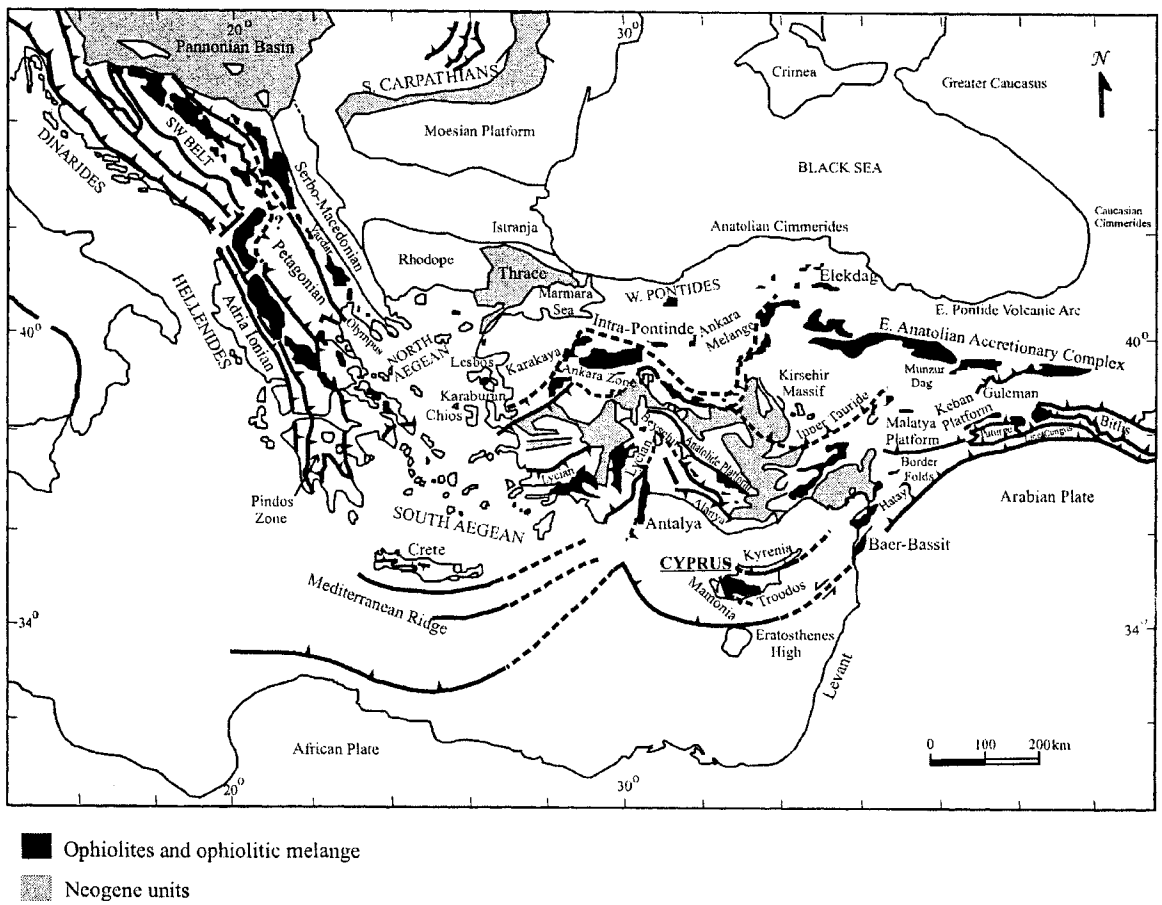

Ophiolites and ophiolitic melange

Neogene units

Figure 2.1. General tectonic map of the main units in the Eastern Mediterranean Sea at present. (Modified after Robertson et al., 1996)

The Alpine-Mediterranean Tethys ophiolites are primarily made up of Mesozoic and Tertiary rocks. Many hypotheses for the evolution of the tectonics of the Alpine-Mediterranean area are currently in debate, as well as two models for the history of the Palaeotethys, which Robertson and Dixon (1984) review. Many ideas for this chapter are taken from Robertson and Dixon's review and are compared with other sources such as Garfunkel (2004), Mart and Robertson (1998), Robertson et al. (1996) and Morris (2003). The first model discussed implies that Palaeotethys was destroyed by subduction southward under Gondwana. The second model consists of the ocean being consumed by a northward subduction under Eurasia. Both models validate the opening of the Tethys or Neotethys, a second ocean south of Palaeotethys and the northward drift of Gondwana. The northward subduction is the preferred model in this paper.

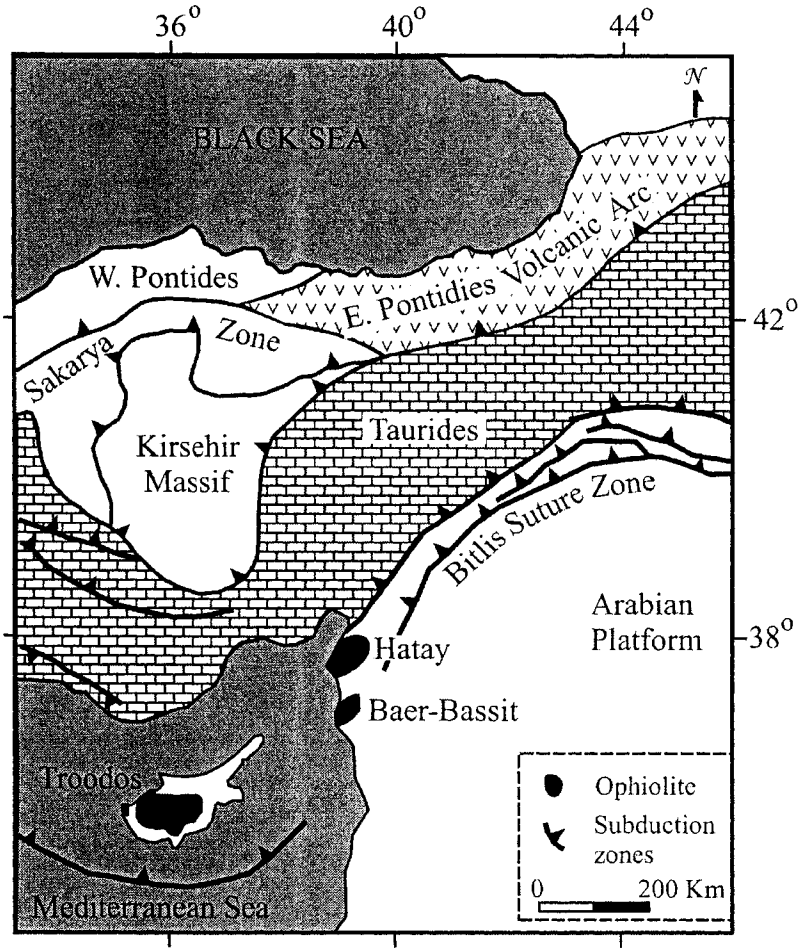

Figure 2.2. Simplified outline of the Eastern Mediterranean region and the main regional tectonic units. This figure shows the discontinuous ophiolitic chain from Troodos in Cyprus to the Hatay-Baer-Bassit terrane in Syria. (Modified after Morris, 2003)

The two models leave little solid evidence, such as ophiolites, to the existence of a Late Palaeozoic oceanic crust. Therefore, a wide Palaeotethyan ocean may not have existed as some authors have question (e.g., Stoklin, 1984 and Robertson and Dixon, 1984).

A general overview of the theories and background information found in the literature was discussed by Robertson and Dixon (1984) and summarised below. Figure 2.3 shows a series of sketches by Robertson and Dixon illustrating the evolution of the Eastern Mediterranean.

Eurasia and North America first underwent a dextral motion relative to Africa, creating the Palaeotethys in the Late Permian to Middle Triassic. The Palaeotethys was an eastward arm of the super ocean Panthalassa. The Eurasia margin of Palaeotethys underwent subduction and strike-slip faulting, while the Gondwana margin underwent active volcanism and extension. Subduction may have also occurred at this margin.

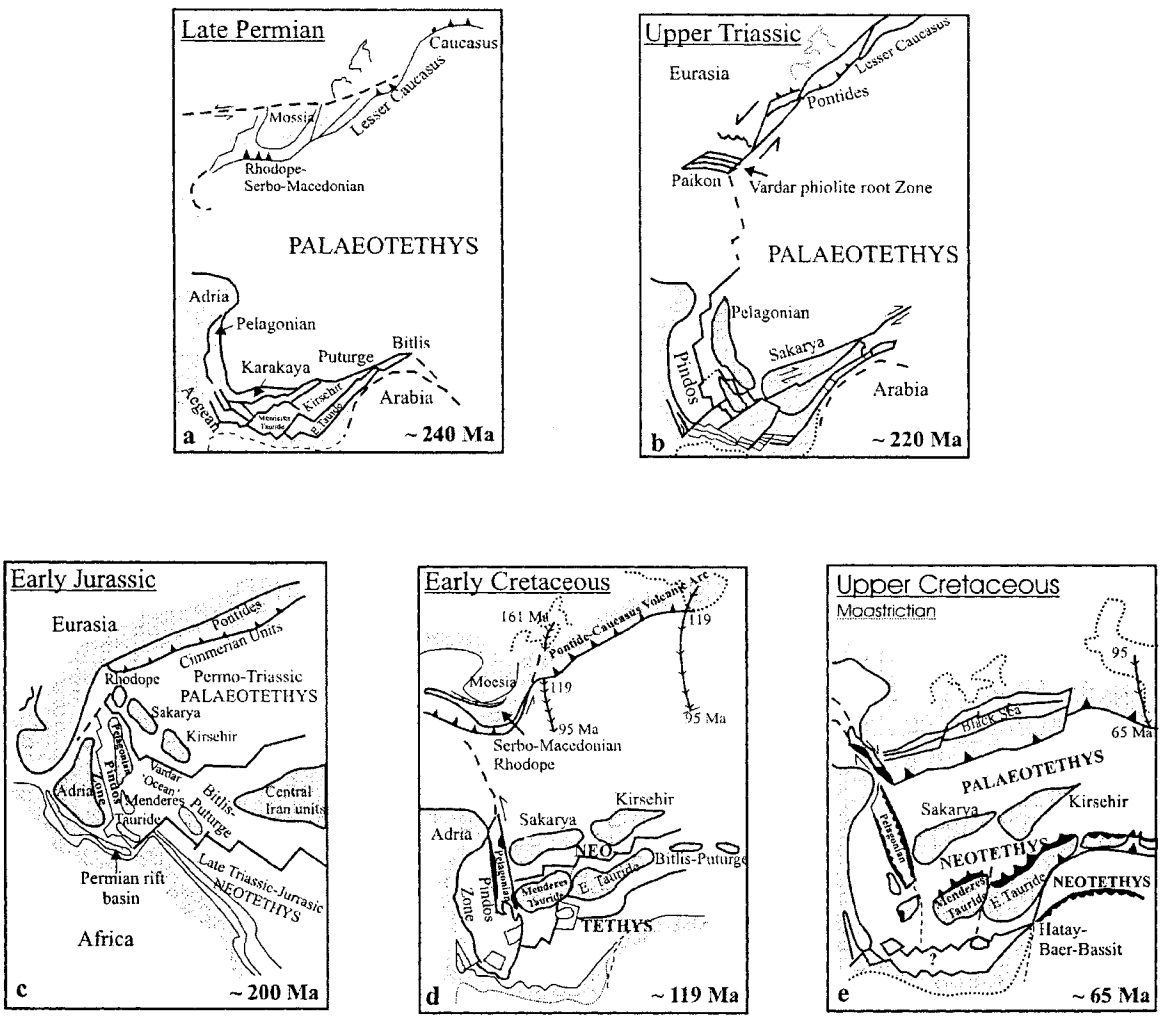

Figure 2.3. Sketches by Robertson and Dixon (1984) to show the reconstructions of the Eastern Mediterranean from the Late Permian to the Upper Cretaceous.

Strike-slip motion, along the future site of the Atlantic opening, occurred during the Middle Triassic to Middle Jurassic. Shearing of Eurasia up to the Middle Triassic resulted in intracontinental rifts propagating westwards from Arabia, to the Levant, and finally to Greece. Major shear displacement within Palaeotethys created a Rhodope-Pontide collage of Late Triassic-Early Jurassic age. The sense of shear between Africa and Eurasia reversed and b[illegible] sinistral by Early Jurassic (Steiner, 1983). A spreading ridge in the Pi[illegible]os zone began and have continued out into the Palaeotethys as an intra-oceanic rift

The Atlantic began to open in the Late Jur[illegible]ssic (173 Ma). This caused the motion of Eurasia, relative to Africa, to change again from southwest to west (Livermore and Smith, 1984), causing north-south spreading centres in the Eastern Mediterranean (Pindos) to form.

Emplacement of intra-oceanic ophiolites and intro-oceanic subduction developed at this time due to collapsed northern and southern boundaries.

The early to Mid-Cretaceous marked a decline in sinistral motion when subduction was initiated along pre-existing structures such as strike-slip faults. A change to north-south convergence occurred and accelerated, coinciding with the opening of the North Atlantic at the end of the Upper Cretaceous period. East-west spreading centres began to open, the Palaeotethys crust along the Pontides margin was consumed and several Neotethyan ocean strands developed. The major change in the motion of Eurasia, relative to Africa, occurred during the Late Cretaceous; spreading centres separated the southern Turkish blocks; subduction zones were initiated and then ophiolites began to uplift.

Africa and Eurasia continued to move towards one another in the Early Tertiary. The south-west Neotethyan rifts became active spreading zones, initiating the movement of the southern Hellenide and South Aegean blocks northwards creating an east-west 'proto-Hellenic Arc'. From the Late Eocene to Miocene a series of collisions occurred until Northern Neotethyan and Palaeotethyans strands were closed, leaving only southern remnant strands south of Turkey, Crete and Peloponnese.

2.3 Tectonics of Cyprus

Deformation along the Cyprean Arc controlled the post Jurassic tectonics of Cyprus, which is now an active plate boundary between the converging African and Anatolian Plates (McKenzie, 1972). Cyprus is divided into three main terranes: Troodos ophiolite, Mamonia tectonic mélange and Kyrenia fold and thrust belt. These are sutured by a post-Troodos pelagic limestone stratigraphy (Fig 2.4). Each are further subdivided within themselves by various units and structures.

The general overall tectonics of Cyprus is summarized below from Robertson (2004). Cyprus was an unstable shelf of Northern Gondwana in the southern part of the Palaeotethys Ocean during the Late Permian (258-248 Ma). Later this became the Kyrenia terrane. Continental rifting of Gondwana around the Mid-Late Triassic (2[illegible]08 Ma) formed a smaller Red-Sea type ocean, the Neotethys, creating microcontinents, which separate the [illegible] and Palaeotethys oceans in addition to helping form the Kyrenia and Mamonia terranes. An unstable subsiding passive continental margin, controlled by strike-slip motion, bordered the Neotethys Ocean in the Late Jurassic to Mid Cretaceous (213-100 Ma). Figure 2.5 shows a possible arrangement of what tectonic elements in the Eastern Mediterranean may have looked like at that time.

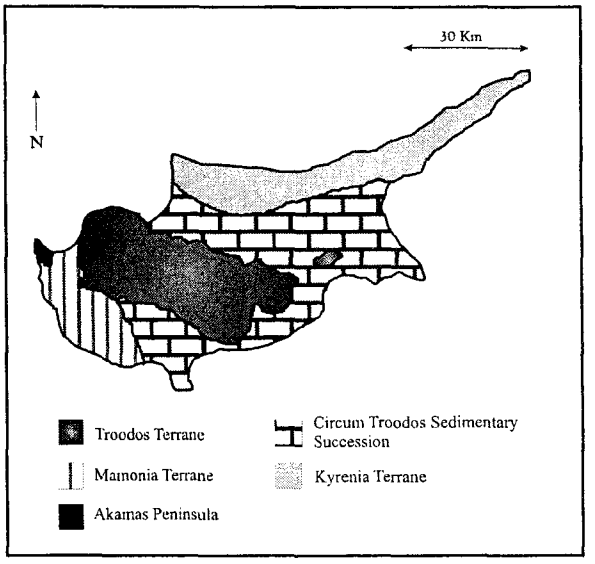

Figure 2.4. Geological terranes of Cyprus, Eastern Mediterranean (Modified after Government of Cyprus, Ministry of Agriculture, Natural Resources and Environment, 1995).

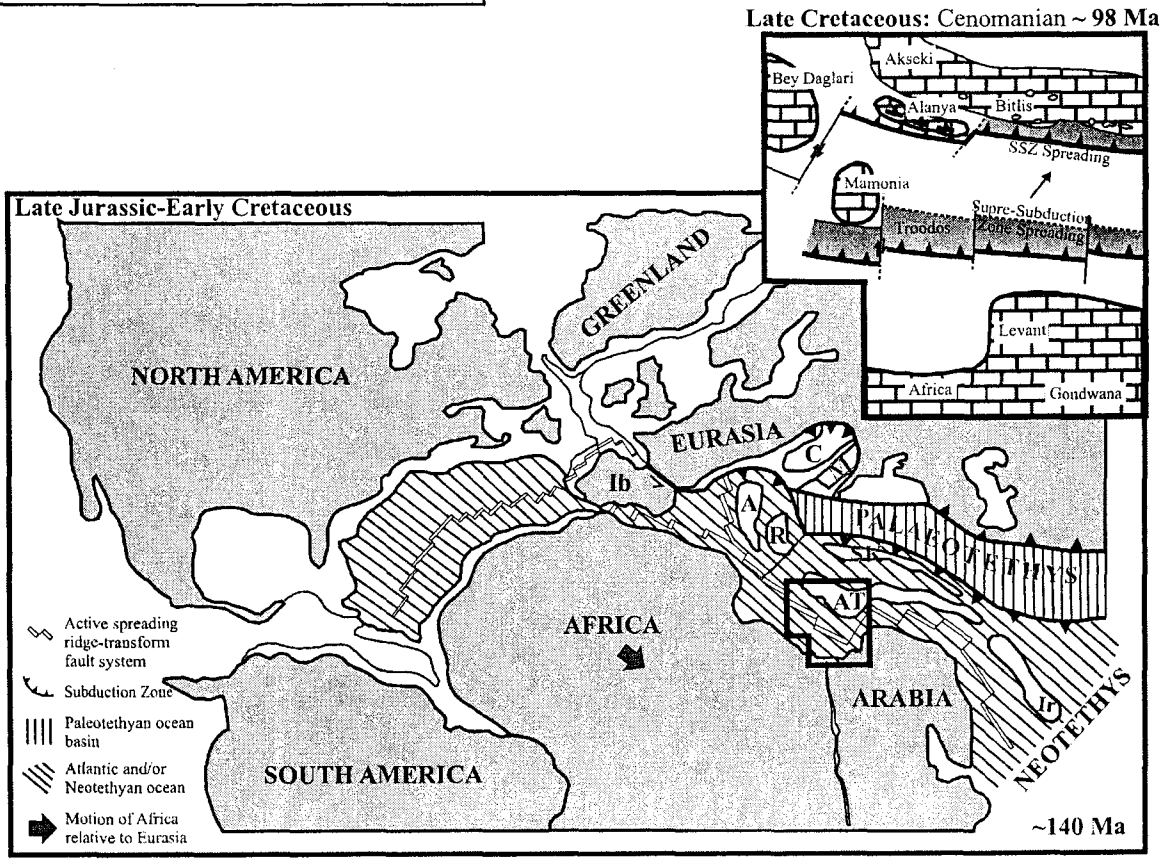

Figure 2.5. This diagram illustrates a palaeogeographic reconstruction of the continents and the interdependently evolving Palaeotethys and Neotethys oceans during the Late Jurassic-Early Cretaceous (Dilek et al., 1990). The position of the continents are simplified and modified from Smith et al. (1981). The grey shaded area is modern coastline. The solid line represents the edge of continent. The important features are labels as follows: A, Apulia; AT, Anatolide-Tauride platform; C, Carnics; Ib, Iberia; Ir, Iran; M, Moesia; R, Rhodope; SK, Sakarya-Kirsehir blocks. The insert in the top right hand corner shows the plate tectonic reconstruction for the Late Cretaceous: Cenomanian-Turonian for the area of interest (Robertson, 2000). The Eastern Mediterranean basin is shown closing with two northward dipping subduction zones and Troodos forming above the southerly of the two zones.

Africa moved east relative to Eurasia. After 119 Ma of moving eastward Africa then moved north, relative to Eurasia. Subduction of the Neotethys was then initiated. The Troodos ophiolite formed above a northward dipping intra-oceanic SSZ in the Late Cretaceous (100-65 Ma) (Fig. 2.5 insert). This zone was rotated a total of 90°. Initially the microplate underwent a >60° anticlockwise rotation that was completed by 65 Ma (Moores and Vine, 1971; Clube and Robertson, 1986). Then, after the first rotation, amalgamation and suturing of the Mamonia and Troodos terranes began (Malpas et al., 1993). The two units were covered and sealed by Palaeocene limestone. An additional 30° anticlockwise rotation of Troodos/Mamonia was completed between 58-37 Ma during the Eocene. Figure 2.6a illustrates the reconstruction the palaeo-rotation of the Troodos microplate during the Late Cretaceous. Subduction of the Neotethys continued with the thrusting of the African plate under the Eurasian plate at a shallow angle during the Oligocene/Miocene periods (36-6 Ma). Troodos was then uplifted to a shallow sea environment and Kyrenia underwent subsidence. The Arakapas Fault belt was activated at that time to relieve stress from the area and was not yet a transform fault. The Polis Graben forms in the Late Miocene. A shallow sea separates Kyrenia and Troodos where carbonate-rich sediments were deposited during the Pliocene (5-1 Ma). The doming of Cyprus, centered on Mt. Olympus, takes place during the Pleistocene. The uplift was a result of underthrusting of the Erathosthenes seamount and serpentiniziation of the Troodos mantle sequence rocks (Fig. 2.6b). Compression and uplift along with extension and subsidence of the Kyrenia terrane also aided in the uplift of Mt. Olympus, 1953 m (Robertson, 2000).

Late Cretaceous: Late Campanian-Maastrichtian ~ 70 Ma

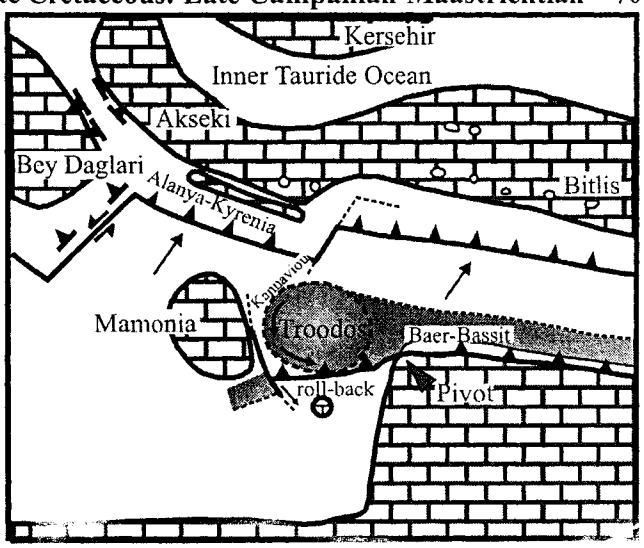

Figure 2.6a. The palaeogeographic reconstruction of the area of interest and one model for the rotation of the Troodos microplate, during the late Cretaceous (Robertson, 2000). The intra-oceanic subduction zone collides with Arabia to emplace ophiolites. During which time Troodos is rotated anticlockwise while [illegible]nic floor.

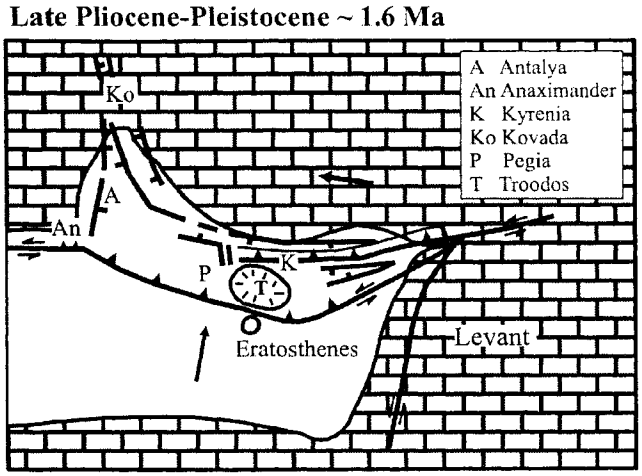

Figure 2.6b. Reconstruction of the Cyprus region during the Late Pliocene-Pleistocene (Robertson, 2000). The collision of Arabia with Eurasia is followed by the Eratosthenes Seamount being subducted under the Troodos microplate aiding, along with related serpentinization, in its uplift.

Early Mesozoic Cyprus evolved within the margins of a small Neotethyan oceanic basin adjacent to the North African continent. The Kyrenia Range formed during early marine deposition and rifting. The Mamonia Complex preserved evidence of Mid-oceanic Ridge (MOR) type basalts and related deep-sea radiolarites and pelagic limestones. Both units underwent passive margin subsidence during the Jurassic-Cretaceous period. Intra-continental subduction took place in the southern Neotethys Ocean taking approximately 90 Ma to form the Troodos ophiolite. The South Transform Fault zone found in the southern part of Troodos recorded dextral motion. The Mamonia terrane was underplated and accreted onto the Troodos Massif west of the Arakapas Transform fault. After Mamonia and Troodos amalgamated thrusting and strike-slip motion caused by anticlockwise palaeorotation of the Cyprus microplate occurred. Northward directed subduction caused the deformation in the Kyrenia Range. Pelagic chalk deposits from the Maastrichtian covered Cyprus onwards while palaeorotation of Troodos continued to occur until the Early Eocene. Northward-dipping subduction persisted until entire north of the inferred subduction zone underwent crustal extension, which came about in the Miocene. Subsidence in the Mesaoria Basin continued and the Pentadhaktylos Graben began to fill with marine mud during the Pliocene. The Eratosthenes Seamount began to collide with Cyprus in the Pleistocene, initiating uplift of Troodos and Kyrenia Range (Robertson, 2002).

2.4 Ophiolites in the Eastern Mediterranean Sea

Ophiolites in general were first described as "typical" oceanic lithosphere formed by seafloor spreading at mid-ocean ridges (MOR) (Robertson, 2004). After geochemical data from ophiolites were studied the definition was expanded to include ocean crust formed in subduction-related settings (Pearce and Cann, 1973). Ophiolites provide minimal support for the ages of the ocean crust since most of the ophiolites in the Eastern Mediterranean are dismembered, eroded or

are extremely altered. Nonetheless, many have been dated. The Tauride ophiolites have been found to be of Cretaceous age (Thiuzat et al., 1981). The Antalya Complex showed various ages that are of Late Cretaceous to the Tertiary boundary. The Troodos Massif and Pozanti-Kersanti were also of Late Cretaceous ranging from 87-75 Ma (Aktas and Robertson, 1984). Mukasa and Ludden (1987) determined the plagiogranite intrusions in Troodos to be 90-92 Ma, using U-Pb dating. The Baer-Bassit ophiolite was established to be 73-99 Ma from the sheeted dikes using K-Ar. However, K-Ar dates from the metamorphic sole of the Baer-Bassit provided a minimum date of 85-95 Ma (Delaloye and Wagner, 1984). Robertson and Dixon (1984) stated that all Late Cretaceous ophiolites were originally created at east-west spreading axes, offset by north-south transform faults. It can be stated that all of the ophiolites in the Eastern Mediterranean were not created in the same tectonic setting, although they do have similar features in common with one another. Figure 2.7 shows the locations of some of the important ophiolites mentioned in the above text.

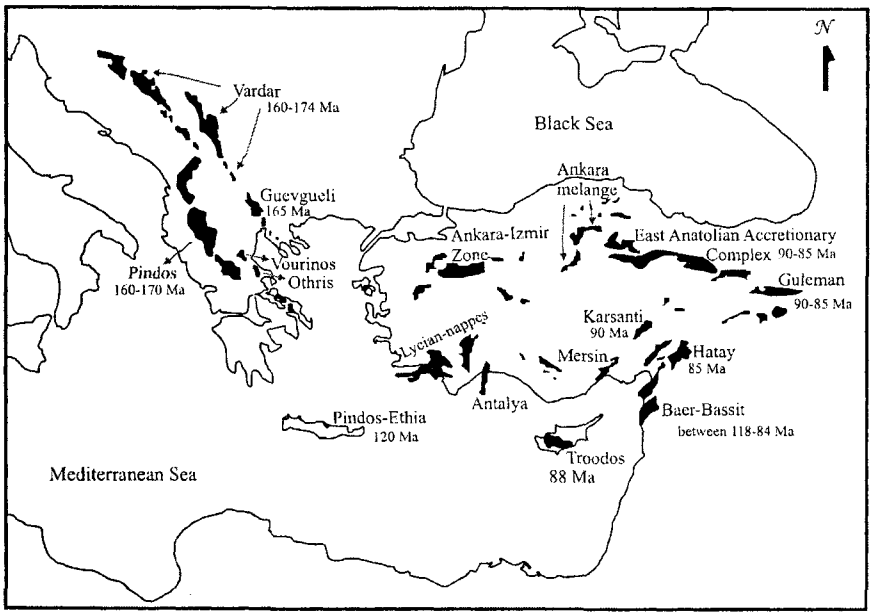

Figure 2.7. The locations of the main ophiolites (shaded areas) of the Eastern Mediterranean as they are seen today are shown here. Some of the approximate ages are also given. (Modified after Robertson and Dixon, 1984)

The ophiolites in the Eastern Mediterranean show large compositional variations (Noiret et al., 1981) and it is not likely that the ophiolites were all created in the same tectonic setting. It is known that enrichment in large-ion-lithophile elements (LIL), such as K, Rb and Ba, and depletion in high-field-strength elements (HFS), such as Nb and Ta, indicate formation above a subduction zone. Pearce et al. (1984) concluded that most ophiolites in the Eastern Mediterranean were derived from boninite lavas, whereas Smith and Spray (1984) classify the ophiolites as different rock types and varying tectonic settings. The Pindos ophiolite is an example of this. Smith and Spray (1984) stated the Pindos to be calc-alkaline and Pearce et al. (1984) stated it is of both Mid-oceanic ridge basalt (MORB) and boninite lava types. Another

example is the Vourinos ophiolite, which Smith and Spray (1984) named the Vourinos, a transitional MORB/ocean island/continental tholeiite, and Pearce et al. (1984) concluded to be boninitic. A consensus between Spray (1984) and Pearce et al. (1984) on the origin of the Othris ophiolite was found between the two to be MORB type lava. Saunders et al., (1980) summarised that the Jurassic ophiolites were formed in a range of tectonic settings or possibly all in back-arc basins, since some back-arcs will show MORB characteristics. Smith and Spray (1984), and Pearce et al. (1984) also agreed the ophiolites of Cretaceous age (i.e. Troodos, Baer-Bassit, Hatay) formed above a subduction zone. However, Whitechurch et al. (1984) argued that the Troodos and Hatay ophiolites were different than Baer-Bassit and Antalya as the latter have abundant harzburgites and cumulates and are much thicker with respect to Troodos and Hatay.

2.5 Tectonics of the Troodos Ophiolite

Whether or not it formed in a back-arc, SSZ or a MOR setting, the Troodos Massif displays classic features of an ophiolite or on-land fragment of oceanic lithosphere. A MOR origin was first favoured for Troodos (Gass, 1968) with the birth of the concept of plate tectonics in 1967. It is known that Troodos is classic oceanic crust and therefore is a remnant of the southerly Neotethyan ocean basin (Robertson et al., 1991, 1996). However, the exact origin has not yet been agreed upon. Miyashiro (1973) favoured a volcanic arc setting because of the overlying extrusive sequence. Robinson et al. (1983) later preferred a subduction-related origin due to the composition of volcanic glasses. Finally, possibilities were narrowed to a subduction-related forarc or backarc setting or SSZ (Miyashiro, 1973; Pearce, 1975; McCulloch and Cameron, 1983; Robertson et al., 1983; Rautenschlein et al., 1985; Thy et al., 1985; Robertson, 2004) with a spreading ridge system within the main Troodos Massif (Moores and Vine, 1971; Varga and Moores, 1985) and a transform fault (Simonian and Gass, 1978; Muron, 1986). Moores (1996, 2000) suggested that there was a mantle depletion that could have occurred as part of his "historical contingency" premise during mantle recycling rather than above a subduction zone. Moores (2000) correctly noted that the recycling of the material in any of the many earlier subduction zones would result in the depletion of the magma. The depletion need not be due to the contemporary plate setting.

The Troodos ophiolite and related ophiolites in the Eastern Mediterranean form two discontinuous linear belts of oceanic fragments along the Bitlis-Zagros suture north of the Afro-African plate (Dilek et al., 1990). Microcontinents of shelf deposits of Cambrian to Cretaceous age separate these two ophiolite chains (Dilek et al., 1990). The ophiolites to the north of the microcontinents are deformed and associated with tectonic mélanges and nappe systems whereas

to the south they are relatively complete (Dilek et al., 1990). Both of these belts are of Jurassic-Cretaceous age and are all, except the Troodos, emplaced from north to south onto the Afro-Arabian margin during the Cretaceous (Dilek et al., 1990). The Cyprus terranes are still being emplaced today onto the subducting northern margin of the African continent.

The main Troodos Massif consists of a dome that exposes the stratigraphic oceanic layers from the centre with the mantle sequence made up of peridotite and serpentinite overlain by mafic to ultramafic plutonic rocks, an extensive sheeted dike complex, extrusive rocks and a sedimentary cover. The southern part of the Troodos ophiolite is slightly different because of the Arakapas (transform) Fault zone. Here the Limassol Forest Complex is made up of tectonized peridotite and serpentinite, mafic plutons and dikes, pillowed and massive lavas, and volcaniclastic rocks (Simonian and Gass, 1978; Murton, 1986).

Uplift creating the dome structure of the ophiolite occurred during the Pliocene. This exposed the cross section of a typical ophiolite, contained on Mt. Olympus. Figure 2.8 compares the sequence from the Troodos ophiolite to the typical modern oceanic floor stratigraphy. The different lithology and stratigraphic layers of the modern ophiolite is comparable to the Troodos ophiolite since they both have the same thickness and distribution.

Multiple magma chambers built the Troodos ophiolite at three or more recognizable spreading axes, not at a single MOR (Malpas, 1989; Moores and Vine, 1971), with a discontinuous and unstable magma supply to the Sheeted Dike Complex. The axes constitute part of a slow spreading ridge system, which had an average spreading rate of approximately 100 mm/a (Hayman, 1996). There are three fossil axes, Solea, Mitsero and Larnaca, and one fossil transform fault, Arakapas Fault, identified within the Troodos Massif (Fig. 2.9). The magma chambers were short-lived, about 200 000 years (Gauthier, 2002). Palaeomagnetic data indicate the original spreading axes trended approximately east-west in direction since the declinations of primary remanence are now directed to the west (Clube and Robertson, 1986). It has been proven that the Troodos ophiolite underwent a progressive, decelerating anticlockwise rotation from 92-88 Ma until the present (Clube et al., 1985; Borradaile and Gauthier, 2002), while moving northward with the early rotation axis located in the microplate (Borradaile and Lucas, 2003). The rocks forming the island underwent a net rotation about the spreading axes of approximately 90° anticlockwise to their present north-south alignment (Varga and Moores, 1985). The upper part of the ophiolite rocks, the dikes and pillow lava sequence, showed sea-floor metamorphism of greenschist to amphibolite facies and, more rarely, to brownschist facies.

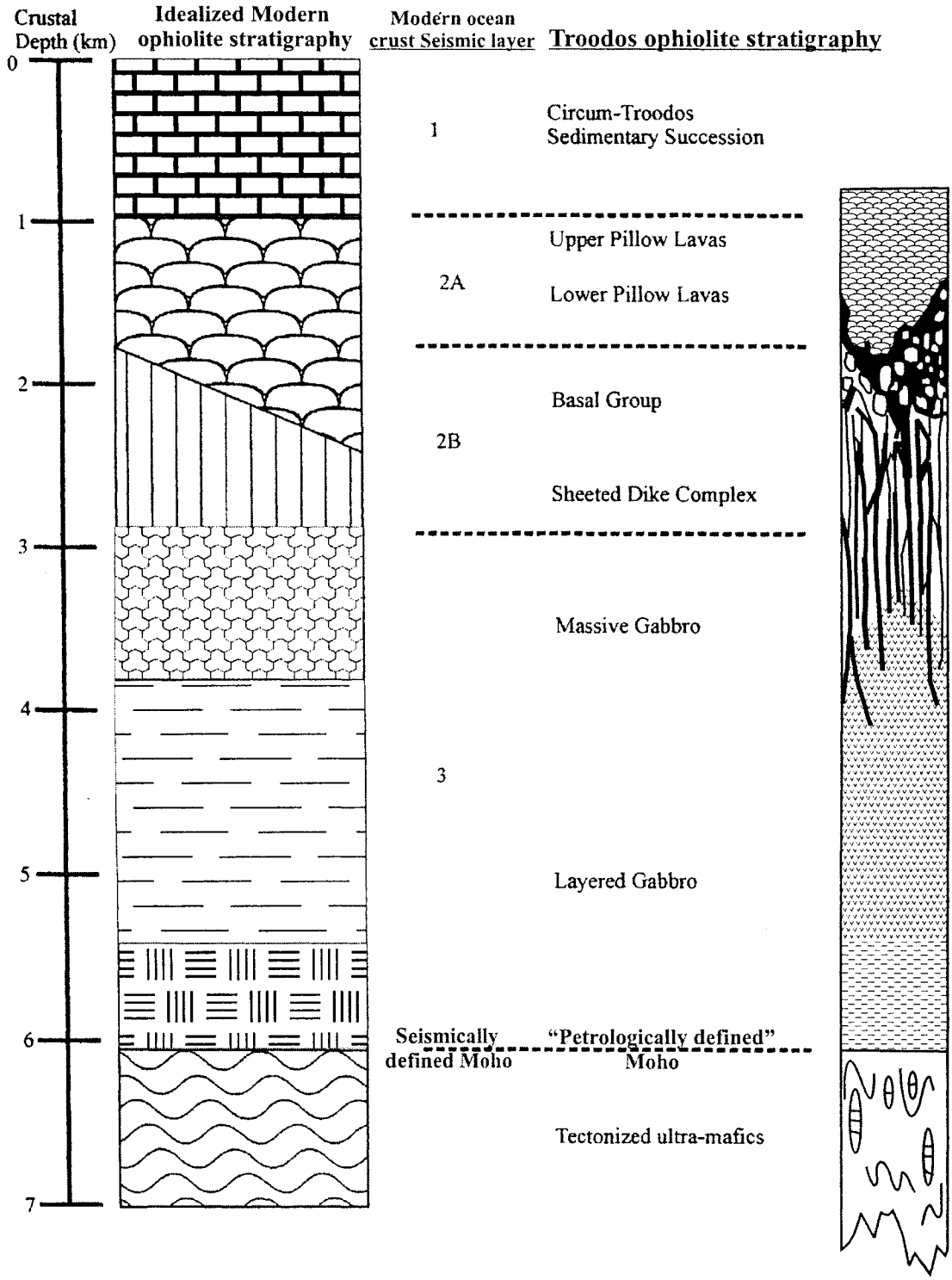

Figure 2.8. Idealized ophiolite sequence in the right column is compared to the Troodos ophiolite stratigraphy on the left. The Troodos ophiolite stratigraphy correlates well to the modern ophiolite stratigraphy and the oceanic layers defined seismically. (Modified after the Geological Survey of Cyprus, 1995)

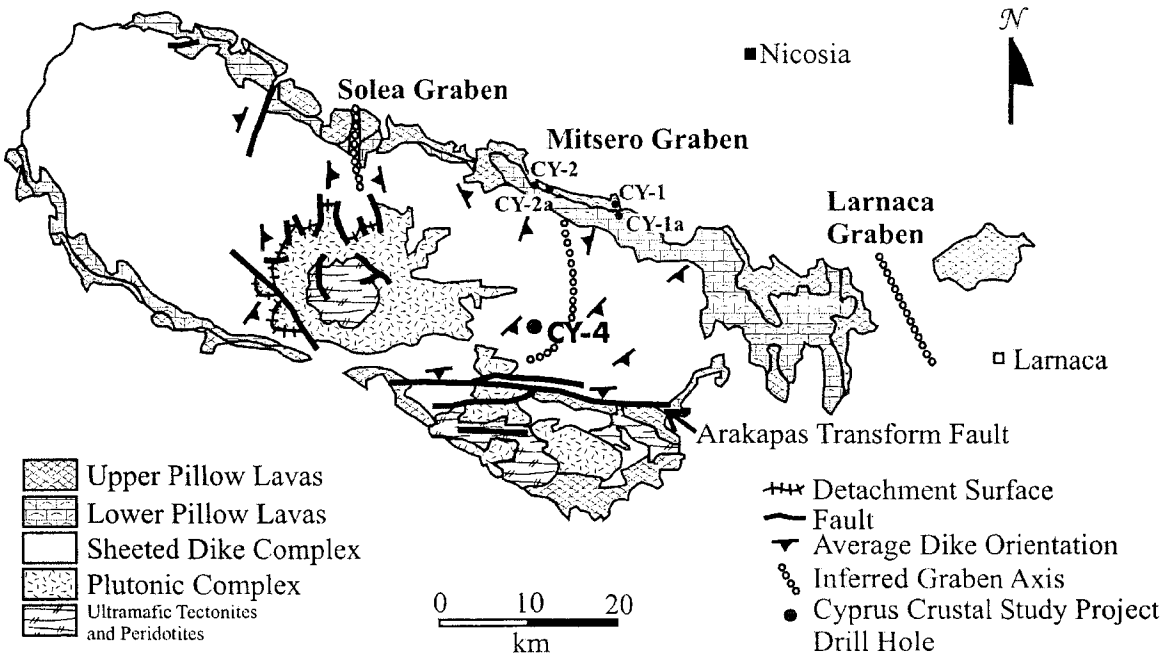

Figure 2.9. Illustration of the general geology of the Troodos ophiolite, with the fossilized transform fault, Arakapas, and the three fossilized spreading ridges, Solea, Mitsero and Larnaca, now seen structurally as grabens. The location of the 5 Cyprus Crustal Study Project drill holes is also shown on this map. (Modified after Dilek et al., 1990)

It was recently accepted that the Akamas ophiolite was a distal off-axis extension of the Troodos ophiolite isolated from Troodos by the Polis rift valley (post-Eocene) (Borradaile and Lucas, 2003). The Akamas ophiolite has an exposed mantle sequence of plutonic rocks and dikes. The rocks of Akamas are more weathered and sheared than other ophiolitic rocks in Cyprus. It was found by Borradaile and Lucas (2003) that the Akamas and Troodos mantle-sequence harzburgites had the same pattern of oriented mantle-flow fabrics and the same Tertiary magnetizations were acquired during exhumation.

Chapter 3. Study Area Geology

3.1 Cyprus Crustal Study Project

The CCSP was initiated in 1980 by P.T. Robinson, who proposed to the ICRDG that the Troodos ophiolite in Cyprus would aid in their investigation to better understand the structure, lithology and composition of the oceanic crust by developing a three dimensional model of the ophiolite. Field studies were approved and started by the Cyprus Government in 1980-1982. Drilling commenced in April 1982 by Bradley Brothers, Noranda, Quebec and was continued until March 1985. Five holes (Fig. 3.1), at three sites, were drilled with an averaged core recovery of approximately 95%. A total of 4563 meters were drilled between the five drill holes.

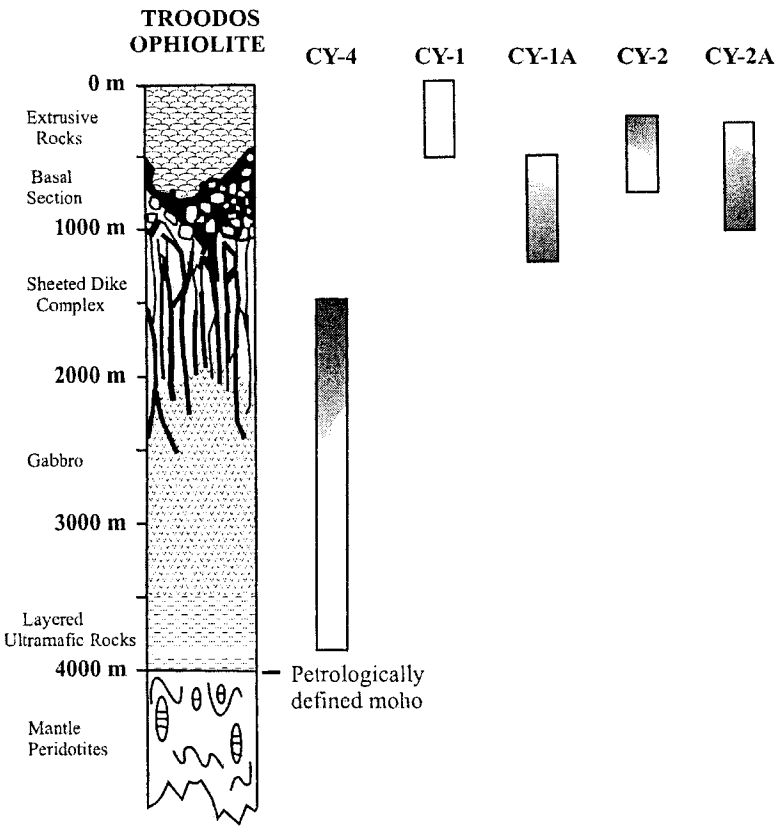

Figure 3.1. The relative positions of the 5 CCSP drill holes on an idealized stratigraphic section of the Troodos ophiolite. The shaded areas indicate the extensively altered sections within each drill hole. (Modified after Vine and Smith, 1990; Malpas and Robinson, 1991)

The first of these five holes, drilled in 1982, was CY-1. This first drill hole is located in the Akaki River canyon (Fig. 1.2). Hole CY-1 was drilled into the lava sequence and was anticipated to go through the entire extrusive section and part of the sheeted dike complex. It reached a depth

of 485 m, ending in the lavas with the remaining extrusive sectioned sampled in the 700 m hole CY-1a, about 0.5 km to the south (Fig. 1.2) (Robinson, 1991).

It was found by examining the extrusive sections in the CY-1 and CY-1a that the lavas had a higher vesicularity than MORB lavas, indicating extrusion at shallow depths (Schmincke et al., 1983). However, water depths have been estimated at 2000 m from the nature of the overlying sediments, so that is an unlikely origin (Schmincke and Bednarz, 1990). Geochemical data showed differentiation of Troodos lavas relative to MOR basalts, suggesting magma fractionation occurred in small chambers with infrequent introduction of new magma (Malpas and Robinson, 1991).

Two distinct lava suites were identified on the northern flank of Troodos on the basis of glass composition. The two suites included an arc-tholeiite suite made up of basalt to rhyodacite and another suite comprised of picrite to andesitic basalt. These two lava suites were believed to represent separate parental melts (Tarney and Marsh, 1991; Mehegan, 1988). Both suites were formed by hydrous partial melting of depleted upper mantle material (Malpas and Robinson, 1991). Magmas represented by the two suites evolved separately but both erupted during spreading. The suites were intermingled at different stratigraphic levels and could not be subdivided geochemically into the upper and lower pillow lavas as defined by Bear (1960).

Smewing (1975) and Gass and Smewing (1973) redefined the upper pillow lava/lower pillow lava boundary as a metamorphic facies change. The upper pillow lavas were affected by zeolite facies metamorphism, whereas the lower pillow lavas underwent extensive greenschist facies alteration. Gass and Smewing (1973) originally believed the lower pillow lavas represented on-axis lavas and the upper pillow lavas signified post-spreading, off-axis lavas. The permeability controlled the alteration within the lavas and four alteration zones were then outlined. From the top to the bottom they include: the Seafloor Weathering Zone, the Low Temperature Zone, the Transition Zone, and the Upper Dyke Zone (Gills, 1987; Gills and Robinson, 1988).

The magnetic properties within CY-1 and CY-1a were investigated by Hall et al. (1991). The intensity of the natural remanence steadily increased from the top of the extrusive rocks down to approximately 500 m. Below 560 m the samples were very weakly magnetized. The distribution of initial susceptibility with depth showed an increase from the top to a depth of 600 m. There was a trend of increasing susceptibility values with depth from the surface to 600 m. Then from 600 m to 1 000 m samples were scattered without any trend with depth. Stratigraphic changes in Curie temperatures (T_C), showed four zones. The first was from the surface to 260 m where values decreased from the surface at 550°C to 450°C. From 260 m to 410 m there were

two T_C at 300°C to 350°C and 500°C to 550°C. The third zone from 410 m to 630 m showed scattered T_C values in the range of 365°C to 575°C. In the fourth zone from 630 m to the bottom of the section the T_C was steady around 580°C.

The second set of drill holes for the CCSP, drilled in 1982, were drilled into the Agrokipia ore deposits of the Troodos ophiolite, which investigated the nature of the hydrothermal circulation and ore formation in oceanic crust. The massive sulphide ore deposits in the Troodos ophiolite occur as clusters in the extrusive section. They are commonly lenticular in cross section and are mainly of a conglomeratic texture consisting of irregularly shaped blocks in a matrix of sandy sulphides (Constantinou, 1980). Beneath the massive ores sits a stockwork of mineralized and hydrothermally altered breccias, pillowed and massive lava flows and dikes (Robinson and Malpas, 1987). The two holes drilled a total of 915 m. Hole CY-2 reached a depth of 226 m in the Agrokipia '***A***' deposit and hole CY-2a was drilled 689 m through the Agrokipia '***B***' deposit (Robinson, 1987). Agrokipia '***A***' consisted of two massive lenses of distinct ore bodies near the top of the lavas, which were mined in the 1950's (Robinson, 1987). Agrokipia '***B***' is 270 m east of Agrokipia '***A***' and is also located in the lavas but 150 m lower in the stratigraphically (Robinson, 1987). This second deposit was mined during the 1950's and 1960's.

The Agrokipia '***A***' deposit is an exhalative deposit that was formed at the sea floor whereas Agrokipia '***B***' formed by replacement of massive, glassy, lavas (Robinson and Malpas, 1987). Both deposits are hosted within highly differentiated lavas of lower andesite-dacite-rhyodacite series (Robinson and Malpas, 1987). It is understood that seawater was the main ore-bearing fluid (Spooner and Bray, 1977) in the Troodos deposits and they were genetically comparable with black smoker deposits of the East Pacific Rise (Oudin and Constantinou, 1984). Three types of alteration were recognized in holes CY-2 and CY-2a. These were: a low-grade seawater rock interaction zone, a pervasive hydrothermal argillic or propylitic alteration and mineralization zone and a subgreenschist facies hydrothermal alteration zone (Robinson and Malpas, 1987). The hydrothermal activity in the area of the Agrokipia deposits produced a remarkable reduction in the magnetization (NRM) of the extrusive rocks, either by oxidative alteration of the original titanomagnetite grains or by replacement by non-magnetic sulphide minerals, mainly pyrite (Johnson and Pariso, 1987).

The last of the series of CCSP drill holes was CY-4. This was the deepest drill hole, which went through the sheeted dike complex and plutonic complex of the Troodos ophiolite. The area surrounding the CY-4 research drill hole comprised of NNW-SSE trending, steep dipping diabase dikes with a plagiogranite intrusion in proximity (Malpas et al., 1989). The

CCSP recognized five zones based on lithology and phase chemistry (Malpas et al., 1989). These were: 0 to 675 m of sheeted dikes, 675 to 900 m of fine to medium-grained gabbro, 900 to 1330 m of fine to medium-grained gabbronorite, 1330 to 1740 m of medium to coarse-grained gabbronorite and 1740 to 2263 m of medium to coarse-grained websterite. Malpas et al. (1989) stated that the gabbro and ultramafic rocks from the bottom two zones (1330-2263 m) reflect crystallization in relatively closed magma chambers, whereas the rocks in the upper zones (0-1330 m) reflect crystallization in a magma chamber that was open to periodic replenishment. They found that the boundary at 900 m coincides with the sheeted dyke/gabbro transition.

The CCSP found a general trend of more primitive mineral compositions as depth increased. This meant the clinopyroxene and orthopyroxene showed a decrease in Fe/Mg ratios, olivine showed a decrease in fayalite mole per cent and the plagioclase showed a decreasing albite mole per cent trend (Malpas et al., 1989).

The palaeomagnetic results from the CCSP indicated that the top 600 m of the CY-4 drill hole had an overall high NRM and magnetic susceptibility, which decreased with depth down into the gabbro and ultramafic rocks (Malpas et al., 1989). Hall et al. (1989) found that the NRM distribution with depth was fairly constant with a few areas of higher values. One area of higher values was between 500 to 600 m. The second area was between 700 to 1500 m and the third area with two zones found from 1830 to 1970 m and 2200 to 2263 m. The research group did not have an explanation for the higher values of NRM within the sheeted dikes, except for the fact that they are aphyric instead of phyric. However, the higher values of magnetization found in the ultramafic rocks were largely due to the serpentinization.

The initial susceptibility defined four zones: 0 to 600 m, 600 to 1300 m, 1300 to 1750 m and 1750 to 2263 m. These four zones were closely related to the main lithologies (Hall et al., 1989). It was concluded that the relatively high susceptibility samples from 0 to 1300 m were related to the dikes and the values from 600 to 1750 m, were associated with the plagiogranite intrusions and the isotropic gabbroic rocks (Hall et al., 1989). The low values below 1750 m were found to correspond to gabbroic rocks whereas the high values were due to the highly serpentinized zones (Hall et al., 1989).

The Curie temperatures found by Hall et al. (1989) had a restricted distribution, which were independent of the lithology units. Most Curie points were in the 500 to 600°C range with the exception of three points found between 300 to 350°C near the dike/gabbro transition and two points found around 700°C in the ultramafic rocks.

3.2 Present Study

Dr. Graham Borradaile and Thomas Hamilton collected 46 samples of CY-4 drill core, during their 2003 field season in Cyprus. Anne Hammond drilled 146 one inch, in length, core pieces that were 10.3 cm^3 in volume. The core pieces were used for rock magnetic experiments. A. Hammond also cut 30 thin sections for petrology work and crushed 23 magnetic powder samples for use in the Curie Balance instrument.

This study concentrated on the magnetic properties of 2250 m, out of the total 2263 m of the CCSP CY-4 research drill hole. Thin section petrography was used to define the different levels of alteration and overall amounts of oxides found throughout CY-4, in order to better understand the evolution of these rocks and therefore facilitated the interpretation of the palaeomagnetic and rock magnetic results. Section 3.2.1 details the general non-magnetic petrology of the CY-4 drill hole. Section 3.2.2 describes the alteration as a result of hydrothermal fluids and serpentinization.

3.2.1 Petrography

The petrology was divided into four broad groups based on lithology similar to those used for the rock magnetic methods. Thirty thin sections were examined in this study. Seven thin sections were from the diabase dikes, seven were from the upper gabbronorite, five were from the lower gabbronorite and three were from the ultramafic websterite or olivine websterite. Raymond (1995) summarized the major textures of ophiolites to be cumulate, hypidiomorphic-granular and tectonite. Minerals most common according to Raymond are plagioclase, clinopyroxene, orthopyroxene, olivine, hornblende, actinolite and chromite. These primary minerals were seen within the 30 sections as well as the metamorphic minerals quartz, sericite, chlorite, biotite and serpentine. Raymond (1995) generalized the mineralogy as follows:

- Above the mantle sequence rhythmic and cryptic layering was found in the plutonic unit. Major rock types were gabbro, diorite, lherzolite, wehrlite, pyroxenites, and troctolite. The olivine ranged from Fo_{91-75}, plagioclase was of the composition of An_{97-40}, and pyroxene was Mg-rich.
- The dike and sill complex consisted of fine-grained gabbro, diabase, dolerite, and basalt.

The overall composition of the diabase dike section examined in this study was approximately 55-60% plagioclase, 30-35% mafic minerals (amphiboles, pyroxenes and olivine) and 2-7% oxides. The diabase was fine to medium-grained intergranular plagioclase, pyroxenes and amphibole along with, sericite, chlorite and quartz. The plagioclase had become cloudy due

to saussuritization. The clinopyroxenes were altered to actinolite, chlorite and sometimes biotite. Minor epidote was also found in a few of the sheeted dike thin sections. When considering the minerals and amount of alteration seen within the slides the grade of metamorphism that affected the diabase was mainly lower greenschist facies. However, Elthon and Stern (1978) and Elthon (1981) concluded the metamorphism of the dikes to be of actinolite facies. Figures 3.2a-f illustrate the various textures and mineralogy of the diabase dikes from the CY-4 drill core.

The alterations of the sheeted dikes were most intense at the top of the drill hole and decreased downwards. The prominent alterations seen were of the plagioclase to sericite and pyroxenes to chlorite and hornblende. The amount of oxide minerals decreased with depth. There were a few small veins or fractures seen. These were filled in with quartz and chlorite and sometimes epidote.

The upper gabbronorite unit appears to be mainly fresh with some alteration of the plagioclase and pyroxene. By volume, the average composition of the gabbro and gabbronorite between 600-1180 m was 50% plagioclase, 25-20% clinopyroxene, 15-20% orthopyroxene, 2-3% amphibole, chiefly hornblende and 2-5% oxide minerals. The thin sections examined were mainly medium grained gabbronorite. Gabbro was observed where there were samples with lesser amounts of orthopyroxene. The textures seen were hypidiomorphic, where all crystals were generally subhedral and ophitic. Relict crystals of plagioclase were cloudy and altered to sericite to approximately 900 m. Some alteration of the mafic minerals to chlorite was also observed in this section. Below 900 m the plagioclase, as well as all other minerals, appeared to be fresh with very few quartz and chlorite filled veins. The oxide minerals were seen as interstitial and the concentration did not appear to change with depth. Figure 3.3a-f shows the gabbronorite textures and mineralogy observed in thin section.

The dike/gabbro transition zone in this study occurred from approximately 600 m to 700 m. Stillman (1989) placed this boundary at approximately 500 m with narrow zones that reached depths of 1200 m. He concluded that the plutonic rocks formed a cluster of discrete plutons, each of which were associated with their own dike swarm.

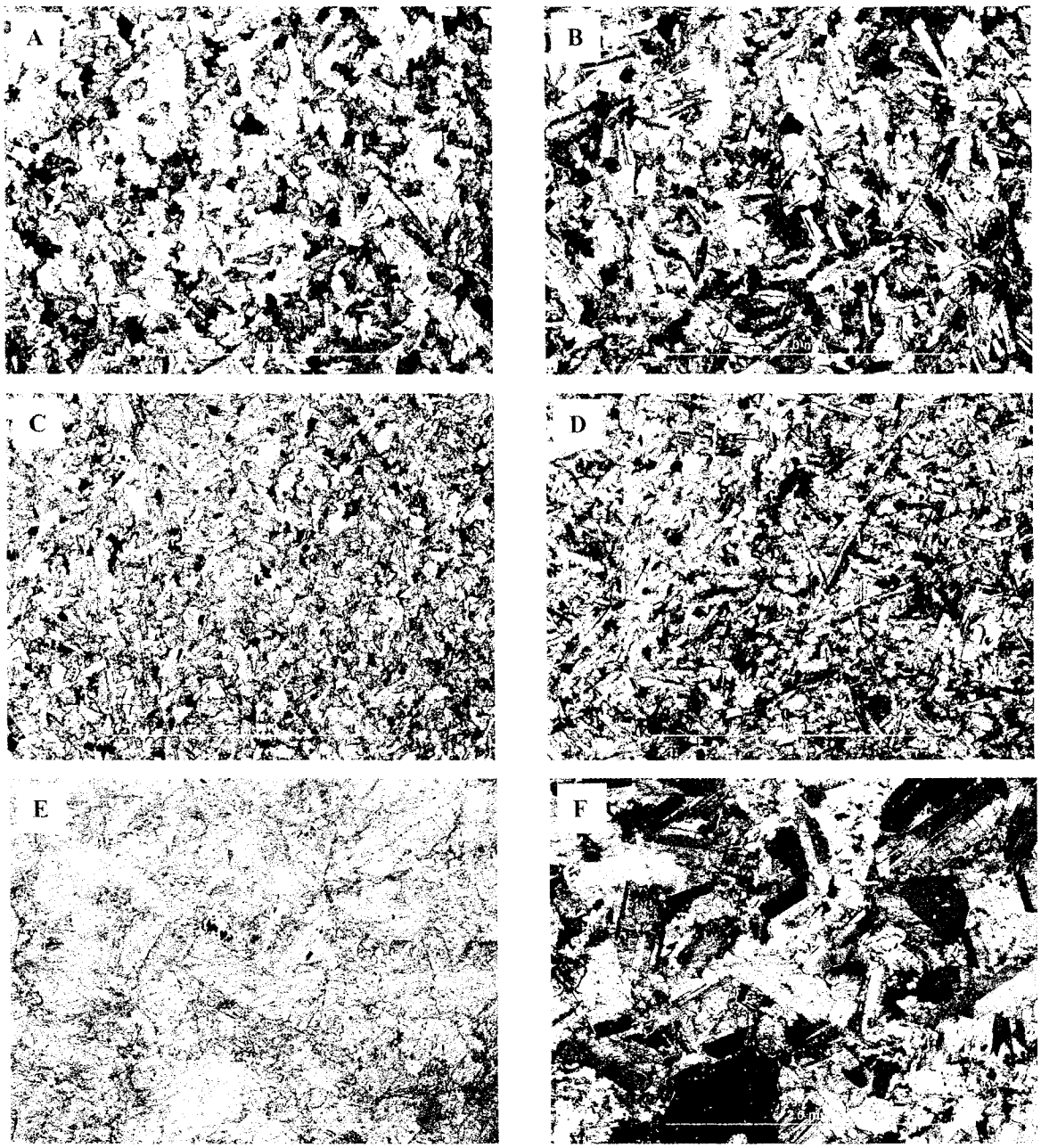

Figure 3.2. **A)** Diabase in plane polarized light at a depth of 187 m showing the intergranular texture of plagioclase laths with interstitial pyroxenes, olivine and amphiboles. **B)** Diabase at 187 m in cross-polarized light. **C)** Fine-grained diabase in plane polarized light at a depth of 349 m illustrating the intergranular texture seen in most of the diabase. The oxides make up approximately 5-7% by volume. **D)** Cross polarized photomicrograph of the diabase at 349 m. **E)** Medium-grained ophitic texture diabase from 628 m in plane polarized light with relict plagioclase altered to sericite. Note the fewer oxides seen lower in the sheeted dike complex. **F)** Diabase at 629 m in crossed polarized light. Many of the mafic minerals have been altered to chlorite here.

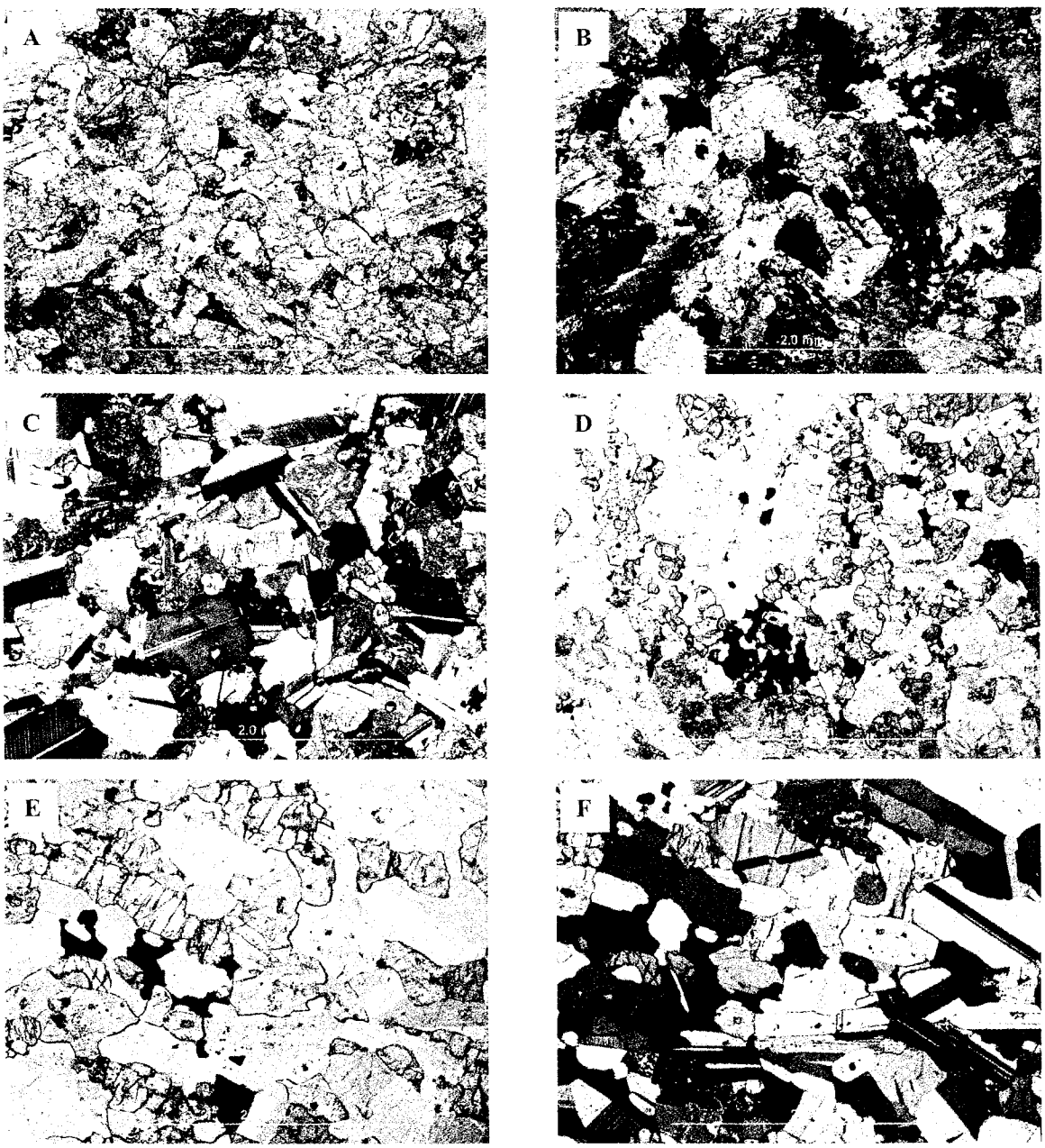

Figure 3.3. **A)** Plane polarized photomicrograph of gabbronorite at a depth of 812 m showing the greenish pleochroism of the pyroxenes. **B)** Cross polarized view of the gabbronorite at 812 m. **C)** Cross polarized gabbronorite at 994 m exhibiting the intergranular texture of the plagioclase, orthopyroxene, clinopyroxene, olivine and oxides. **D)** Gabbronorite at 1060 m in plan polarized light illustrating the euhedral plagioclase crystals and anhedra, irregular grains of pyroxenes and oxides. **E)** Medium-grained gabbronorite at 1179 m showing orthopyroxene, clinopyroxene and oxides occupying the space in between plagioclase in plane polarized light. **F)** Unaltered gabbronorite from 1179 m in crossed polars.

From 1180 m to 1810 m lower gabbronorite rocks were observed (Fig. 3.4a-f). The average mode of this lithology group was 30-40% plagioclase, 15-20% orthopyroxene, 15-20% clinopyroxene, 3% amphibole, 2% olivine and 2-5% oxide minerals. The fine to medium grained gabbronorite and gabbro displayed porphyritic textures. Areas of the coarser grained gabbronorite showed a granoblastic texture as well as higher pyroxene and lower plagioclase concentrations.

The thin sections examined showed mainly fresh rocks with little to no alteration. One exception was at 1520 m where evidence of serpentinization (Fig. 3.4d) was seen around the mafic minerals. Generally, the plagioclase crystals were euhedral to subhedral and exhibited Carlsbad twinning indicating the relative freshness at depth. The mafic grains were seen to be subhedral to anhedral. Mafic minerals in some areas were affected by chloritization in small amounts.

The ultramafic rock lithology group (Fig. 3.5) was interlayered and cumulate websterite and olivine websterite. The overall composition of the websterite was 65 % clinopyroxene, 30 % orthopyroxene and 5% olivine. The olivine websterite had a similar composition but was 15% olivine and had lower amounts of pyroxene. The pyroxene was euhedrual to subhedral and the olivine was anhedral.

The alteration seen in this group of thin sections was moderate at the top and increased with depth. At the bottom of the CY-4 drill hole almost all the olivine and some pyroxene (mainly the orthopyroxene) was replaced by serpentine. The alteration into serpentine was along irregular cracks of the olivine crystals giving rise to the separation and production of fine-grained Fe-oxide minerals. This created an irregular network of fibrous serpentine with oxide minerals. This net texture is shown in Figure 3.13a. As serpentinization increased the average mode varied from 5-15% olivine to about 5-15% serpentine.

3.2.2 Metamorphism and Alteration

Ocean floor metamorphism occurs mainly in the form of hydrothermal alteration. Hydrothermal alteration involves any process that entails the movement of hot, predominantly aqueous fluids, near the active spreading axis. This may be the residual fluid formed in the last stages of crystallization in an igneous intrusion or can be external water, such as seawater over the MOR. The hydrothermal fluids react with the rocks they come into contact with and alter their composition or deposit minerals from solution. For example, iron, copper, lead or zinc sulphides. Hydrothermal reactions that affected the CY-4 rocks were mainly serpentinization, chloritization, and saussuritization.

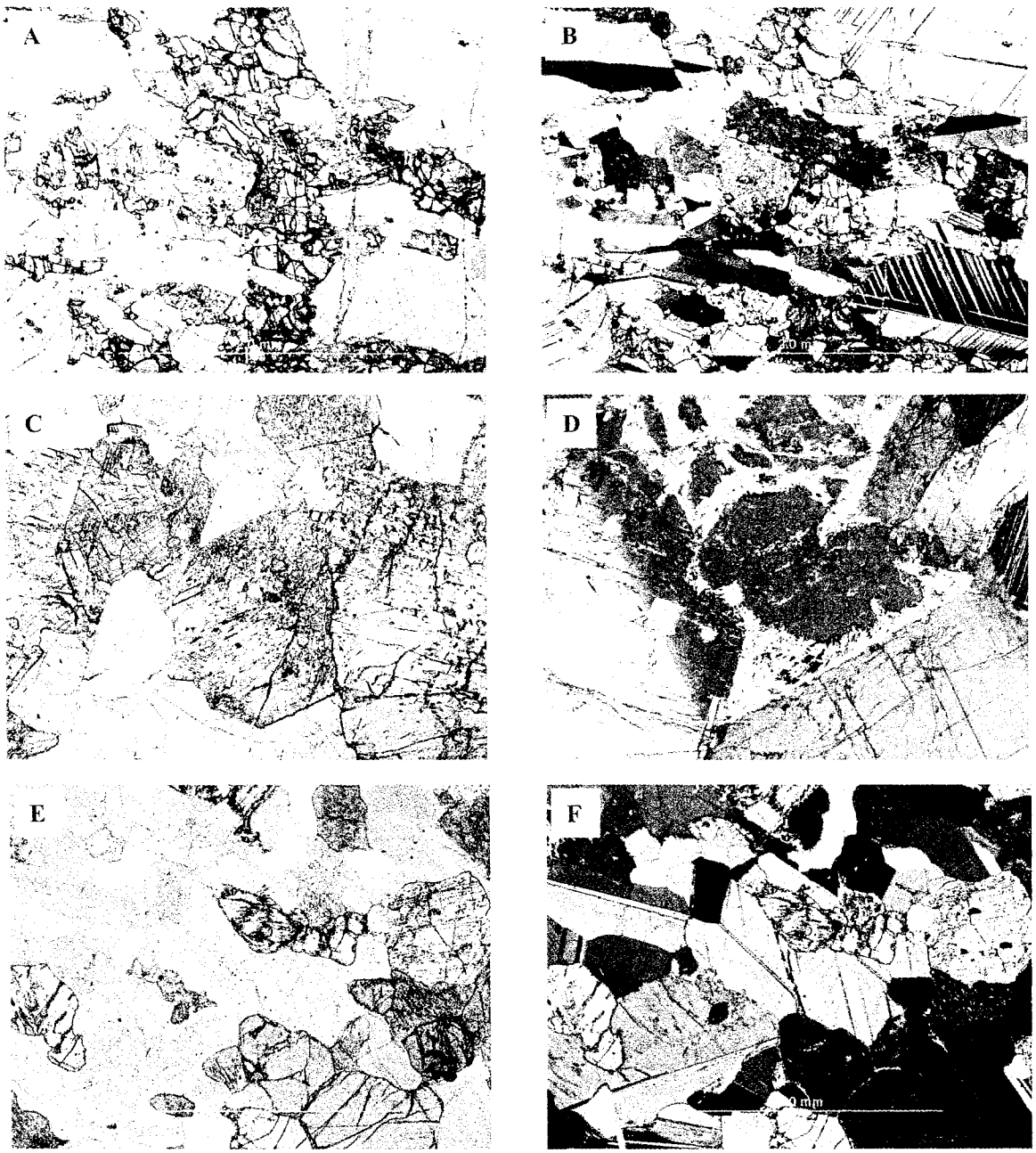

Figure 3.4. **A)** Photomicrograph of a medium-grained gabbronorite from 1294 m in plane polarized light. **B)** Crossed polarized view of the gabbronorite at 1294 m with Carlsbad twinning seen in the plagioclase. **C)** Coarse-grained gabbronorite exhibiting granoblastic texture at a depth of 1345 m, in plane polarized light. **D)** The first appearance of extensive serpentinization seen in crossed polars from 1520 m. **E)** Cumulate gabbronorite composed of plagioclase, orthopyroxene, clinopyroxene and amphibole in plane polarized light at the depth of 1730 m. **F)** Relatively fresh gabbronorite from 1730 m in cross polars.

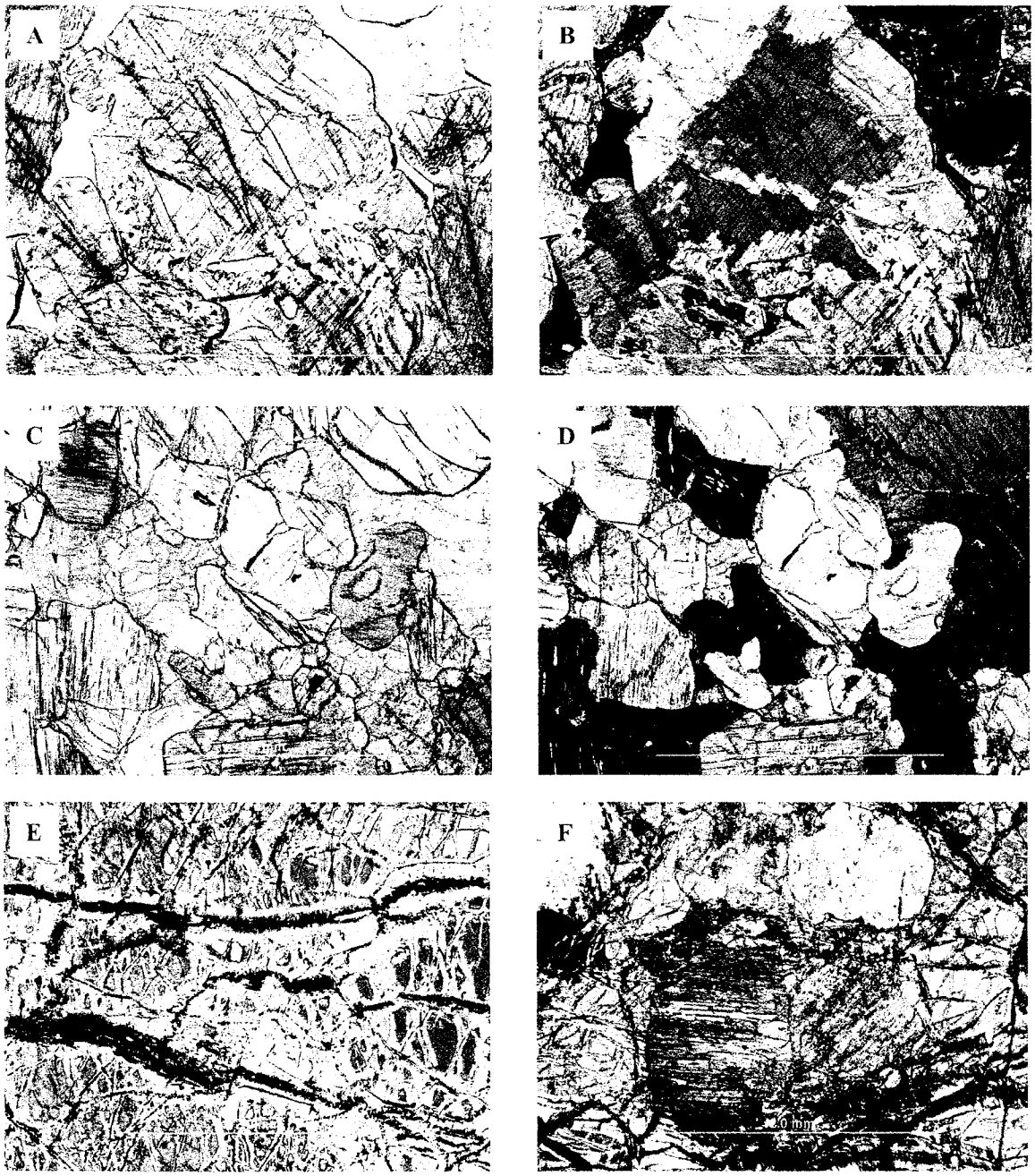

Figure 3.5. **A)** A large olivine crystal partly altered to chlorite at the top and serpentine around the periphery. This photomicrograph is in plane polarized light and is from 1915 m. **B)** In crossed polars the serpentine is more visible in this olivine websterite at 1915 m. **C)** Websterite exhibiting cumulative orthopyroxene, clinopyroxene and minor olivine at a depth of 2131 m in plane polarized light. **D)** Cross polarized view of the websterite at 2131 m. **E)** At 2250 m a net texture of the olivine due to serpentinization can be seen. This photomicrograph is in crossed polarized light. **F)** In crossed polarized at 2250 m the serpentinization seen is extensive.

The mineralogical changes or alterations are different with changing temperatures and pressures of the hydrothermal fluids. This explains the different degrees of hydrothermal alteration on the ocean floor as you move away from the ridge and down into the oceanic crust. Kusznir (1980) has shown that the intrusive rocks have a greater magnetization than the plutonic or mantle rocks. The magnetization of the intrusive rocks may be related to the spreading rate, which in turn influences the depth to which hydrothermal seafloor alteration extends. Since slow spreading ridges move less than 100 mm/a they are mainly comprised of intrusive rocks. This leads to strong magnetization deeper into the oceanic crust for slower spreading ridges (Kusznir, 1980). Haymon (1996) explains that the alteration in ophiolites is consistent with depth of penetration of the hydrothermal fluids adjacent to and just above the axial magma chamber.

Gills and Roberts (1999) discussed theoretical and mathematical models of a magma-hydrothermal transition. Gills and Roberts (1999) placed the transition zone at or near the sheeted dyke-plutonic boundary for the Troodos ophiolite. This transition was where hydrothermal and magmatic fluids mixed as a result of short-lived fractures. The confining pressure also controlled the maximum depth of alteration. The hydrothermal system, which affected Troodos, was considered a steady state system where alteration occurred between fractures. Gills and Roberts (1999) concluded that these fractures were formed within the axial zone of spreading or possibly during the last stages of magmatic activity. It was stated that the fractures were what promoted the mixing of magmatic, metamorphic and hydrothermal fluids. Also, later stages of magmatic activity involved degassing and the increase in fluid pressure induced the hydrofracturing, which once more, promoted the mixing fluids.

The duration of a hydrothermal circulation cell in a segment of spreading ocean crust is approximately several million years (Raymond and LaBrecque, 1987). The crust spreads further and the convection cell is repeatedly restablished in the same relative proximity to the spreading axis. Therefore, alteration effects on remanent magnetization can vary considerably with time and the range in alteration temperatures. Raymond and LaBrecque (1987) inferred this decay of remanence to be the result of the alteration of titanomaghemite to Fe-rich titanomagnetite and titanoilmenite.

At the base of the sheeted dikes there were epidosite zones that represented hydrothermal reaction zones, which reached temperatures up to 350°C (Cann et al., 1987; Schiffman et al., 1987). The reaction zones were thought to move upward through cylindrical alteration pipes and into stockwork zones under the orebodies (Robinson and Malpas, 1987). Detailed studies of these stockwork zones were done in CY-2 and CY-2a. Hydrothermal alteration in Troodos was

subgreenschist to greenschist facies, sea-floor metamorphism. A summary of minerals, which are present in the CY-4 rocks, and their ferromagnetic alteration products are shown in Table 3.1.

Original Mineral	Alteration Ferromagnetic Product	Approximate Temp. (C)
Ti-rich TM60	Magnetite	>300
Magnetite	Maghemite	150-250
Magnetite	Hematite	>500
Olivine	Magnetite	>300
Pyrite	Magnetite	350-500
Maghemite	Haematite	350-450
Pyroxenes	Magnetite	>600

Table 3.1. Summary of some important minerals and their alteration ferromagnetic products and approximate temperatures the alteration occurs. The alterations depend on such factors as grain size, rate of heating, shapes and presence of impurities. (After Tarling, 1983)

In ophiolites and seafloor peridotities, serpentinization is a common alteration process. Serpentinization occurs upon the reaction of high-temperature minerals with lower temperature seawater. The water converts the high-temperature minerals to low-temperature, serpentine-group minerals. The heat released during serpentinization is sometimes the driving force of hydrothermal alteration (Lowell and Rona, 2002). Lowell and Rona (2002) stated the conditions that were needed for serpentinization to occur included a high ratio of tectonic extension to magmatism, low magma budget, and high fracture/fault permeability that supplied the seawater to large volumes of upper mantle rocks. In the context of this thesis serpentinization reactions are important since copious amounts of secondary magnetite would be produced. The hydrothermal temperatures that may result from serpentinization have a wide range of temperatures starting as low as ~300° Celsius, if there is significant heat input from below and a low fluid flow rate (Lowell and Rona, 2002).

Chapter 4. Anisotropy of Magnetic Susceptibility (AMS)

4.1 Introduction

All minerals have an induced magnetic response in the presence of an applied field termed susceptibility. Magnetic anisotropy occurs when the susceptibility due to induced magnetization varies in direction through a rock. The susceptibility is the strength of magnetization (or ease with which a rock can be magnetized) best measured in an applied low strength field to avoid permanent (remanent) magnetization of the ferromagnetic minerals. A typical low field is ≤ 0.1 mT, similar to the Earth's field. The induced magnetization that occurs in this weak field disappears when the field is removed and no permanent magnetization resulted. The natural magnetization of a rock is left unaffected and there are no changes to it. The anisotropy of magnetic susceptibility (AMS) determined how susceptibility varies with direction and thus reflects any mineral alignment, or preferred orientation (Hrouda, 1982; Borradaile and Jackson, 2004) a rock had to the applied field of magnetization. Any material that was not randomly orientated is anisotropic and posses a magnetic fabric corresponding to its structural petrofabric. AMS can reveal this fabric, which may indicate a rock's structural evolution such as the axis of flow of a magma chamber or the effects of tectonic strain.

4.2 Magnetism

Magnetism in a material is acquired when an applied external magnetic field aligns the spin-moments of the electrons in the *d*-orbital. O'Reilly (1974) stated that the materials could be categorized magnetically according to the concentration of the magnetic atoms or the nature of the resultant exchange interactions. Material that contains atoms without uncompensated spins such as water (H_2O) and quartz (SiO_2) are diamagnetic; their induced field was anti-parallel to the applied field. Materials with a low concentration of magnetic species that exchange interactions would couple small isolated clusters of atoms and show paramagnetic responses, parallel to the applied field. These materials may overwhelm the diamagnetic response and are such minerals as chlorite, biotite, pyroxene, amphibole and epidote. More magnetically concentrated materials that exchange interactions produced a magnetic spin order that was retained in the absence of the magnetic field, called ferromagnetic. Examples of ferromagnetic minerals are magnetite, hematite and pyrrhotite. Figure 4.1 illustrates these different types of magnetism.

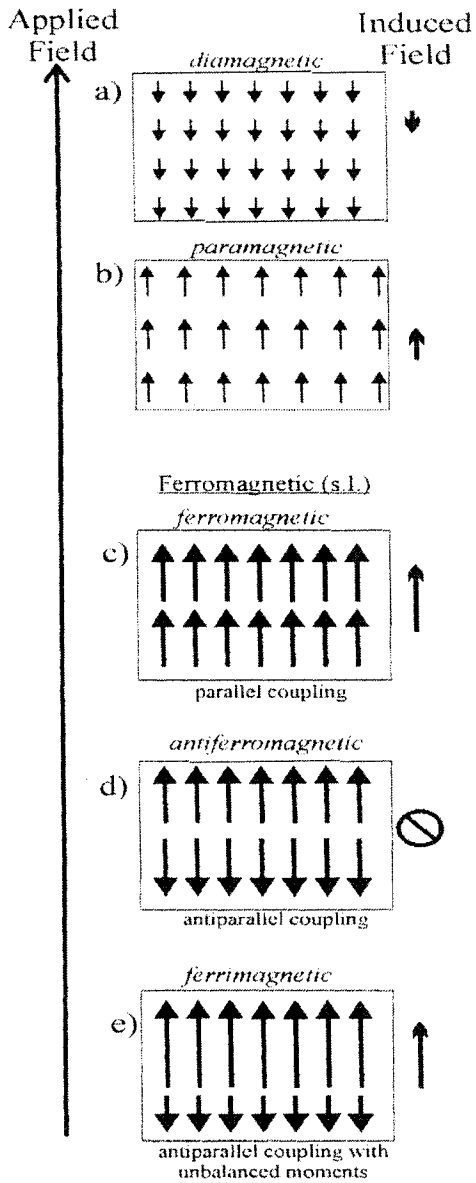

Figure 4.1. Illustration of the spin moments and the resulting net magnetism in the different types of magnetism (Modified after Dunlop and Özdemir, 1997; Weiss, 1907).

Low field susceptibility and its anisotropy concern that of an induced magnetization (M). When dealing with anisotropy the desired field to work with was that of the initial stage on a potential hysteresis loop (M-H at H~0). The initial susceptibility is defined by $\chi = dM/dH_o = 1/N$ and the saturation field is NM_s (Dunlop and Özdemir, 1997). N is the demagnetizing factor. The demagnetizing factor can be used to detect changes in domain state at high temperatures. The relationship $\kappa=1/N$ only holds when shape anisotropy dominates over magnetocrystalline and/or stress anisotropies. In diamagnetic and paramagnetic materials χ is linear. As long as the magnetic field (H) is low, the bulk susceptibility (κ) it can be expressed as:

$$\kappa = M/H$$

Non-linearity occurs in stronger fields, thus the reason AMS was measured in low fields. There was always a danger of some "ferro"magnetic contamination by inclusions of Fe-oxides. This would cause the paramagnetic minerals to acquire a magnetism that was non-linear and therefore non-reversible. When a ferromagnetic material is magnetized in one direction it will not relax back to zero magnetization along a linear path, such as diamagnetic and paramagnetic materials do, when the field is removed. An applied field in the opposite direction will drive the magnetization back to zero and trace out a hysteresis loop (Fig.4.2) on a M-H graph.

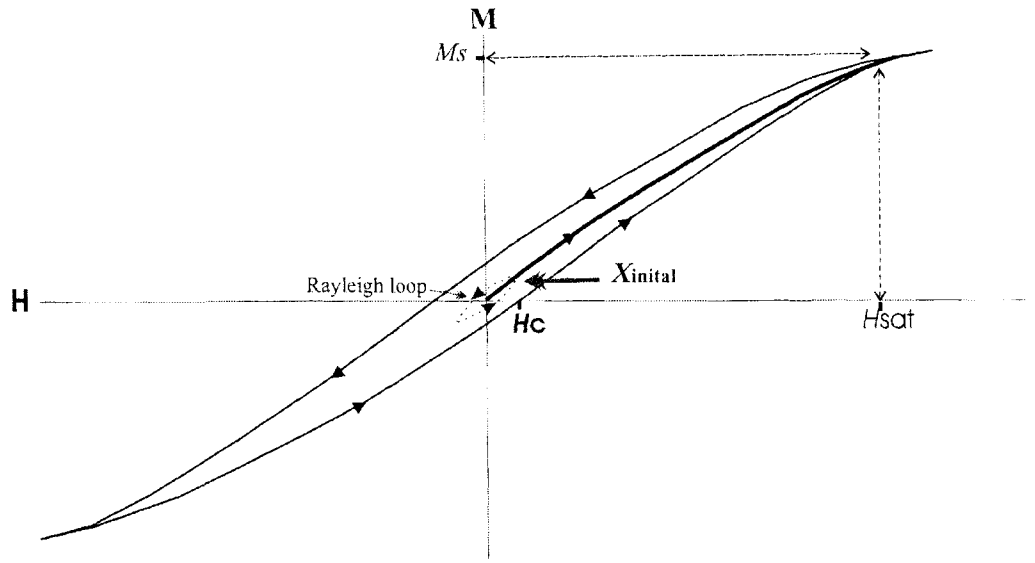

Figure 4.2. Hysteresis loop of a large MD grain of magnetite where H is the field, M is the magnetization, H_c is the coercive force and X is the initial susceptibility. Notice that slope X is linear (X=M/H) near the origin and therefore at a weak field no remanent magnetism is obtained and when an applied field is removed no permanent effects remain on the material.

4.2.1 Diamagnetism

All materials have diamagnetic properties. A magnetic field that is applied to any material whose electron shells are complete will cause electron spins to produce a magnetization in the opposite direction to that of the applied field (O'Reilly, 1974). When this is the only response, the material is described as diamagnetic. Common minerals, if *pure*, such as quartz (SiO_2), calcite ($CaCO_3$) and feldspar ($KAlSi_3O_8$, $NaAlSi_3O_8$-$CaAl_2Si_2O_8$) are diamagnetic (Dunlop and Özdemir, 1997). The magnetic susceptibility for a diamagnetic mineral is negative (-14×10^{-6} SI) and is not temperature dependent. Refer to Figure 4.1a to see how the spin moments and resulting net magnetism appears in a diamagnetic material.

4.2.2 Paramagnetism

Paramagnetism can be described by a partial alignment of atomic magnetic moments in materials that have incomplete electron shells in the same direction as the applied field (O'Reilly, 1974). Common rock-forming minerals, such as amphibole and biotite, are paramagnetic. When the field is removed the electron spin moments return to random orientations. The susceptibility in a paramagnetic material is positive and large compared to a diamagnetic material and for pure silicates it is generally $< 2000 \times 10^{-6}$ SI. However, if there are abundant magnetite inclusions in a paramagnetic mineral, such as amphibole, the susceptibility can be as high as 9000×10^{-6} SI (Borradaile and Henry, 1997). Syono's (1964) formula estimates κ for a pure paramagnetic mineral phase. Syono's formula is:

$$x = \frac{\mu_0 (x_{Fe^{2+}} \rho^2_{Fe^{2+}} + x_{Fe^{3+}} \rho^2_{Fe^{3+}} + x_{Mn^{2+}} \rho^2_{Mn^{2+}})}{(3k_B T)}$$

Where $\rho_{Fe^{2+}} \approx 5.4\rho_B$ is the moment per Fe^{2+} ion and $x_{Fe^{2+}}$ is the number of Fe^{2+} ions per kilogram of sample. This is the same for other ions, such as $\rho_{Fe^{3+}}$ and $\rho_{Mn^{2+}}$ ($\rho_{Fe^{3+}} \approx \rho_{Mn^{2+}} \approx 5.9\rho_B$). The atomic moment ρ will have electron spin and electron orbit components that will be quantized in multiples of ρ_B (ρ_B is Bohr's magneton = 9.274 x 10^{-24} Am^2).

The effects of paramagnetic minerals such as pyrite, biotite and amphibole on the whole rock AMS will outweigh the diamagnetic effects. Diamagnetic and paramagnetic silicates have a lattice with a theoretical susceptibility of ≤ 2000 x 10^{-6} SI with which is higher in most natural examples due to inclusions/exsolutions of oxides (Lagroix and Borradaile, 2000; Werner and Borradaile, 1996; Borradaile, 1994). Figure 4.1b illustrates the spin moments and the resulting magnetism on a paramagnet when an applied field is present. The susceptibility of a paramagnetic mineral will decrease with increasing temperature, a diamagnetic mineral has constant susceptibility with temperature and ferromagnetic minerals have complex changes in bulk κ with temperature (Borradaile and Jackson, 2004). The slope of a graph of induced magnetization, *M*, against field *H* gives κ (=*M*/*H*), the susceptibility. This is a straight line of positive slope for paramagnets and a unique line of negative slope (-14μSI) for diamagnetic minerals.

4.2.3 Ferromagnetism

Materials that display ferromagnetic properties acquire magnetism due to an external field that is parallel to the applied field and persists after the field is removed. This magnetism is referred to as permanent or remanent magnetization. Weiss (1907) explained ferromagnetism by suggesting the existence of an internal molecular field so strong that it brings atomic moments into nearly saturation alignment, producing a spontaneous magnetization (M_s). When discussing magnetic minerals of this magnetism, ferromagnetism *sensu lato* is used to distinguish the broad category. Ferromagnetism (*s.l.*) connects the spins of unpaired electrons in the 3d shell. Refer to Figure 4.1c-e to see the spin moments and net magnetism of a ferromagnetic material.

Different spin patterns in the 3d shell will create distinct magnetisms. These are described as ferromagnetism, ferrimagnetism, antiferromagnetism and canted antiferromagnetism. Dunlop and Özdemir (1997) showed that different domains with different

directions of M_s would have mutually compensating moments. Figure 4.3 shows these different combinations of exchange-coupled spin moments and the resulting net magnetism.

Ferromagnetism *sensu stricto* refers to the specific type of spontaneous magnetization, which occurs when the electron spins of adjacent cations are directly coupled in the same direction (Fig. 4.3a). Antiferromagnetic materials occur when the coupling force changes the electron spins so that the adjacent cations are reversed and two opposing magnetizations are created. This produces a net magnetization of zero (Fig. 4.3b). If for some reason a sublattice is more magnetic it will result in an imbalance within a grain and therefore give a net magnetization in the same direction as the dominant sublattice magnetization. This is termed ferrimagnetism (Fig. 4.3c). Magnetite is an important example of a ferrimagetic mineral. When a sublattice magnetic orientation is permanently deflected through a small angle (≈0.2°) in the absence of any external field, as described by Dunlop and Özdemir (1997), it is said to be a result of spin-canting. Canted antiferromagnetism (Fig. 4.3d) produces a weak resulting net magnetism perpendicular to the sublattice magnetization. Hematite displays this type of magnetism between the Morin transition, just below room temperature, and the ordering temperature, ~670°C (Dunlop and Özdemir, 1997).

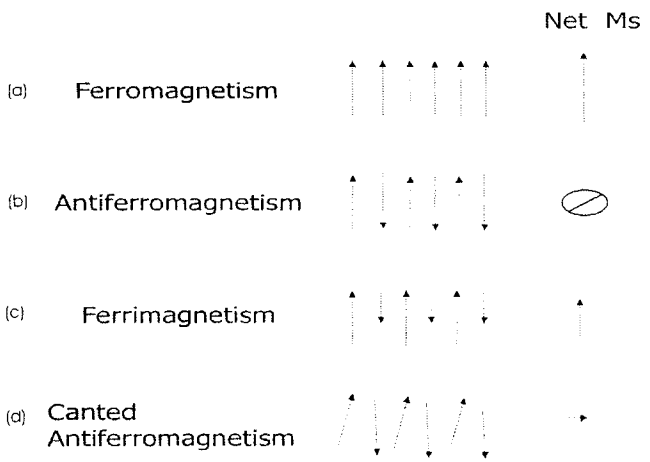

Figure 4.3. Different possible exchange-coupled spin structures and resulting net effect of magnetization of each. (Modified after Dunlop and Özdemir, 1997)

4.3 Anisotropy of magnetic susceptibility (AMS)

Magnetic susceptibility (k) that is measured in a weak field (H) vanishes when the applied field is removed ($\boldsymbol{M = kH}$). Since there are no permanent magnetization effects (induced magnetization only) the natural remanent magnetization is left untouched. AMS represents the anisotropic combination of the susceptibilities from all the minerals present within a rock sample. Since it does not affect or record the contribution of remanence, AMS also represents the

anisotropy of the petrofabric, often in a direct manner (Hrouda, 1982; Borradaile and Jackson, 2004). Note that the ferromagnetic (*s.l.*) minerals will have a greater 'weight' on the total or bulk susceptibility (κ) than silicates because their susceptibilities are comparatively high. Generally, all three types of magnetic minerals, diamagnetic, paramagnetic and ferromagnetic, are present and contribute to the observed susceptibility.

AMS is represented by a second rank tensor and is shown with a magnitude ellipsoid of magnetic susceptibility defined by the length and orientation of three eigenvectors, $K_1 \geq K_2 \geq K_3$. Second rank tensors can relate cause and effect for an anisotropy material (Borradaile, 2003) by describing the cause of anisotropy in three-axes (i or j=1,2,3). In the case of AMS, the second rank tensor describes a variation with orientation that is intrinsic to a specimen at a particular point and does not change when the referenced axes change (Borradaile, 2003). Figure 4.4 shows the components of a second rank tensor as stress with reference to an x_1, x_2, x_3 Cartesian reference frame.

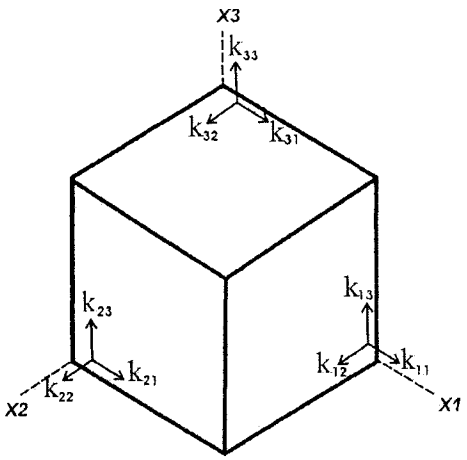

Figure 4.4. Nine components of a second-rank tensor k_{ij} in a frame of x1, x2, x3. k_{ij} acts along the j-axis and on the plane perpendicular to i. The eigenvectors (k11, k22, k33) are the principal directions of susceptibility where i=j. (Modified after Borradaile, 2003)

The AMS ellipsoid is coaxial to the petrofabric, meaning that the K_1 axis is parallel to the lineation and the K_3 axis is perpendicular to the foliation in the rock (Rochette, et. al., 1992). The mean orientation of the principal axes should be orthogonal and calculated using tensor-statistics (Jelinek, 1978; Borradaile, 2001). Tensor-statistics show the mutual interaction of the directional uncertainty of the mean principal directions (Jelinek, 1978; Lienert, 1991; Borradaile, 2001). The high susceptibility samples may deflect the orientation of the tensor-mean away from the majority (Borradaile, 2001). Normalizing the results will overcome this problem. However, high susceptibility 'outliers' may be significant and could demonstrate a subfabric.

Normalizing consists of taking each specimens tensor and dividing its principal magnitudes (k_{max}, k_{int}, k_{min}) by their geometric mean, or bulk susceptibility (κ) (Borradaile, 2001). This helps to define the subfabrics of accessory minerals and lower κ minerals and not be

outweighed by the high bulk susceptibility specimens or inclusions. Just a few grains of magnetite can dominate the whole rocks κ and therefore the AMS, which may have a matrix of paramagnetic silicates (Borradaile, 1988). Table 4.1 summarizes some of the minerals mentioned in this thesis and their bulk susceptibilities that have been reported by various sources. Figure 4.5 displays the effects of high bulk susceptibility.

Standardizing or normalizing is beneficial, but non-normalized results must still be taken into consideration. Since there is a possibility of conflicting subfabrics and different orientation distributions that can be revealed by normalized and non-normalized mean-tensors, it is best to view both results. Comparing the two will display most conflicts such as the influence of ferromagnetic (*s.l.*) minerals on the whole rock AMS. Also, the bedding fabric cannot be interpreted from a specimen's tensors if normalized. One specimen of large κ can skew the fabric towards its own principal axes. This is not to say the higher κ subfabric might not be the primary fabric, but it is not known until the normalized and non-normalized mean tensors are compared.

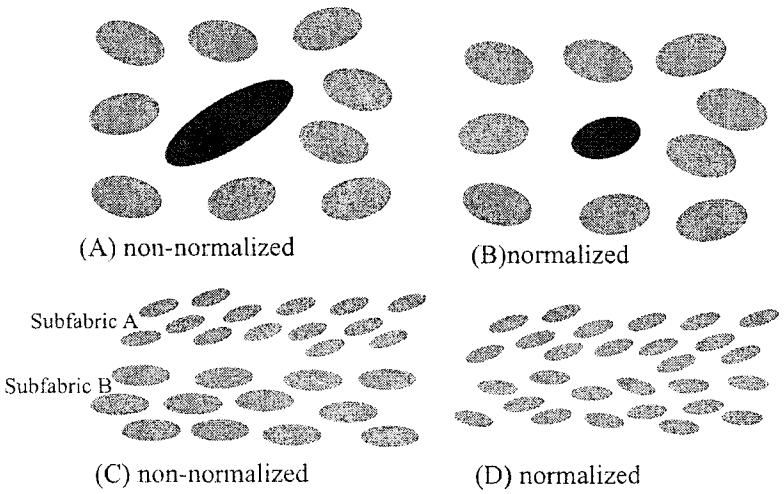

Figure 4.5. The different effects on AMS magnitudes on normalized and non-normalized specimens. The darker oval represents a ferromagnetic grain (showing subfabric A) within the paramagnetic and diamagnetic grains. (Modified after Borradaile, 2001)

Mineral Name	Bulk - k	kmax	kint	kmin	Reference
	(in 10^{-6} SI/vol)				
Actinolite	3560.4	1.076	0.982	0.947	1
Hornblende	8919	1.347	0.917	0.809	1
Chlorite	358	1.093	1.06	0.908	1
Biotite	998	1.107	1.096	0.824	2
Biotite	2500				3
Quartz	-13.4				4
Magnetite	5 841 000	1.063	0.989	0.951	1
Maghemite	0.001				5
Hematite	10 000				6
Pyrrhotite	1 500 000	1.306	1.003	0.767	1
Amphibole	2750				3
Tourmaline	1690				1
Serpentine	75 700				7

1) Borradaile, G., Keeler, W., Alford, C. and Sarvas, P., 1987. Anisotropy of magnetic susceptibkiby of some metamorphic minerals. Physics of the Earth and Planetary Interiors 48, 161-166.

2) Hrouda. F., Jelinek, V. and Zapletal, K., 1985. Use of magnetic properties of rocks in ore and petroleum geophysics (in Czech). Res. Rep. Geofyz. Brno, 54-75.

3) Borradaile, G. and Kukkee, K., 1996. Rock-magnetic study of gold mineralization near a weakly deformed Archean sysenite, Thunder Bay, Canada. Exploration Geophysics 27, 25-31.

4) Hrouda. F., 1986. The effect of quartz on the magnetic aniosotropy of quartzite. Studia Geophys. Geod. 30, 39-45.

5) Tarling, D.H., and Hrouda, F., 1993. The Magnetic Anisotropy of Rocks. Chapman and Hall, London, UK.

6) Uyeda, S., Fuller, M.D., Belshe, J.C. and Girdler, R.W., 1963. Anisotropy of magnetic susceptibility of rocks and minerals. J. Geophys. Res. 68, 279-291.

7) Lagroix, F.and Borradiale, G., 2000. Magnetic fabric interpretation complicated by inclusions in mafic silicates. Tectonophysics, 325(3-5), 207-225.

Table 4.1. Summary of bulk susceptibilities of some important minerals.

4.3.1 Preferred Crystallographic Orientation (PCO)

Most minerals in a rock express their AMS according to a preferred crystallographic arrangement (PCO). Crystals in a rock will have a preferred orientation. This orientation indicates the Kinetic processes which a rock may have undergone as magma flow or tectonic strain. These preferred orientations might be due to primary things as solid state deformation or magmatic flow. PCO's will have elongated grains with the maximum susceptibility along the long axes while the flat grains will have minimum susceptibilities perpendicular to the plane. This is an approximation since principal susceptibility axes are only parallel to crystal axes in minerals of high symmetry (Borradaile and Jackson, 2004).

4.3.2 Preferred Dimensional (Grain-Shape) Orientation (PDO)

Magnetite is one of the minerals to have an AMS defined by **grain shape anisotropy** and not *crystallographic structure*. This is because its bulk susceptibility is so high (2-3 SI). Any mineral with $\kappa \geq 0.2$ SI has the potential to show shape-controlled AMS. There are different magnetic responses in minerals such as magnetite and maghaemite, named multi-domain (MD), pseudo-single domain (PSD), single domain (SD) and superparamagnetic (SP). Different boundaries within these varying dimensions have an effect on the anisotropy of the mineral. MD grains of magnetic minerals will contain several magnetic domains (≥ 4) separated by a wall that is moved when a weak magnetic field is applied. Grains of magnetite that are MD are usually in the size range of >3μm. In PSD a magnetic domain behaves as a single-domain particle. There are usually 6 to 2 domains in a PSD grain. A SD grain contains only one ordered magnetic domain. In magnetite the upper limit for SD is around 1μm, depending on shape. Hematite has a domain size of about 1cm. This implies that most hematite is SD. SP grains are ferromagnetic (*s.l.*) but have strong paramagnetic properties and will lose any remanence they may have obtained, over a few minutes. Figure 4.6 shows the MD, SD, PSD and SP dimensions.

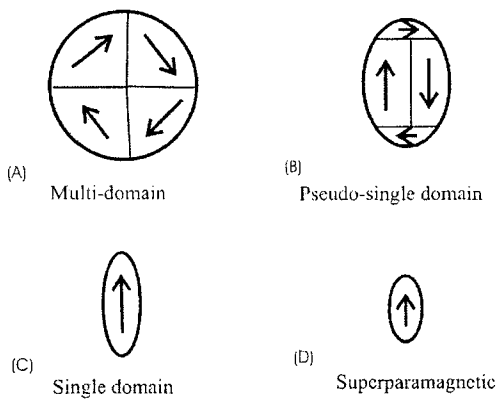

Figure 4.6. The different dimensions possible in various minerals, especially magnetite.

In MD and PSD magnetite the maximum susceptibility, (k_{max}) can be found parallel to the long axes, x, of the ellipsoid much like the crystallographic controlled magnetic fabric. However, in SD magnetite the minimum susceptibility (k_{min}) is found parallel to the x axes. This is referred to as an inverse AMS fabric and will be explained in detail in the section 4.3.4 (Fig. 4.8).

4.3.3 Whole rock and specific minerals AMS

The orientation-distributions of remanence-carrying inclusions in minerals are of a large importance when studying the palaeomagnetism of a rock as well as its magnetic fabric (Borradaile and Henry, 1997). As Figure 4.7 displays, silicates may be aligned in one direction

with inclusions of greater magnetic susceptibility either in a different orientation or simply a random orientation. This can influence the overall AMS to show the orientation of the inclusions, rather than the desired information on the orientation of the silicate fabric.

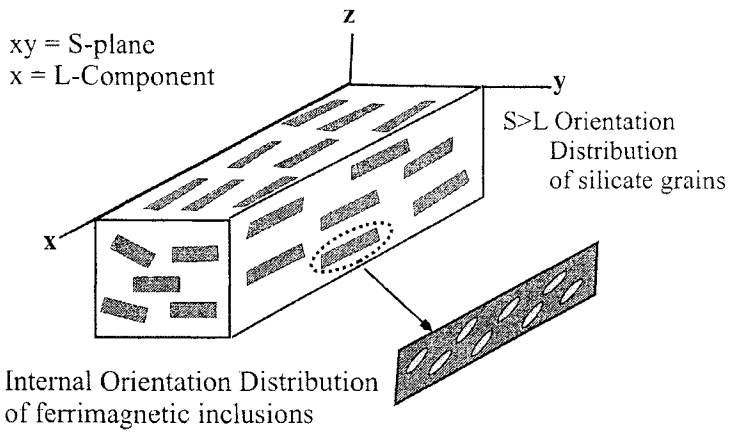

Figure 4.7.
Representation of a rock with a combined fabric of silicate minerals and iron oxide minerals, defining the petrofabric. Each silicate mineral contains a subfabric due to the magnetic inclusions. (Modified after Borradaile and Henry, 1997)

Different orientation-distributions of various minerals within a rock will affect the AMS, each in their own way. If all minerals (crystals and matrix) are generally aligned in the same direction and of a similar susceptibility, the AMS will show the magnetic fabric and that of each mineral. This is the simplest of examples. A single specimen ellipsoid can characterize this orientation distribution faithfully (Borradaile, 2001). It will represent the "mean fabric". However, most rocks will have higher susceptibility Fe-oxide minerals and variations in alignment with different minerals. Therefore, AMS ellipsoids will vary in shape and orientation from specimen to specimen (Borradaile, 2001). This will cause a number of AMS sub-fabrics to be blended into an overall rock-AMS fabric.

4.3.4 Magnetic fabrics

The magnetic fabric controls the shape and orientation of the susceptibility ellipsoid and is defined by the ferromagnetic minerals within the specimen. Figure 4.8 illustrates the S and L fabrics (originally introduced by Flinn in 1965) and the corresponding susceptibility principal axes on a stereoplot as well as the orientation distribution within a sample. The S-tectonite has an ellipsoid that is defined by x=y>>z and is oblate (i.e. pancake shaped) whereas the L-tectonite is defined by x>>y=z and is prolate (i.e. more rod shaped). S and L fabrics are shown best in a lower hemisphere stereographic net projection.

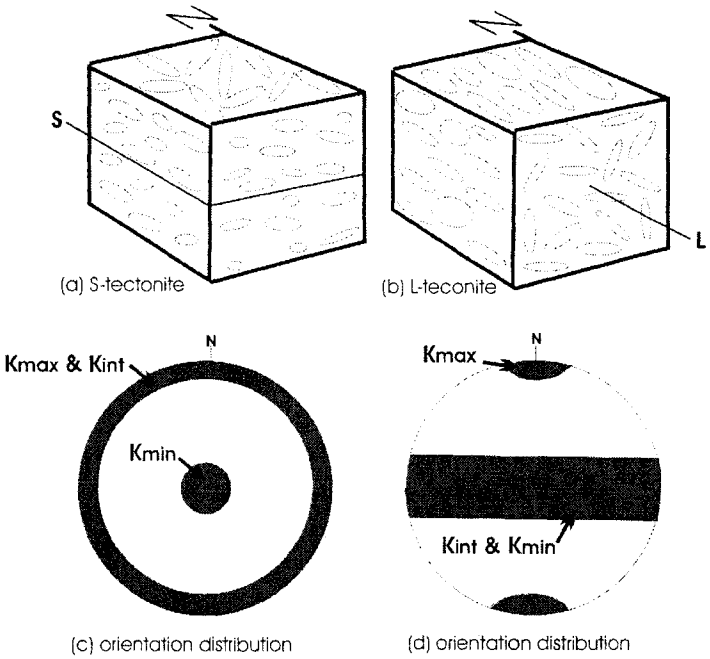

Figure 4.8. (a) and (b) show the S and L fabrics respectively which correspond to (c) and (d) orientation distributions respectively (Modified after Flinn, 1965; Borradaile, 2001, 2003).

Normal magnetic fabrics are most commonly observed. Normal fabrics will have k_{max} parallel to the x-axes and k_{min} parallel to the z-axes. The magnetic axes follow the principal crystallographic axes. The interactions between ferrimagnetic grains and the fabric of SD magnetite will result in an inverse fabric where k_{max} will parallel the z-axes and k_{min} will parallel the x-axes (Rochette, 1988). In an inverse fabric the F and L are opposite to a normal fabric. An inverse planar fabric is defined as $k_{max} > k_{int} \sim k_{min}$ and $L \geq F$. Therefore, k_{max} is perpendicular to foliation and k_{min} is parallel to the linear orientation distribution. Figure 4.9 illustrates the dimensions of the magnetic susceptibility ellipsoid for both a normal and inverse fabric.

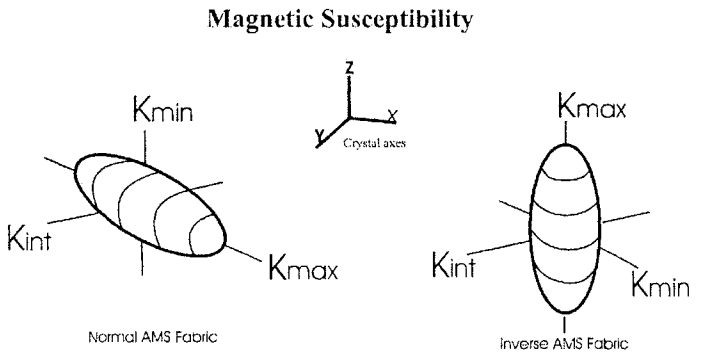

Figure 4.9. Shows the dimensions of MD and SD magnetite resulting from preferred orientation distribution (normal magnetic fabric) or preferred dimensional orientation (inverse magnetic fabric). (Modified after Ferré, 2002)

The mixing of normal and inverse fabrics produce what is known as intermediate magnetic fabric (Rochette et al., 1992, 1999), less ambiguously referred to as a blended fabric (Borradaile and Jackson, 2004). Blended fabrics arise where the orientation of two or all three principal axes of the ellipsoid are interchanged for different minerals, which may be due to other sources then mixing (Ferré, 2002). The minimum proportion of an inverse component necessary for the onset of a blended fabric depends greatly on the shape of the normal component, the shape of the inverse component, and the anisotropy of the inverse component (Rochette et al., 1992). Ferré (2002) states that the resulting anisotropy from a blended fabric is systematically lower then that of either a normal or inverse magnetic fabric.

Co-axial blended fabrics will have a magnetic ellipsoid with the following properties:

$$k_{max} = (1\text{-}i)\, k_{max} + i\, k_{max(i)}$$

$$k_{int} = (1\text{-}i)\, k_{int} + i\, k_{int(i)}$$

$$k_{min} = (1\text{-}i)\, k_{min} + i\, k_{min(i)}$$

where i is the proportion of the inverse component.

4.4 Methodology

Determining the anisotropy of the 145 oriented cores used for AMS in this study, was done by measuring the susceptibility along seven axes using the Borradaile-Stupavsky orientation scheme. The Borradaile-Stupavsky scheme yielded an even, directional sampling of the hemisphere and allowed for precision of low susceptibility, heterogeneous samples (Borradaile and Stupavsky, 1995; Borradaile and Henry, 1997). Figure 4.10 illustrates these seven directions. The AMS measurements were determined with the use of the Sapphire Instruments SI2 susceptibility meter. Error ("noise") for this instrument was less than 0.2 μSI for each measurement (Borradaile and Stupavsky, 1995). The low field produced by the SI2 was approximately 1 oersted and oscillated at 19 200 Hz. All measurements were then processed using the SI201.EXE program written by Dr. G. Borradaile.

AMS ellipsoid shapes are best plotted according to the method of Jelinek (1981), which uses the shape parameter (T) and the degree of anisotropy (P_j) as Cartesian graph axes. The anisotropy degree and its shape were best defined in terms of (T) and (P_j) respectively. On the Jelinek plot, oblate shapes would have a positive T value, approaching +1, whereas prolate shapes would plot as a negative T value, approaching –1. Neutral ellipsoids plotted at T=0.

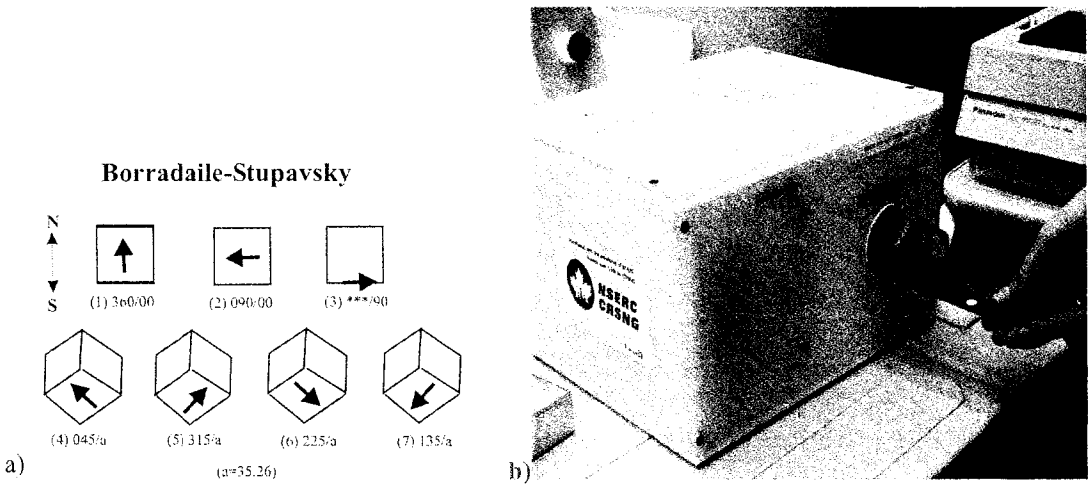

Figure 4.10. (a) Cubical representations of specimens in the holder in plan view for the different measurements of AMS along the N-S axis. (b) Specimen inserted in AMS unit in orientation #5.

Traditionally, but not effectively, the Flinn diagram plots AMS fabrics like strain ellipsoids on a Cartesian graph. In this plot 'a' is the length of the major axis divided by the length of the intermediate axis, and 'b' is the length of the intermediate axis divided by the length of the minor axis. In Jelinek's plot the lineation and foliation are defined quantitatively, where L (lineation)=k_1/k_2, F (foliation)=k_2/k_3, and P (degree of anisotropy)=k_1/k_3 (Jelinek, 1981). Flinn's L and F are purely qualitative descriptors of the relative dominance of prolate (L) or oblate (S) fabric, associated with mineral lineation or schistosity, respectively. The shape of the tensor means and magnetic fabrics are read from a Jelinek plot easiest, whereas the strain is viewed best in a Flinn-type plot.

Borradaile and Jackson (2004) introduced an alternative way to view tensor parameters and representation, the Borradaile-Jackson polar plot. These authors addressed problems with the conventional graphing techniques of Jelinek and Flinn, particularly those concerning the shape of the magnitude ellipsoid expressed as its degree of prolateness or oblateness as well as the measure of the eccentricity of the ellipsoid. In structural terms the constricted ellipsoid shapes would lie between neutral and prolate and the flattened ellipsoids would lie between neutral and oblate but it is not so simple in magnetic anisotropy terms (Borradaile and Jackson, 2004). The Borradaile-Jackson plot offers to eliminate these problems by intruding a $\pi/4$- segment polar plot, where P_j is the radius and T is the arc-length. Figure 4.11 shows and compares AMS tensors on the newer Borradaile-Jackson plot to Jelinek and Flinn plots for the 145 core samples used in this study. Isotropic fabrics plot uniquely at the origin whereas they are smeared along the y-axis of a Cartesian plot of Jelinek's parameters.

Strain and susceptibility ellipsoids may be plotted and compared on a stereonet, after the AMS measurements, in order to correlate between the strain and magnitude of susceptibility

(Borradaile, 1991). On a stereonet an oblate ellipsoid would have its maximum and intermediate axes within a 90° girdle from its minimums grouped in the centre. A prolate ellipsoid would have its maximum axes grouped and the intermediate and minimum axes in a girdle 90° from the maximum direction.

The AMS stereonet plots (Fig. 4.14) were made for the total 145 CY-4 cores, in addition to the plots of each lithology unit; sheeted dikes, lower and upper gabbro and websterite. The bulk susceptibility was also plotted (Fig. 4.12) vertically from the top of the drill hole to the bottom to help interpret the differing magnetic responses throughout the CY-4 drill core.

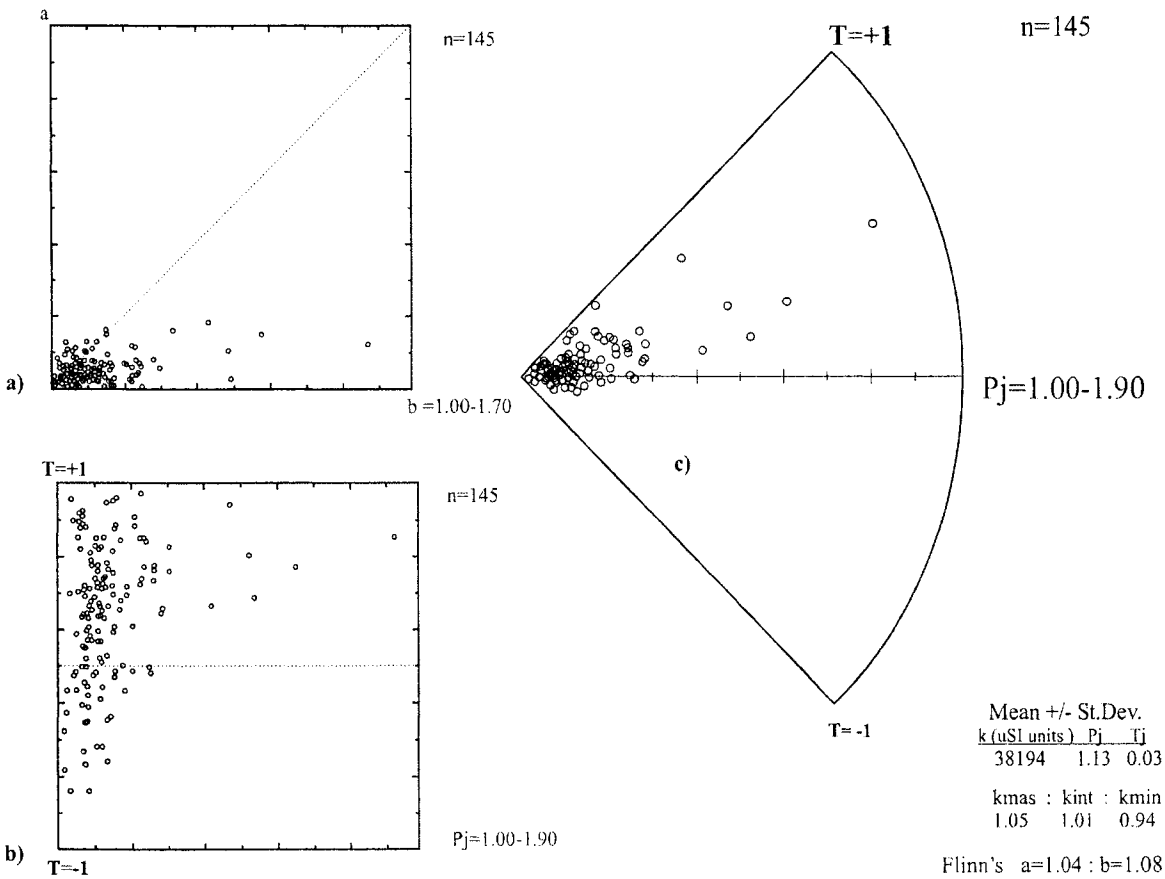

Figure 4.11. Anisotropies plotted in three different ways a) Flinn, b) Jelinek and c) Polar or Borradaile-Jackson plot. Without reducing the scale of P_j the Jelinek plot displays the magnitude of the fabric and its shape best compared to the other plots. However, all three plots do show a majority of oblate shaped fabrics.

4.5 Results

In order to compare the results from different magnetic methods with no bias the CY-4 drill hole was divided into 4 broad zones, based on lithology. The κ given by the average susceptibilities of the 7 measurements determined by AMS, defines the 4 zones very well. Figure

4.12 shows the distribution of κ through these zones. Each point on the graph is an arithmetic mean taken from 2 to 5 measurements for that depth.

The first unit from 0-600 m was made up of diabase dikes. The κ for this zone was the highest for the CY-4 drill hole ranging from approximately 27, 000 to 153, 000 μSI. From 600-1180 m the κ was representing gabbro, gabbronorite and a few diabase dike sections, indicated by the spikes in κ. This second zone had a low value of 1, 500 μSI and a high of about 70, 000 μSI. From 1180-1800 m the low κ was due to the massive gabbronorite. They ranged from 1, 000 to 15, 000 μSI. The last zone corresponded to the ultramafic rocks with a κ ranging from 500 to 17, 000 μSI, with one spike to 67, 000 μSI in the bottom sample used in this study.

The lowest values of κ correspond to the gabbros, which were generally isotropic. The high values at the top of CY-4 were due to the accumulation of Fe-oxides in the dikes during hydrothermal alteration. The one high value at the bottom of CY-4 was likely a result of serpentinization.

Histograms of the κ for the three main lithology groups, diabase dikes, gabbroic rocks and ultramafic rocks, are shown in Figure 4.13. The histograms show the large range of susceptibilities in each group. The diabase dikes (Fig. 4.13a) histogram show no overall pattern but displays three populations whereas the log 10 distribution of κ shows one main population at about 4.5. The gabbro lithology group (Fig. 4.13b) shows a steady decrease in frequency as κ values increase with no defined main population in the histogram. The log 10 distribution shows one population at approximately 2.5 and a less pronounced population at about 4. The ultramafic group's histogram (Fig. 4.13c) shows a similar pattern to the gabbroic rocks with the large decrease in frequency with increasing κ, only in this group there is a population visible after the initial drop in frequency. The log κ graph also shows similarities with the gabbroic rocks. There is a main population shown at about 2.5 and a less predominate population at about 4.

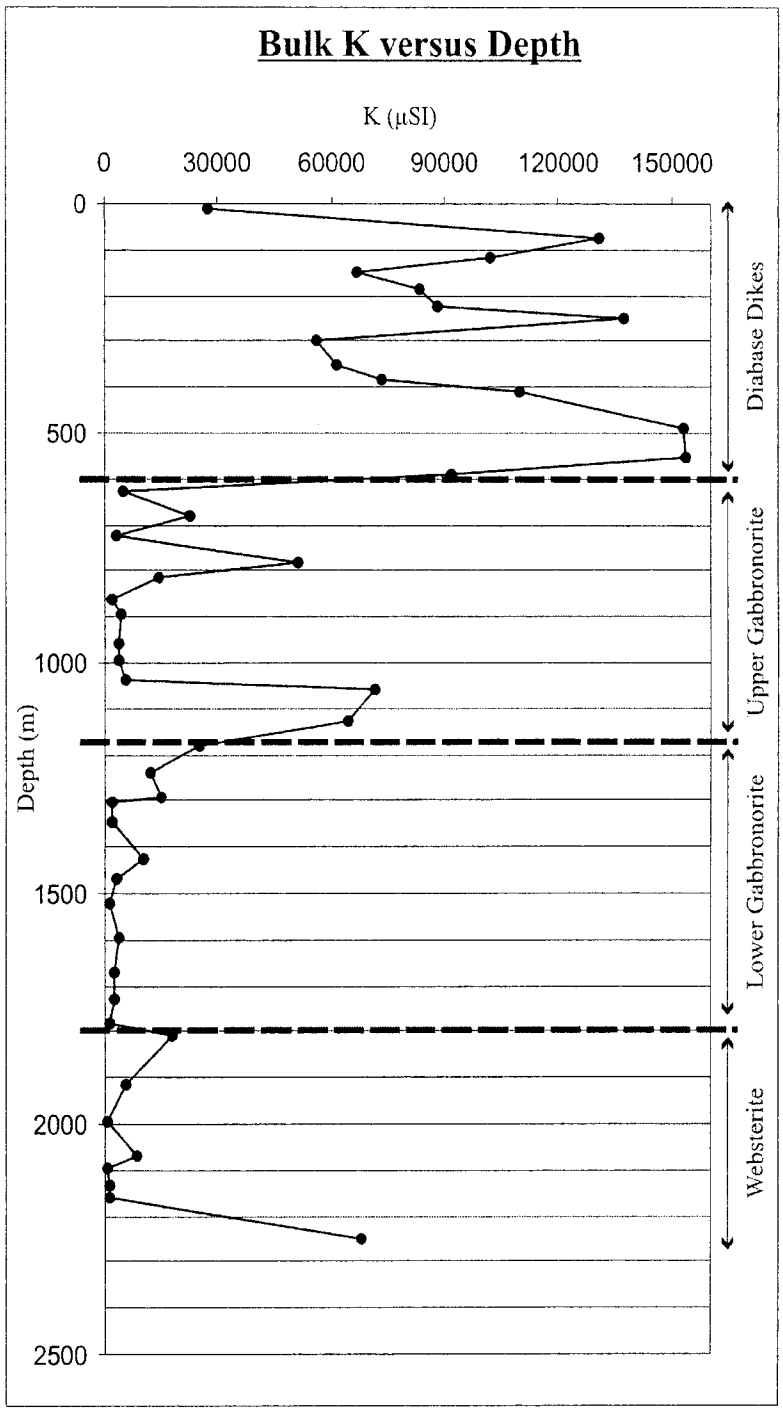

Figure 4.12. Distribution of κ down CY-4. The four susceptibility zones seen here are related to the changes in the lithology units.

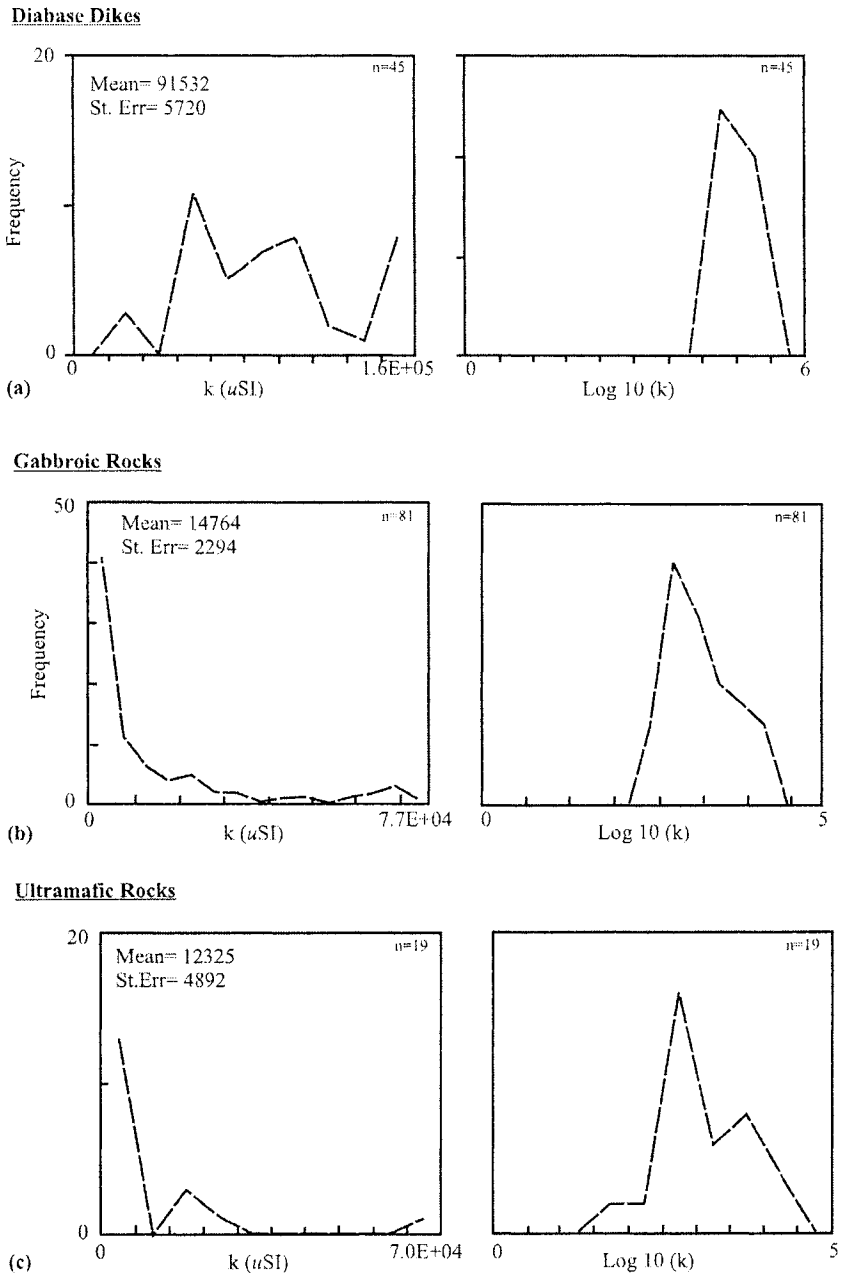

Figure 4.13. Histograms for the bulk susceptibilities of the 3 major lithologies found within the CY-4 drill hole. The log 10 diagrams of each histogram are shown to the right of each histogram. (a) κ distribution for diabase dikes. (b) κ distribution for gabbroic rocks. (c) κ distribution for the ultramafic rocks.

The tensor means and magnetic fabrics determined by AMS for this study are shown in Figure 4.14. Lower hemisphere stereonet projections for all the CY-4 samples were compared to the steronets of the 4 individual zones. The maximum, intermediate and minimum tensors are indicated by a square, triangle and circle, respectively. The sub-elliptical zone around a tensor is a 95% confidence cone about the tensor's mean axis.

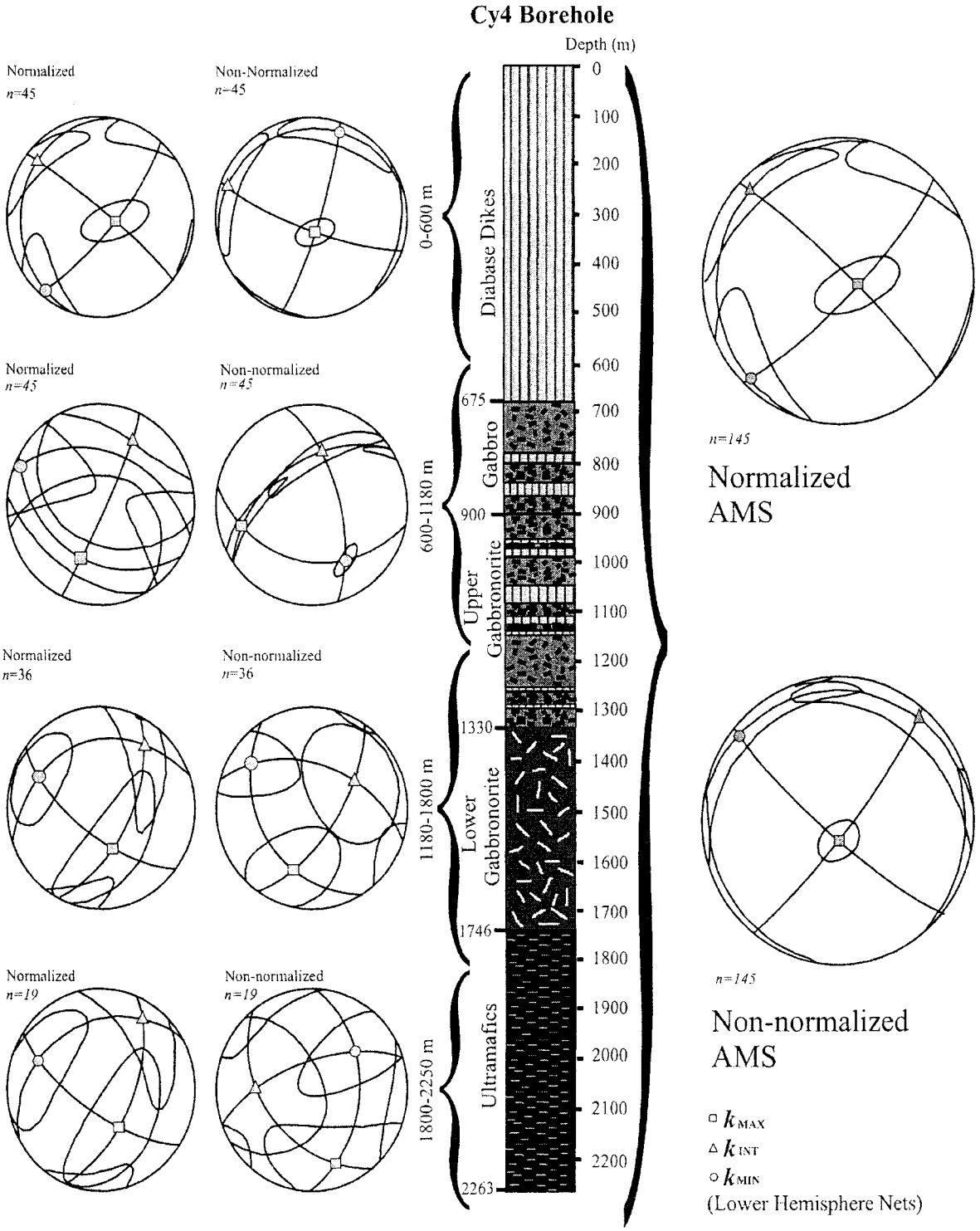

Figure 4.14. The tensor means display the magnetic fabrics in the above diagram. The stereonets for all cores are along the right side of the stratigraphic column. To the left are the stereonets for each lithology group.

Mean tensors of the principal susceptibilities for all 145 CY-4 samples in both the normalized and non-normalized stereonets displayed a strong vertical fabric designated by the small 95% confidence cones around κ_{max}. Since κ_{min} was horizontal and azimuthally dispersed, it implies a weak vertical foliation. The overall fabric for the CY-4 drill hole was L>S (Fig. 4.11c).

A similar orientation distribution to the overall fabric was seen within the sheeted dikes (0-600 m). The normalized and non-normalized mean tensors of the 45 dike samples showed a strong vertical fabric with tight confidence cones around κ_{max}. The κ_{int} and κ_{min} girdles elongated towards each other, although less pronounced than seen in the combined lithology tensors, they displayed a horizontal schistosity. Both the normalized and non-normalized stereonets for the sheeted dikes were L>S fabrics. The κ_{min} for the normalized and non-normalized stereonets were subhorizontal NE-SW and κ_{max} nearly vertical.

In the upper gabbro and gabbronorite zone (600-1180 m) the 45 samples displayed a weak fabric in the normalized stereonet and there was no distinct orientation displayed since all 95% confidence cones overlapped. However, in the non-normalized stereonet a strong S>L fabric was shown by the small confidence cone around κ_{min}. The plane to the κ_{min} mean tensor (foliation) seen at approximately 045° and could be related to the dikes, found to have an average strike around 040° in outcrops surrounding and to the south of CY-4. Since the ferromagnetic minerals mainly influenced the non-normalized mean tensors, the fabric observed in this zone was due to the periodic occurrence of high κ dikes and their strong magnetic foliation.

The lower gabbronorite zone (1180-1800 m) of 36 samples exhibited a weak S>L fabric for the normalized mean tensors. The foliation in the normalized stereonet was parallel to the strike of the Mitsero graben. In the non-normalized stereonet the confidence cones were touching but not overlapping. The non-normalized stereonet in this zone showed a typical mantle flow fabric, S=L.

At the bottom of the CY-4 drill hole 19 samples were measured. In the normalized stereonet a weak S>L fabric was displayed, again parallel to the Mitsero graben. In the non-normalized stereonet the girdles were all overlapping one another and no fabric was defined. The lack of fabric could be a representation of a mantle flow.

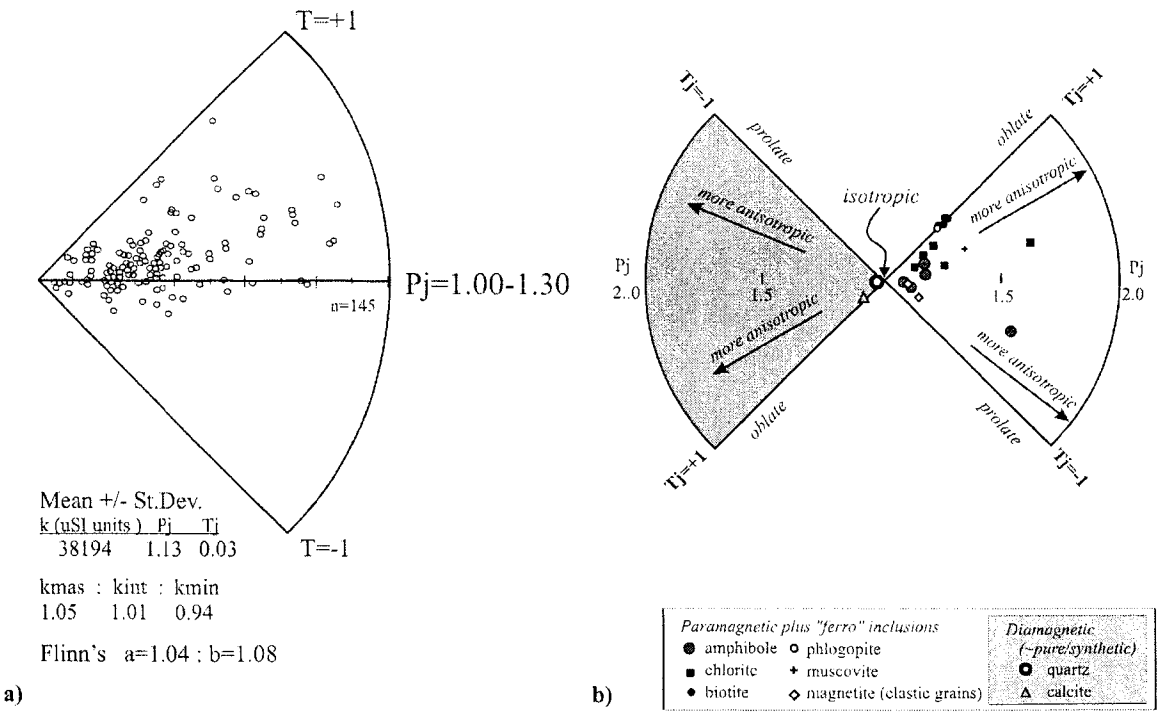

Figure 4.15. a) The Borradaile-Jackson plot with the magnifation of P_j (P_j=1.00-1.30), to better examine the 145 CY-4 drill hole samples. This shows the main fabric to be oblate with a few prolate fabrics that fall close to T=0. b) AMS of common minerals and the effects on them due to concentration on a polar plot by Borradaile and Jackson, 2004.

The CY-4 samples (shown in Fig. 4.11 and Fig. 4.15a) showed a strong oblate fabric where the mean P_j =1.13. This range of P_j is typical for anisotropic chlorite, biotite and amphiboles when compared to Figure 4.15b. There were prolate fabrics observed but they fell relatively close to a sphere (T=0) and did not have an extreme eccentricity. These prolate fabrics are expected be the contribution of the magnetite.

In summary, the AMS results showed a strong correlation between the overall tensors and the top 600 m of the CY-4 drill hole. This would indicate that the sheeted dikes were the main factor in the tensor data and may have overshadowed the contribution of other lithology units in the overall results. The ferromagnetic minerals in the upper gabbroic rock showed a strong subfabric, which may be due to the diabase dikes and their foliation. At the bottom of the CY-4 drill hole, in the lower gabbroic and ultramafic rocks, there were no strong fabrics seen. The 95% confidence cones became large enough so that they all overlapped, indicating a mantle flow fabric with no specific lineation.

Chapter 5. Critical Temperature Points

5.1 Introduction

The Curie balance, Sapphire Instruments 6, was one of the instruments used in this study to determine which iron oxide minerals were present in the CY-4 drill hole from thermomagnetic curves of saturation remanence at different temperatures. The magnetic mineralogy in the oceanic crust depends mostly on the composition and cooling rate of the magma from which it originated. Rapidly cooled basaltic lava will preserve titanomagnetite with an intermediate titanium composition (TM_{60}), whereas slower cooled lavas above 150°C will preserve exsolutions texture of illmenite and magnetite lamellae (O'Reilly, 1984).

A Curie balance was used to heat a mineral separation in which the "ferro"-magnetitc mineral fraction had been enhanced, thus permitting measurement of the Curie or Néel temperatures of the oxide minerals. From the thermomagnetic curves the Curie temperature (T_C) can be defined as the critical temperature at which where a mineral's remanence becomes saturated in an applied large field and all magnetic moments become ordered to maximize the saturation magnetization M_s. As the temperature rises, thermomagnetic energy randomizes the spin moments until M_s=0, at the T_C. It is a critical point because at the T_C the spin structure is randomized by thermokinetic energy (O'Reilly, 1984) and all permanent remanence is lost. Remanence is recovered as the sample cools since there is no magnetic shielding. However, the remanence recovered after cooling is usually << M_s (O'Reilly, 1984) due to oxidation during the heating part of the experiment. Common minerals that have T_C's are ferromagnetic magnetite and titanomagnetite. The Néel temperature (T_N) is the critical temperature point for antiferromagnetic minerals such as hematite, ilmenite and goethite. The critical temperature points that were found during this study to characterize the iron oxide mineralogy of the CY-4 drill hole are all T_C.

5.2 Methodology

Before work on the Curie Balance began, 21 mineral separations were prepared for this method. Pieces of the core were broken off then crushed with a metal hand crusher to approximately 3 mm sized chips and subsequently put into an agate mill to crush and liberate individual mineral fragments between –100 and –200 mesh size. Between every five samples silica sand was run through the agate mill to clean the mill. Each fine sifted separation was washed in cool water until it ran clean of dust and then dried in a warm oven at <100°C. The mineral aggregate was then spread out and a large magnet was dragged over it to separate the magnetic minerals. It was common for a few silicate grains to stick to the "ferro"-magnetic

grains so the high-graded magnetic separation separated power was not always necessarily pure. This caused minor problems. The problems caused some of the sample results to be discarded since the silicate minerals caused difficulties on the graph and critical points were not clearly visible.

A sample of pure magnetite was run in the Curie Balance several times to calibrate the instrument. This found the most sensitive range for the position of the LVDT (linear variable differential transducer), which detects the motion of the sample holder due to temperature change. The machine was calibrated so that the critical temperature point for pure magnetite was 582°C. Once calibrated the unknown samples were then studied.

In the Curie balance instrument the sample was suspended in a Vycor tube as a horizontal swing-balance. This was attracted to a Neodymium (Nd) solid state magnet (H~600mT). A small furnace heated the specimen and as its saturation magnetization (M_s) decreased with temperature, the LVDT (linear voltage displacement transducer) recorded the displacement of the specimen as it swung away from the magnet. The hanger was adjusted from the front panel of the machine horizontally and vertically on x, y and z axes using micrometer screw controls to ensure it was located at the most sensitive range of LVDT values before the experiment began. The mineral separation went into a tube, which slid into the suspended hanger. The average specimen weight was approximately 0.030g. The Nd magnet was located at the rear of the instrument in line with the holder. The furnace wrapped around the specimen holder and was enclosed in a cold water jacket fed from a water faucet. Figure 5.1 illustrates the SI 6 Curie Balance and the general set up.

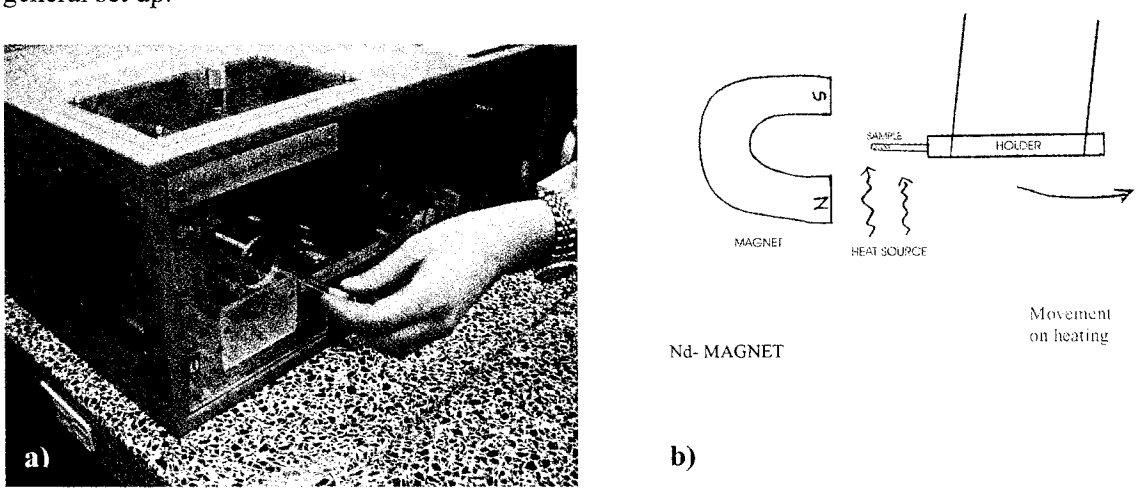

Figure 5.1. a) Photograph of the horizontal translation Curie Balance shows the SI-6 front panel and sample tube. b) The sketch illustrates, in a simplified way, the way in which the Curie and Néel points were obtained. A large magnetic field is applied and measurements of the position of the sample at different temperatures are recorded electronically by the LVDT. As a sample heats up, remanence decreases and the sample falls away from the magnet.

The variations in saturation magnetization (M/M_o) were measured as the specimen was heated in the Curie balance. The magnetization is saturated for most ferromagnetic minerals by the field of the Nd-magnet There may be more than one T_C or T_N, corresponding to different minerals in a specimen. The M/M_o value decreases as the grains were heated, indicating a loss of remanent magnetism. At critical temperatures there may be distinct drop in the M/M_o value, defining a T_C or T_N. As the grains cooled, M/M_o increases back along a similar path to the heating curve. However, the curve was commonly slightly lower since the heating caused oxidation that produces minerals with lover SIRM such as hematite.

5.3 Results

The results from the Curie Balance were observed on thermomagnetic graphs which plotted the normalized intensity of magnetization M/M_o, as the y-axis, where M_o represents the initial magnetization. This was plotted against temperature in degrees Celsius on the x-axis. The graphs showed the change in M/M_o on heating and cooling curves. Any sharp decrease in M/M_o on either curve indicated a critical point, usually characteristic of a specific iron or iron-titanium oxide. The difference between the heating and cooling curve indicated the amount of oxidation or alteration that occurred during the experiment. For this study a maximum temperature of 700°C was used. Most minerals reach their T_C or T_N before 700°C. Some of the mineral separations were contaminated with hydrous minerals such as amphibole. This created 'noisy' graphs due to the large amount of alteration that took place upon heating and no results could not be obtained. These samples underwent refined magnetic separation and the thermomagnetic experiment was repeated. Examples of the Curie Balance graphs are shown in Figure 5.2.

All of the critical points identified from Curie Balance graphs were plotted on a temperature versus depth graph (Fig. 5.3a). This graph differentiates four different populations representing TM_{60} (original), oxidized TM_{60}, magnetite and hematite, in order of increasing critical temperature. In figure 5.3b a histogram is used to emphasize these four main iron oxide populations. Notice that magnetite and hematite have the highest frequency, followed by oxidized TM_{60} then original TM_{60}.

The Curie or Néel temperatures used in this study were extracted from a graph in Figure 5.3c, which indicated the temperature at which saturation should occur for the various iron and iron-titanium oxides. TM_{60} is indicated on the graph by a dot at 150°C. This T_C increased as oxidation occurred, as seen on the graph. Magnetite was shown to have a T_C at 582°C and hematite had a T_N at 675°C on the graph.

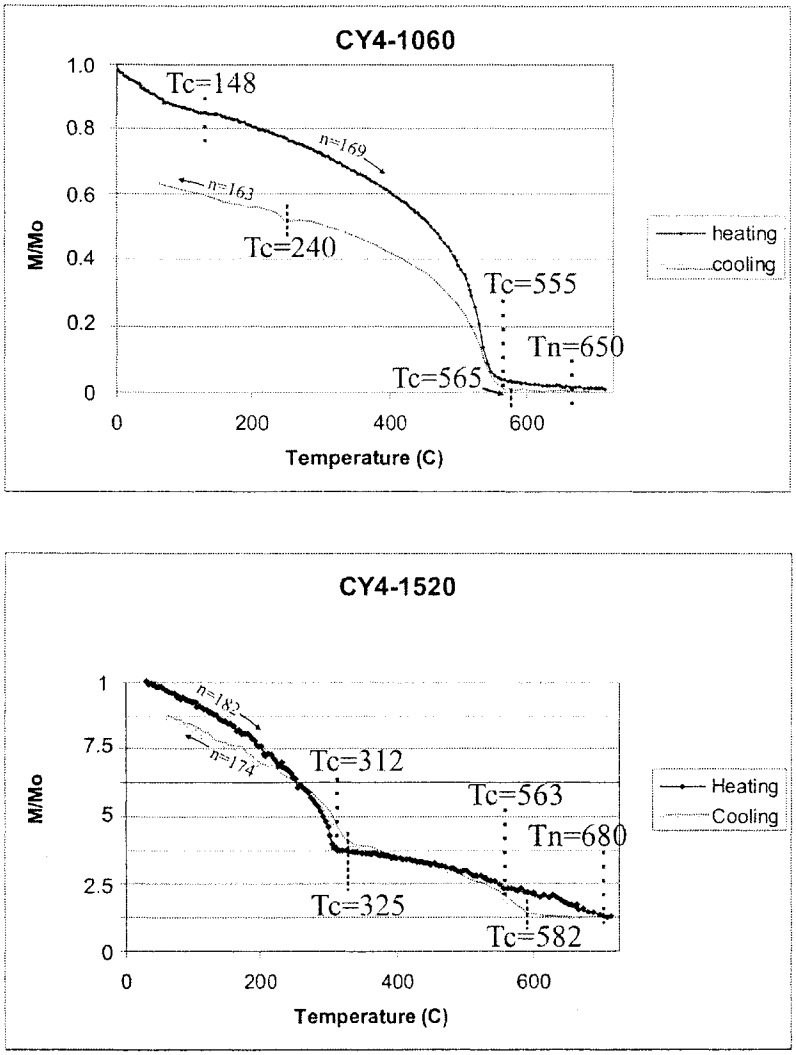

Figure 5.2. Two examples of Curie Balance graphs. The depth of the sample in the drill hole is given at the top of the graph (i.e., 1060 m and 1520 m). The critical temperature points are indicated with a vertical line and the temperature at which the inflexion point occurred. The critical points for the heating curves are shown above the curve and points corresponding to the cooling curve are below the curve. Notice the cooling curve is lower then the heating curve in intensity due to the oxidation of the original minerals in the specimen, during the experiment.

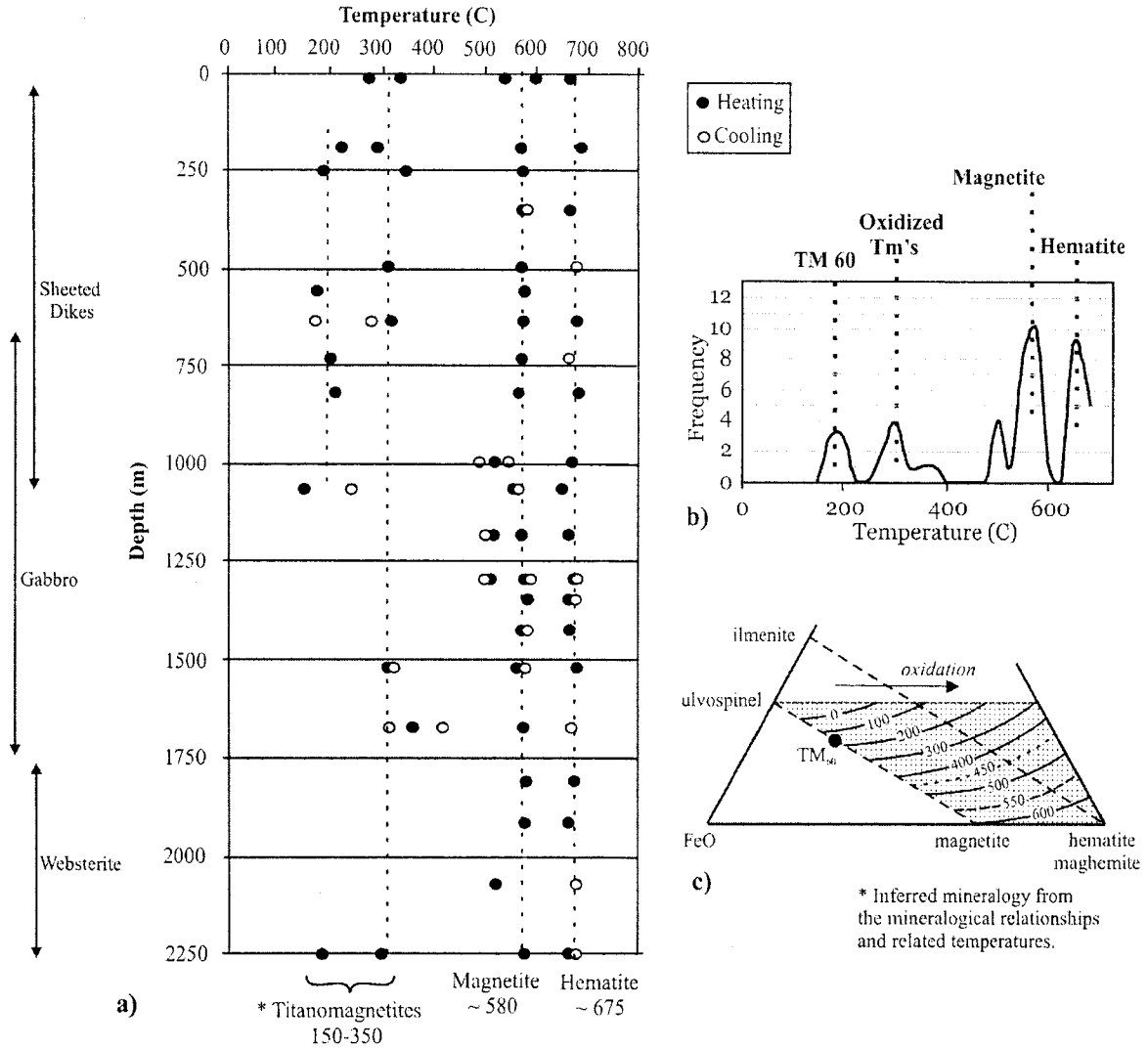

Figure 5.3. Combined results of Curie and Néel temperatures down the CY-4 drill hole. a) The inferred mineralogy for each population is given at the bottom of the graph. Filled in circles indicate critical temperature points taken from the heating curve and open circles represent those from the cooling curve. b) A histogram to indicate the main populations found in the CY-4 drill hole during heating. c) Graph taken from O'Reilly (1984) to show where the critical temperatures used in this study originated from.

The majority of the samples showed an inflexion point at 582°C, representing the iron oxide magnetite. Another point at 675°C was also seen in most samples, indicating hematite. Hematite was a common by-product of heating and, therefore, its concentration was often enhanced during cooling. Hematite has a lower M_s than the other iron oxides; consequently it lowers the cooling curve. Multiple heating of each sample may add confidence in stating that there was hematite present in the original sample but enhanced during the experiments. However, samples were only heated once in this particular study. The TM_{60}, found at a critical temperature point of about 200°C, was seen to exist to a depth of 1060 m. The original or 'fresh' TM_{60} T_C's were limited to the dikes. As the titanium-iron oxides were exposed to seawater through

hydrothermal circulation they were altered. The resulting oxidized TM_{60}, indicated by a higher T_C at 300-350°C, was found from the top of the drill hole to approximately 650 m and then again in a small interval from 1500-1700 m. This lower level intermission of oxidized TM_{60} may be indicative of an area where the hydrothermal fluids traveled down a fracture or a more permeable area. The TM_{60}'s seen at the bottom of the drill hole were a result of serpentinization.

Chapter 6. Magnetic Hysteresis Measurements

6.1 Introduction

As discussed in chapter 4, in ferromagnetic grains domains exists (Fig. 4.6) as a means of reducing the magnetostatic energy. Landau and Lifschitz first recognized the magnetostatic or demagnetizing energy in 1935. They found that over time the dipole-dipole interactions between atomic moments in a material would generate a demagnetizing energy that would eventually outweigh the natural exchange forces and rearrange to produce a uniform magnetization. In a MD grain, M_s is uniform within each domain but M_s vectors are in different directions in different domains (Dunlop and Özdemir, 1997). Figure 6.1 illustrates two possible configurations for the same grain. In a SD grain (Fig. 6.1a) the large surface area on the grain creates a high density of poles and therefore a large magnetostatic energy (Dunlop and Özdemir, 1997). In a MD grain (Fig. 6.1b) the grain has long plate-like domains that have short and tight surface poles and therefore generates little magnetostatic energy (Dunlop and Özdemir, 1997). As a grain changes from SD to MD the demagnetizing energy decreases, as seen in Figure 6.1. This is because the formation of magnetic domain will decrease the percent of surface covered by magnetic charges and charges of opposite sign are adjacent rather than separated (Butler, 1992).

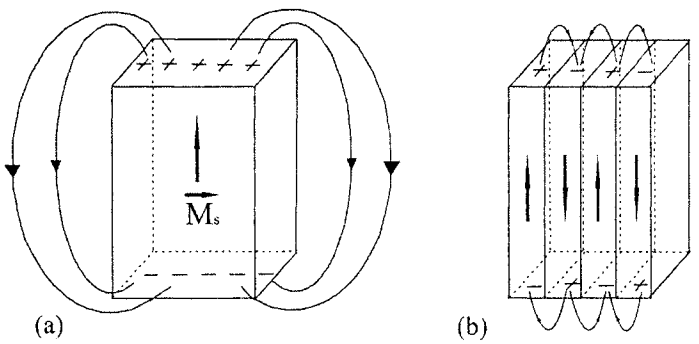

Figure 6.1. Alternative domain structures for the same grain. (a) single-domain structure with large + and – poles, linked by large external flux loops. (b) Four-domain structure with more localized flux linkage at surface poles. (Modified after Dunlop and Özdemir, 1997)

Magnetic hysteresis is used to classify the ferromagnetic minerals by identifying the grain size or domain state by measuring a sample's coercivity, magnetic saturation and remanence properties. The grain size refers to the behaviour of the magnetic domains and not the actual grain size dimensions. When an external field is applied to a material, changes occur as a result of the re-organization of domain walls to reduce the internal stress and demagnetizing energy. These changes in the magnetic domain structure are displayed in the hysteresis loop (Figs. 4.2, 6.2). The hysteresis loop is generated by measuring the magnetization (M) of a

material while the magnetizing force (H) is increased and decreased. The loop is the result of the varying applied field and the non-liner behaviour of ferromagnetic magnetization. Magnetic hysteresis parameters are obtained by first applying a positive magnetization until saturation of the grains is reached at which point the field is reversed to the negative direction until saturation is reached in that direction. Then a second experiment is run to determine the reverse field needed to reduce the remanence to zero after removal of the field. This direct current (D.C) demagnetization will give the coercivity of remanence, H_{cr} (Fig. 6.2b). The shape of the hysteresis loop is determined primarily by the mineralogy, grain size and grain shape.

In Figure 6.2 the saturation remanence, saturation magnetization, coercive force and remanent coercive force are shown for a SD grain. Figure 6.3 shows actual SD, PSD and MD examples of hysteresis loops for CY-4. The H_c is said to be meaningless in most cases where as the stability of remanence is considered important, since removal of the field will result in recovery of remanence which depends on the physical and geometrical state of the ferromagnetic assemblage (Wasilewski, 1973). Wasilewski (1973) states that the H_{cr} is of greater significance. For this reason H_c and H_{cr} were plotted separately (Fig. 6.5) against depth to compare their differences and importance.

The graph of the ratio of M_{rs}/M_s against H_{cr}/H_c, the Day plot, was first introduced by Day et al. (1977) and was later developed to differentiate grain size by Parry (1982) (Dunlop, 2002a, 2002b). A log-log Day plot was used to characterize the magnetic grain size down the CY-4 drill hole (Fig. 6.3). However, Wang and Van der Voo (2004) stated that while the Day plot does well at characterizing the grain size, it is less well suited to differentiate between iron oxides with higher and lower titanium content. Wang and Van der Voo (2004) eliminated H_{cr} in the Day plot and created a plot with the ratio M_{rs}/M_s, called 'squareness' (Tauxe et al., 2002), against H_c (Fig. 6.4). Dunlop (2002a) also believed the Day plot would determine grain size but that there must be independent information about the mineral compositions and state of internal stress as well. It is for this reason that mixing curves were introduced in order to compare the results from this study to known SD + MD and SP + SD mixtures (Fig. 6.7).

The Day plot is divided into SD, PSD and MD regions based on SD and "true" MD values of the parameters to define the limits of the PSD region (Dunlop, 2002a). Day et al. (1977) used $M_{rs}/M_s = 0.5$ and $H_{cr}/H_c = 1.5$ as SD limits and $M_{rs}/M_s = 0.05$ and $H_{cr}/H_c = 4$ as MD limits, for titanomagnetites of all compositions. These are generalizations since different values apply for titanomagnetites of different compositions and the MD limits maybe be subject to revision. Behaviour of PSD grains was explained by Stacey (1962), as an explanation of the

transitional magnetic properties of magnetite over the broad range between SD and truly MD (Dunlop, 2002a).

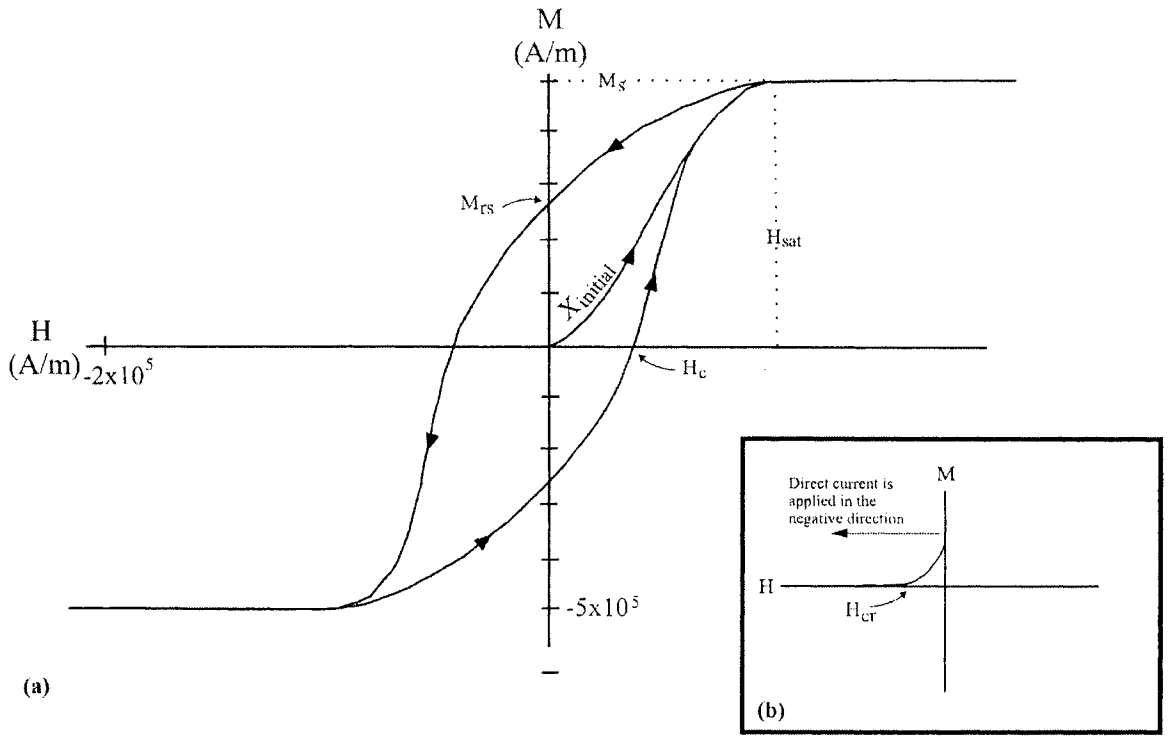

Figure 6.2. (a) Idealized hysteresis loop for randomly orientated SD magnetite grains. (Modified after (Dunlop and Özdemir, 1997) (b) Hypothetical example of DC demagnetization experiment that yields the H_{cr} value.

6.2 Methodology

There were 46 cores from CY-4 used for this rock magnetic method to characterize the magnetic grain size down the drill hole. An alternating gradient force magnetometer, a Princeton Measurements Micromag 2900 (1.4 T), was used for the hysteresis experiments. Four small chips, ranging from 1-3 mm in size (≤ 0.150g), from each core sample made a total of 184 measurements. Each chip was placed on the sample holder and held by viscous silicone vacuum grease. The maximum direct field (H) used in the experiments was 2.0 T. Since the hysteresis loop was used to determine the *ferromagnetic* mineralogy a slope-correction that turned the upper 70% of the high-field magnetization curve to horizontal, was used to illustrate the ferromagnetic response isolated from any paramagnetic background. This correction was done to eliminate any contributions from paramagnetic or diamagnetic minerals that may have been in the chip sample. The slope correction will result in an underestimation of the saturation magnetization for the

magnetically harder samples, if the high-field part is not truly saturated (Wang and Van der Voo, 2004).

The values for saturation remanence, saturation magnetization, coercive force and coercivity of remanence were plotted on Day and squareness plots then observed to determine the magnetic grain sizes down CY-4. This squareness plot helped to differentiate between TM_{60} and Ti-poor magnetite where as the Day plot characterized the magnetic grain size. Through grain size determination the Day plot successfully distinguished multidomain (MD) magnetite from smaller grained titanomagnetite (Moskowitz et al., 1998). It was concluded by Wang and Van der Voo (2004) that if titanomagnetite and magnetite have similar demagnetizing factors, the slope of squareness vs. H_c for titanomagnetites will be around four times higher than that of the Ti-free magnetite (Fig. 6.4). It appears in Figure 6.4 that all the specimens for CY-4 are really Ti-poor magnetites rather than TM_{60}, sensu stricto.

Hysteresis measurements used a small chip off a standard core specimen of 10.55 cm^3 in volume. This limits the accuracy of the results since just four small chips off of each core is used to represent the entire rock at each depth. At most the chip sample used in the Micromag represents ~0.04% of the core from which it was taken (Borradaile and Lagroix, 2000). Any heterogeneity within the core sample may lower this percentage. Thus, multiple runs of the sample cores were done and fortunately, reproducibly was rather good for the four runs (Fig. 6.6a). The results from hysteresis were used along with T_C and T_N to increase the precision of the magnetic mineralogy determined in this study. A complete list of data for each measured sample can be found in Appendix C.

6.3 Results

It is shown in a Day Plot (Fig. 6.3) that decreasing grain size results in an increase in M_{rs}/M_s and a decrease in $H_{cr}H_c$. For the sample set used in this study the majority fell within the PSD parameters. The more hydrothermally altered diabase dikes and gabbroic rocks fell within MD parameters whereas the lower gabbroic and ultramafic rocks fell along the SD-PSD boundary.

Figure 6.4. shows the squareness versus H_c plot for this study. The averages for each sample depth are used to simplify the diagram, giving 42 data points. Wang and Van der Voo's (2004) slopes were plotted on the graph to compare their known TM_{60} and magnetite slopes to the CY-4 lithology group slopes. The slope increased with depth indicating the increase in titanium within the magnetite grains which can also be correlated to a decrease in grain size. The ultramafic rocks plotted close to the TM_{60} but are still not steep enough to be labelled TM_{60}. The diabase dikes and all gabbroic rocks have slopes that correspond best with the Ti-poor magnetite.

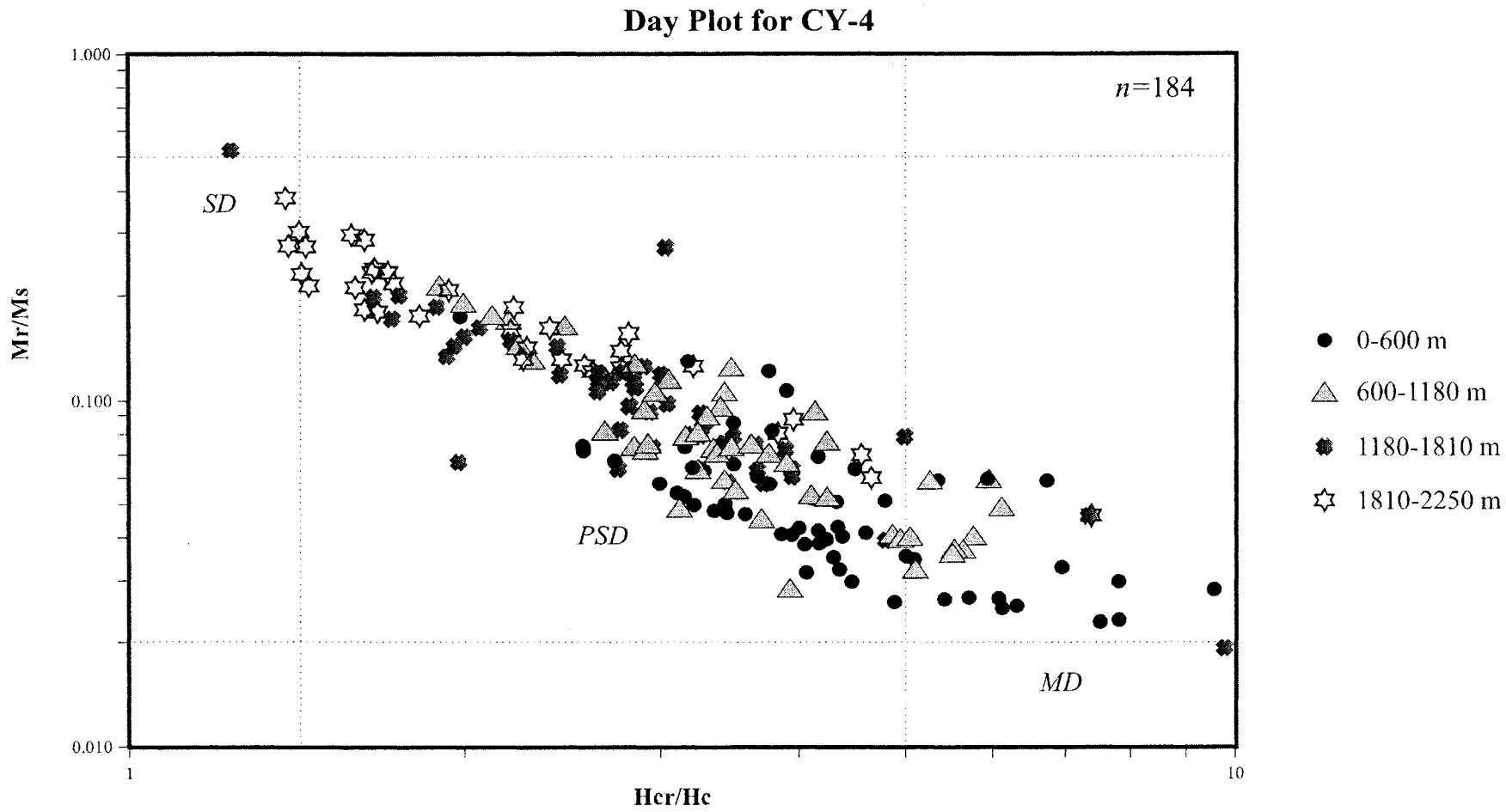

Figure 6.3. Day plot of the 186 hysteresis measurements taken from the CY-4 drill core. Symbols represent depth increments related to lithology. • is diabase dikes, △ is upper gabbroic rocks, **x** is lower gabbroic rocks and ★ is ultramafic rocks. As depth increases grain size decreases; M_{rs}/M_s increases and H_{cr}/H_c decreases.

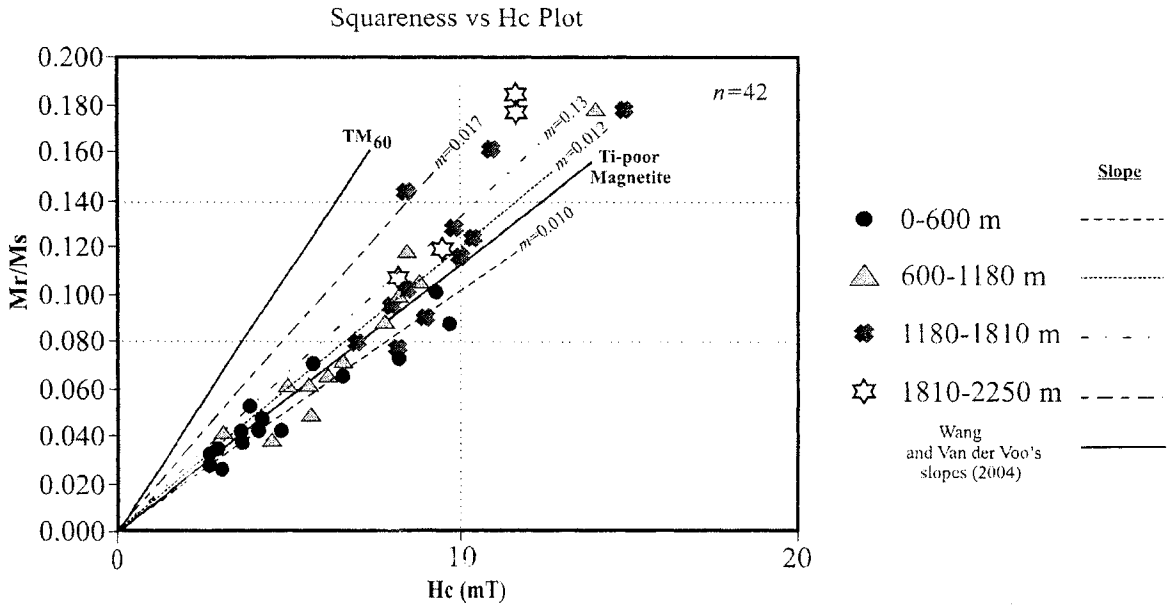

Figure 6.4. Squareness vs H_c plot for the CY-4 samples. The slope was calculated for each depth group separately. The slope increased with depth indicating an increase of titanium in the magnetite grains. *m*=slope of data points on graph for each lithology group.

The coercivity can also be referred to as magnetic hardness. The higher the coercivity the more magnetic hardness a material is said to have. Magnetic hardness (high coercivity) is generally associated with high Fe^{2+} concentration in titanomagnetites (Özdemir and O'Reilly, 1982). Figure 6.5a. displays the magnetic hardness down CY-4 and compares it to H_{cr} with depth (Fig. 6.5b) and the ratio of H_{cr}/H_c down CY-4. The H_{cr}/H_c versus depth (Fig. 6.5c) graph shows a steady decrease in H_{cr}/H_c with depth. The top of the drill hole indicates that the ferromagnetic minerals present have weaker magnetic memories than at the bottom of the hole. The minerals at the bottom of the hole have strong magnetic memories and are idea for palaeomagnetic methods even though they are most likely secondary TM_{60} or magnetite. The minerals at the bottom of the hole have weaker memories and are more likely representative of pure magnetite, probably with a tendency to acquire VRMs.

Figure 6.6a shows a data point for each measurement taken for this experiment. This illustrates the consistency of specimens and validates the sampling method (i.e., that four micro-samples do represent the rock specimen as a whole). Each run of 46 samples is shown on the Day plot by a different symbol. The four different runs are uniformly distributed the same, with only 2 outliers. The mean of each sample's 4 measurements was also calculated and the standard deviation is shown by the error bars (Figure 6.6b). The error bars are small with few exceptions. The small grain sizes (SD) show error bars equal for both the M_r/M_{rs} and H_{cr}/H_c ratios, but as you

move closer to the larger grain sizes (MD) the H_{cr}/H_c error bars become larger than the M_r/M_{rs} error bars.

Figure 6.7 displays three SD + MD mixing lines from Dunlop (200b). The mixing curve 1 shows a relationship best with the CY-4 data, at first glance, but a trendline will show that the data from the drill hole crosses these mixing lines indicating the presence of TM_{60}. The occurrence of TM_{60} in these rocks is known and therefore the mixing lines are not useful here.

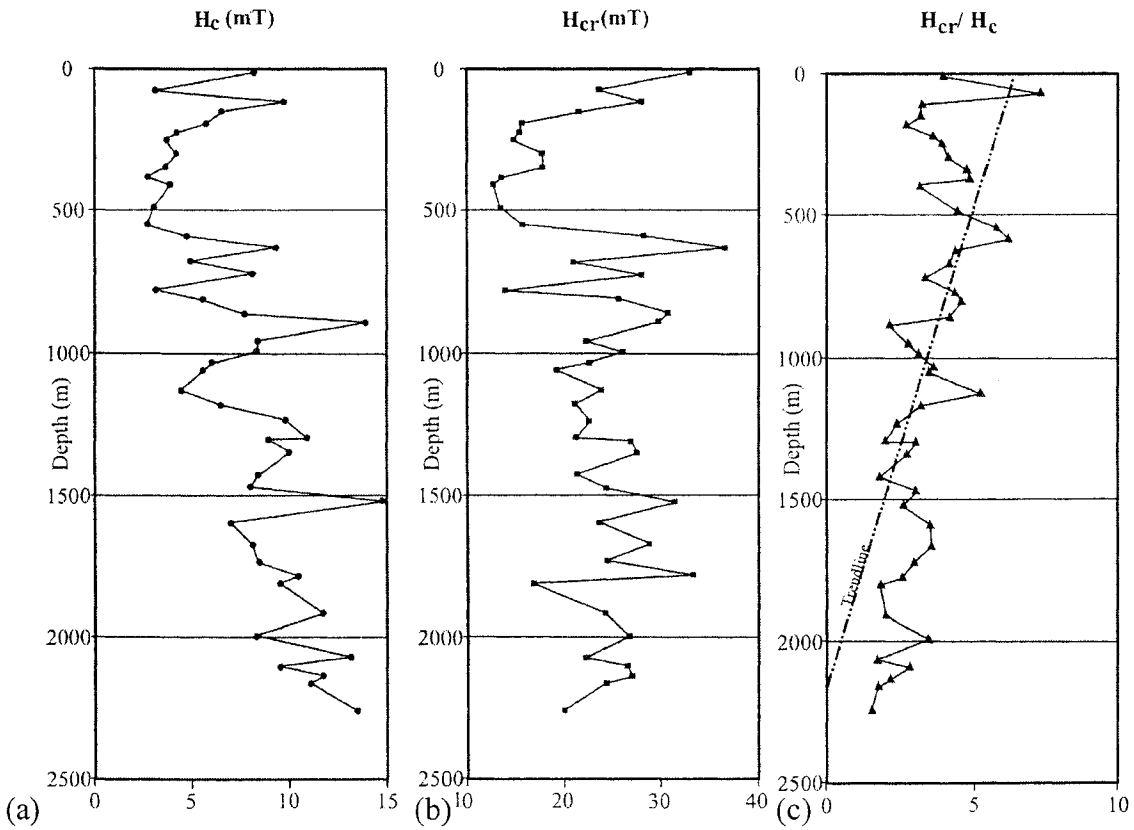

Figure 6.5. (a) Magnetic hardness (H_c) down CY-4. (b) H_{cr} versus depth. (c) H_{cr}/H_c down CY-4.

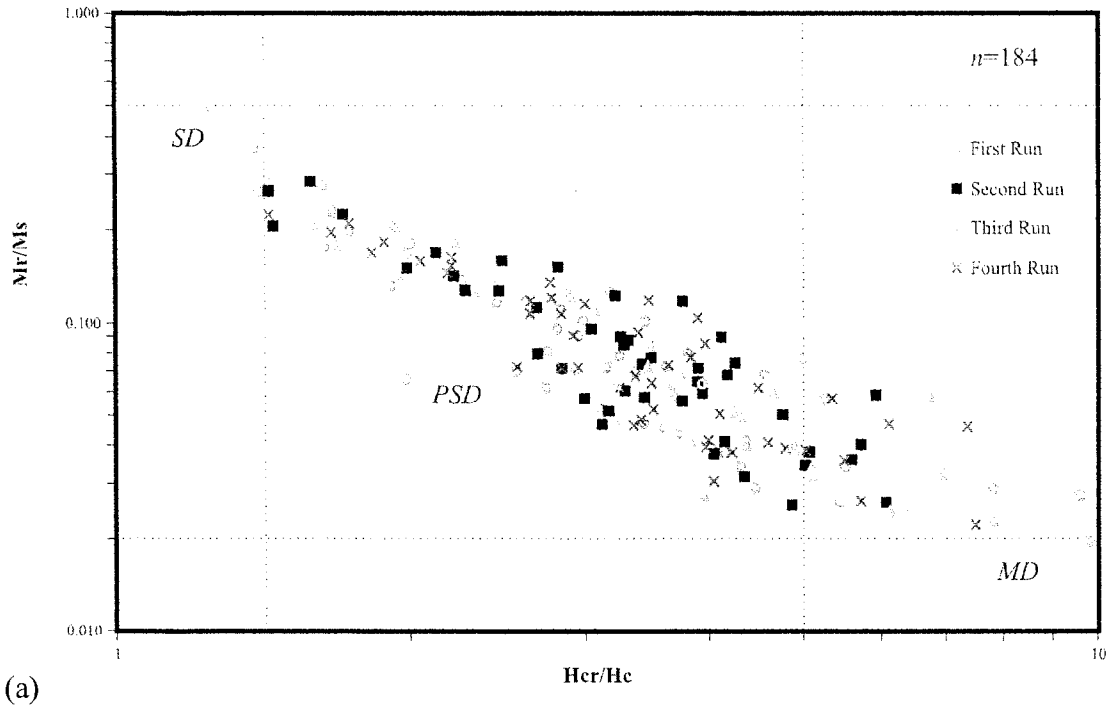

(a)

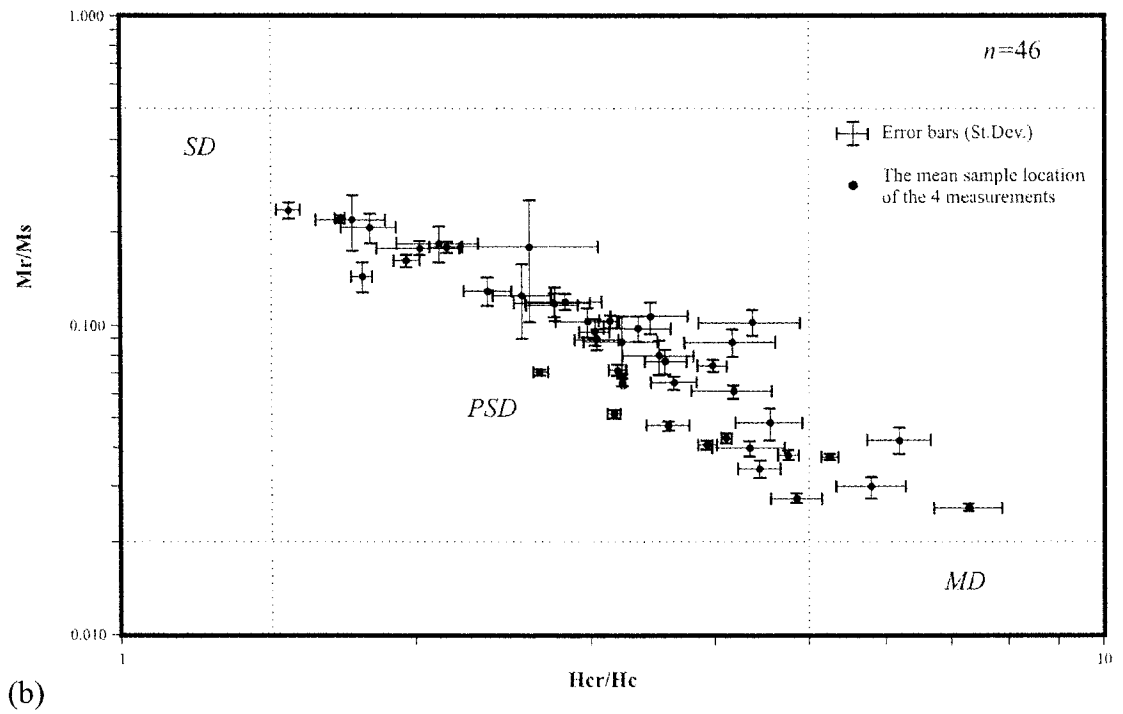

(b)

Figure 6.6. Day plots illustrating the consistency between the four different runs of the 46 samples used in this study. (a) Shows each run of samples separately. (b) The mean of the four runs for each sample is show with error bars.

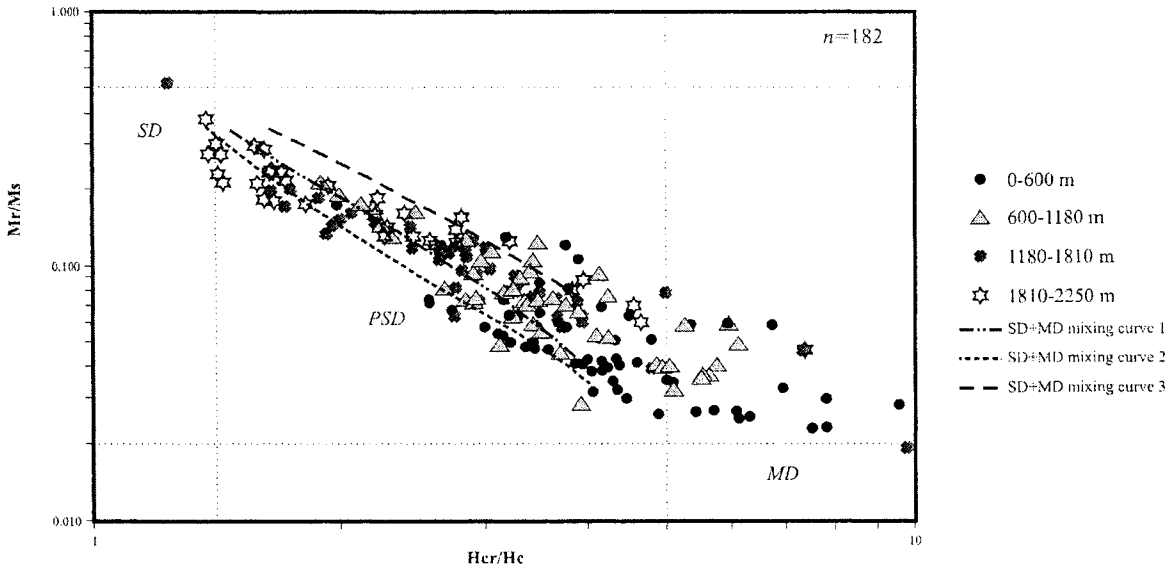

Figure 6.7. Mixing lines from Dunlop 2002b added to the results from CY-4. Mixing curve 1 correlates best with CY-4 samples.

Chapter 7. Palaeomagnetism

7.1 Introduction

Natural remanent magnetism (NRM) is fundamental to understanding palaeomagnetism and rock magnetism. NRM is a record of the Earth's magnetic field, as it existed at the time that a rock was formed. Analysis of NRM will indicate the intensity and direction of the permanent magnetism which in turn will determine a rocks age and history. In situ magnetization of rocks is the vector sum of two or more components: $J = J_i + J_r$ where J_i is the induced magnetization and J_r is the NRM (Butler, 1992). The geomagnetic field, H, produces the induced magnetization $J_i = \chi H$. Induced magnetization will generally parallel the local geomagnetic field and is usually the dominant component in a rock. However, palaeomagnetism is more concerned with the remanent magnetization since the acquisition of induced magnetization is a reversible process without any memory of past magnetic fields (Butler, 1992). Exponential decay of remanent magnetism occurs naturally and varies over many orders of magnitude. For instance, a SD grain that has a short relaxation time is referred to as superparamagnetic. Louis Néel showed that the characteristic relaxation time of SD magnetization is given by:

$$\tau = \frac{1}{C}\exp\left(\frac{\nu H_k j_s}{2kT}\right)$$

where C = frequency factor $\sim 10^{11}$, v = volume of SD grain, H_k = microscopic coercive force of SD grain, j_s = saturation magnetization of the ferromagnetic material and kT = thermal energy. Temperature dependence is strong for both the relaxation time and the coercive force. Butler (1992) shows that for coercive force controlled by shape anisotropy, H_c is proportional to j_s, whereas when controlled by magnetocrystalline anisotropy H_c is proportional to j_S^n, with $n > 3$. Blocking temperature, T_B, is the temperature at which the remanence acquired during cooling in a magnetic field becomes blocked within the rock (Tarling, 1983). It has an inversely proportional relationship to the relaxation time of the remanence at ambient temperature. The T_B of individual domain mainly depends on its size (~ domain state) and composition (Tarling, 1983). To interpret the geomagnetic field at different periods of time, the orientations of magnetization directions acquired by alternate palaeofields are isolated. Different demagnetization methods fix the orientations of the various components that make up the NRM. In this study low temperature demagnetization (LTD) and thermal demagnetization (TD) were used to isolate the component vectors of different age that combine to yield the NRM of the CY-4 rocks.

7.1.1 Natural Remanent Magnetism (NRM)

NRM is commonly composed of multiple magnetization vectors; a primary component and one or more secondary components. The way in which the NRM is acquired determines the type of remanent magnetism and its durability. Primary NRM is the magnetization representing the earth's geomagnetic field at the time of the rock's formation (or a 'short' time thereafter). The three most important forms of primary magnetization are thermoremanent magnetism (TRM), chemical remanent magnetism (CRM) and detrital remanent magnetism (DRM). Secondary NRMs are due to natural processes that affect a rock after its formation such as later geological events that produce other TRMs and CRMs. A ubiquitous secondary component is due to viscous remanent magnetism (VRM). Rarely, an isothermal remanent (IRM) will be formed by lighting.

TRM is the magnetism that is acquired when a rock cools from above its Curie temperature in the presence of a magnetic field (Butler, 1992). This is most common for igneous rocks. Butler (1992) explains that it is the action of the magnetic field at the T_B that produces a TRM. Any small magnetic field at elevated temperatures can impart a weak alignment in the distribution of magnetic moments of the ferromagnetic grains during cooling and produce a net remanent magnetization vector (Butler, 1992). All ferromagnetic grains behave paramagnetically above their T_C (Tarling, 1983). As different grain sizes cool just below the T_C, they will acquire different relaxation times while their H_c is low. The larger SD grains may have relaxation times that allow their remanence to be measured whereas smaller SD grains will have shorter relaxation times which may make them superparamagnetic (Tarling, 1983). When cooling to room temperature H_c increases rapidly and the larger SD grains will acquire relaxation times of the order of thousands to millions of years and could even exceed geological time. The smaller grains will show a range of relaxation times but some will be small enough continue to behave superparamagnetically. That is, they will have high susceptibility in an applied field and all remanence will be lost after removal of the field. Igneous rocks with stable TRM commonly have a T_B within approximately 100°C of the T_C (Butler, 1992) for the primary component of magnetization.

Total TRM is broken into portions that were acquired in distinct temperature intervals. The portion of TRM blocked in any particular T_B window is referred to as "parial TRM", PTRM (Butler, 1992). PTRM is a vector quantity, and TRM is the vector sum of the PTRMs contributed by all blocking temperature windows and can be expressed by Butler, (1992) as:

$$TRM = \sum_{n} PTRM(T_{Bn})$$

If magnetite is the dominant ferromagnetic mineral within a specimen, the vector sum of all PTRMs will be distributed from T_C to room temperature and thermal demagnetization experiments will systematically strip away components of magnetization and reveal each PTRM component. Thermal demagnetization is explained farther in section 7.1.3. This method is used in this study and reveals the important TRM components of the CY-4 rocks, as well as those acquired by chemical remanent magnetization described below.

CRM is acquired when magnetic grains nucleate and grow in a field (O'Reilly, 1974) for example during sea-floor metamorphism and hydrothermal alteration in the Troodos ophiolite. "Chemical change" i.e. mineralization, is responsible for forming new ferromagnetic minerals which takes place below their T_C. Tarling (1983) describes CRM as follows; i) After nucleation, it initially behaves superparamagnetic, then increases logarithmically in its relaxation time until it reaches a blocking volume (V_B) at which its remanence is stable enough to measure, (i.e., about 500 s); ii) Continued growth will result in a continued increase in the relaxation time until it reaches dimensions where MD behaviour commences and the relaxation time becomes less predictable but geologically significant. CRM may involve metamorphism of a ferromagnetic mineral or precipitation of a ferromagnetic mineral from solution. The oxidation and hydrothermal metamorphism common within the Troodos ophiolite make CRM an important component of the CY-4 rocks.

The form of magnetism that is acquired during deposition and lithification of sedimentary rocks is referred to as DRM (Butler, 1992). DRM is less understood than TRM and can be quite complex since there are so many processes involved in the formation of sedimentary rocks. In this study we are not concerned with DRM as a primary component.

Knowing the metamorphism, change in location with respect to the geomagnetic field and mineralogical changes that may have affected a rock will help to understand the secondary components. The gradual change of magnetization over time at a constant temperature is known as the viscous magnetization (Dunlop and Özdemir, 1997). This causes part of the initial NRM to be replaced by a VRM. In fact, VRM is merely a TRM with a very short relaxation time. Butler (1992) explains that from a palaeomagnetic viewpoint, VRM is usually undesirable noise. Rocks that are affected by periods of heating, such as metamorphism, will acquire a thermoviscous remanent magnetism (TVRM). The prolonged exposure to elevated temperatures below the T_C can alter the ferromagnetic minerals, even at low-grade metamorphism, sometimes destroying the primary NRM and/or chemically remagnetizing the rock (Butler, 1992), as in ophiolites. As long as there are ferromagnetic grains with high blocking temperatures, the primary NRM components can be retained. Low temperature demagnetization may remove the VRM and low blocking

temperature of TVRM components. This method of demagnetization is explained further in section 7.1.2.

7.1.2 Low Temperature Demagnetization (LTD)

LTD removes remanences of lower coercivity vector components, which are carried by the multidomain (MD) magnetite grains (0-15 mT) (Dunlop and Özdemir, 1997; Borradaile et al., 2004). It accomplishes this by rearranging unstable domain walls within magnetite grains. In order to do this the sample must be cooled below the Verwey transition (T_V), ~120 K and the isotropic point (T_k), around 135 K, since it is during these crystallographic changes that the domain walls can be destabilized and moved. Therefore, thermal cycling of samples that contain MD magnetite from room temperature to liquid nitrogen temperature (77 K) causes partial demagnetization of remanences. However, the remanence that is carried by the single domain SD grains is unaffected by LTD treatment (Muxworthy and McClelland, 2000). Therefore, LTD is useful in isolating the remanence carried by more stable magnetite grains in a sample since they are unaffected by any crystallographic changes which occur at low temperatures. Merrill (1970) found that multiple cycles of LTD are more effective than simply one longer duration at low temperatures and consequently, LTD is special in the way that it progressively and discretely rearranges domain walls.

7.1.3 Thermal Demagnetization (TD)

Butler (1992) explains that TD involves heating a specimen to elevated temperatures (T_{demag}) up to the ferromagnetic minerals T_Cs. After each incremental heating the specimen is cooled to room temperature in a zero magnetic field. The NRM components carried within grains, which have blocking temperatures (T_B) less than or equal to T_{demag} were randomized during heating. Re-measurement of the remaining remanence reveals what vector component of magnetization was lost. Repeated measurements are taken at room temperature in between each raise in temperature. This selective removal of NRM vector components permits one to identify stable vector directions and turning points between them.

Each NRM vector de-composition measured is shown graphically on a vector plot. The vector projections are viewed in two and three dimensions on a Zijderveld diagram. The power of the vector component diagram is its ability to display directional and intensity information on a single diagram by projection the vector onto two or three orthogonal planes (Butler, 1992). The Zijderveld diagram is used to observe a trajectory of the vector end points that trend towards the origin of a vector component diagram (Butler, 1992). An equal-area projection is also used; the

lower hemisphere stereonet will display the direction of the NRM vector components (Fig. 7.2). Principal component analysis (PCA) is then completed on the vector component diagrams to determine the best-fit line through the scatter of data. PCA's are then plotted and statistical analyses are done to establish the vectors mean orientations.

Sir Ronald Fisher (1953) was the first to derive a theoretical distribution, called the Fisher distribution, to look at three-dimensional statistical analyses of vectors on a sphere used in palaeomagnetic studies. Fisher recognized that the normal distribution of two-dimensional vectors on a sphere would show the orientations equal in all directions from the mean orientation and a cone that intersects the sphere as a small-circle out lining the confidence region (Borradaile, 2003). When direction is given unit weight, the small area on the sphere would have a probability density given by:

$$P = \frac{\kappa}{4\pi \sinh \kappa} \cdot \exp(\kappa \cdot \cos \delta)$$

where δ is the angular distance between a point and the true mean of the vector population and κ is the concentration parameter ranging from zero, if all vector points are uniformly distributed, to infinity if they are all parallel to the mean vector (Tarling, 1983).

The concentration parameter is:

$$\kappa \approx K = \frac{n-1}{n-R}$$

where n is the number of orientations sampled and R is the result of the calculated mean orientation. The calculated approximation for Fisher's κ is realistic for $n \geq 10$ and $\kappa \geq 3$ (Borradaile, 2003).

In palaeomagnetic studies the above statistical parameters are used. A probability of 0.05, expressed as α_{95} is most commonly used (Tarling, 1983). This means that there is a 95% confidence that the true mean direction will lie within the cone of radius α_{95} around the observed mean.

When the concentrations of data points are not in a circular distribution it is analysed using the Bingham model. In 1964 the Bingham statistical model was developed to explain populations that may vary from clusters being in a circular symmetry, to partial girdles to full girdles with axial symmetry on a sphere (Borradaile, 2003). A confidence cone with a Bingham distribution differs from the Fisher cone in that it will be elliptical. This is because the anisotropy of the orientation distribution distorts the confidence region about the mean orientation (Borradaile, 2003). The maximum Eigenvector (κ_{max}) gives the mean orientation of the Bingham distribution whereas the intermediate (κ_{int}) and minimum (κ_{min}) Eigenvectors determine the range

of the ellipse's radii out from the mean orientation. The long axis of the ellipse will then be drawn out along the intermediate concentration and the width of the ellipse will be in the direction of the minimum concentration. The Fisher mean is calculated as a vector mean whereas the Bingham mean is centred on the maximum Eigenvector (Borradaile, 2003). The Fisher and Bingham mean are shown in Figure 7.1.

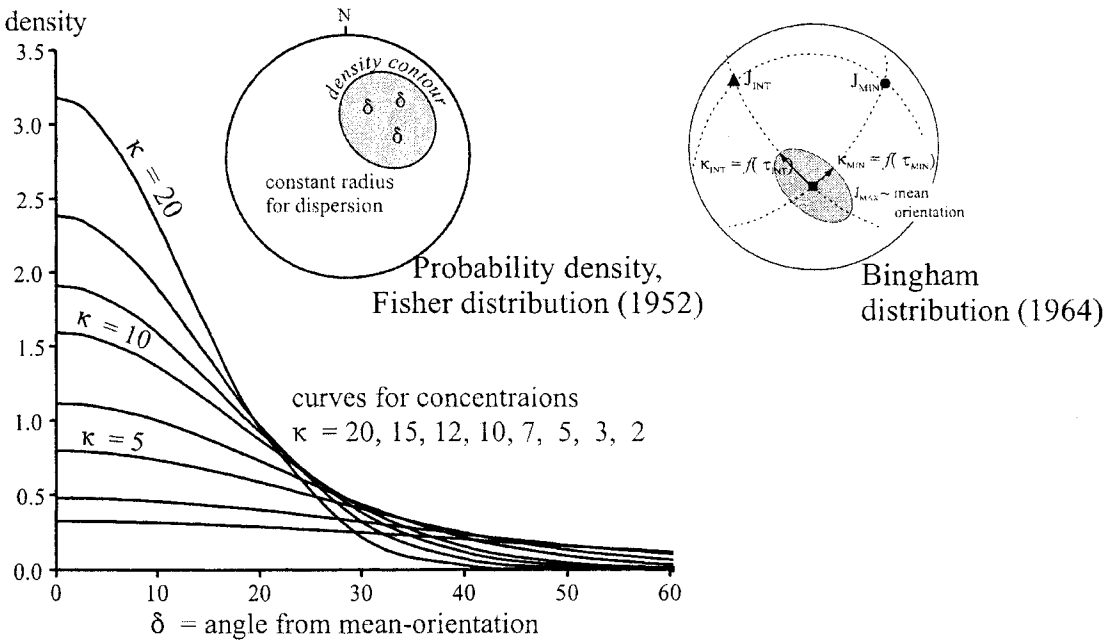

Figure 7.1. The probability density of the Fisher cone distribution for varying concentrations parameters of κ at different angles from the mean orientation is shown by the graph and on the first sphere. An example of a Bingham distribution from the concentration parameters of κ_{int} and κ_{min} on a sphere is given for comparison. (Modified after Borradaile, 2003)

7.1.4 Apparent Polar Wander Path (APWP)

A useful way to understand the importance of the CRMs isolated from NRM by demagnetization is to determine the location of the palaeopole, relative to the site (Troodos), responsible for magnetization. If the site moved, different CRM directions would define different palaeoples. These lie on an APWP which then show the inverse sense of motion of the site with respect to the palaeopole. The palaeomagnetic poles of varying geologic age taken from the NRM vectors are plotted on the present latitude-longitude grid and the path relative to the continent, in this case Cyprus (Borradaile and Lucas, 2002), is traced out to give the APWP for that tectonic region. Creer et al. first introduced the APWP method of summarizing palaeomagnetic results in 1954.

The Earth's magnetic poles and geographic poles are not exactly aligned. Geomagnetic secular variation varies the angular relationship of the axes over scales of 1 year to 10^5 years

(Butler, 1992). Secular variation patterns differ from continent to continent. Therefore, each APWP relates to a specific path taken by a continent over time but fortunately geological processes are sufficiently slow that the effects are averages out to define the geocentric axial dipole (GAD) model.

7.2 Methodology

First, the NRM was measured with the MOLSPIN magnetometer before incremental demagnetization was applied to each of the 46 samples down the CY-4 drill hole. After the original NRM was measured the samples were subjected to 3-cycles of LTD in liquid nitrogen. Each cycle consisted of immersing the samples in a liquid nitrogen bath (77K) and allowed to equilibrate at that temperature and then warm back up to room temperature in a magnetic shield, randomizing the domain boundaries and remanences that are less stale and undesirable in palaeomagnetism. Following LTD, thermal demagnetization was applied in 13 steps. Since magnetite dominates the remanent magnetism within the rocks of CY-4, TD was done to a maximum temperature of 550°C (580°C is the T_C for magnetite). The heating was completed in 13 steps. These were: 100°, 120°, 140°, 160°, 200°, 300°, 350°, 400°, 450°, 475°, 500°, 525° and 550°C, respectively. The heating was done in a TM-80 Shaw thermal demagnetizing furnace. Between each demagnetization step, the samples remaining remanence was measured using the MOLSPIN magnetometer and analyzed in the SPIN04.EXE program, written by Dr. G. Borradaile.

The vector components were sorted through in the SPIN04.EXE program. As explained in section 7.1.3, the linear trajectories of the vectors were portrayed on Zijderveld diagrams and in three-dimensional rotatable vector plots to determine the direction of the best-fit line for each component. PCA was carried out on each sample using selections from the 15 data points obtained by LTD and TD. In some cases one or two of these points were outliers, in which case they were deleted and the PCA was completed using the remaining points. After determining PCA's for the vectors, statistical analysis was completed to establish the vectors mean orientations. Vector components for each depth interval were plotted on an equal area stereonet showing the Fisher cone, Bingham 95% confidence cone, Eigenvectors, and density contour distribution. Figures 7.2 to 7.5 illustrate these stereonets and the statistical information used to determine the vector components. After analysing the statistical information, the mean of the Fisher cone or the maximum eigenvector was used for the palaeomagnetic pole and plotted onto a map to show the APWP. The first APWP for Troodos was determined by Borradaile and Lucas

(2003) and is shown in Figure 7.6 in order to compare the NRM vectors collected from the CY-4 drill hole.

7.3 Results

The vector components that were determined by PCA were divided into the four groups based on lithology and depth down the CY-4 drill hole; diabase dikes, upper gabbronorite, lower gabbronorite and ultramafic rocks. PCAs for each lithology were further separated into four components or unblocking temperature ranges that were identified by palaeomagnetic techniques. Two vector components, named A and D, were found within all lithology groups. Component A had a T_{ub} >550°C (Fig. 7.4) and component D had a T_{ub} <140°C (Fig. 7.5). Two other components were found in differing lithology groups. Component B was found between 350°C< T_{ub} <475°C and was found in the diabase dikes, lower and upper gabbronorite rocks (Fig. 7.2). Component C was found within the diabase dikes and upper gabbronorite rocks at 180°C< T_{ub} <200°C (Fig. 7.3). These two mid-temperature components were identified with very few samples (≤3) and therefore have questionable validity, according to the criteria of Van Der Voo (2004).

The A component of NRM was the most stable component isolated. It was still not completely unblocked at the highest temperature used in this study for TD (550°C). This component is the primary component of NRM. It is the oldest component and consequently, its relaxation time must exceed the age of the ophiolite. All A-vectors point downwards but in different directions for each lithology group.

The B and C components of NRM were identified in very few samples and therefore are just briefly mentioned here. They were not used to calculate palaeopoles since the numbers of samples were insufficient. Figures 7.2 and 7.3 show the stereonet diagrams for these components respectively. Most of these vectors point upwards.

The D component of NRM was the secondary component, almost certainly a VRM, which was easily removed below 140°C. All vector points of the D component point downwards and generally northward but in different direction for each lithology group.

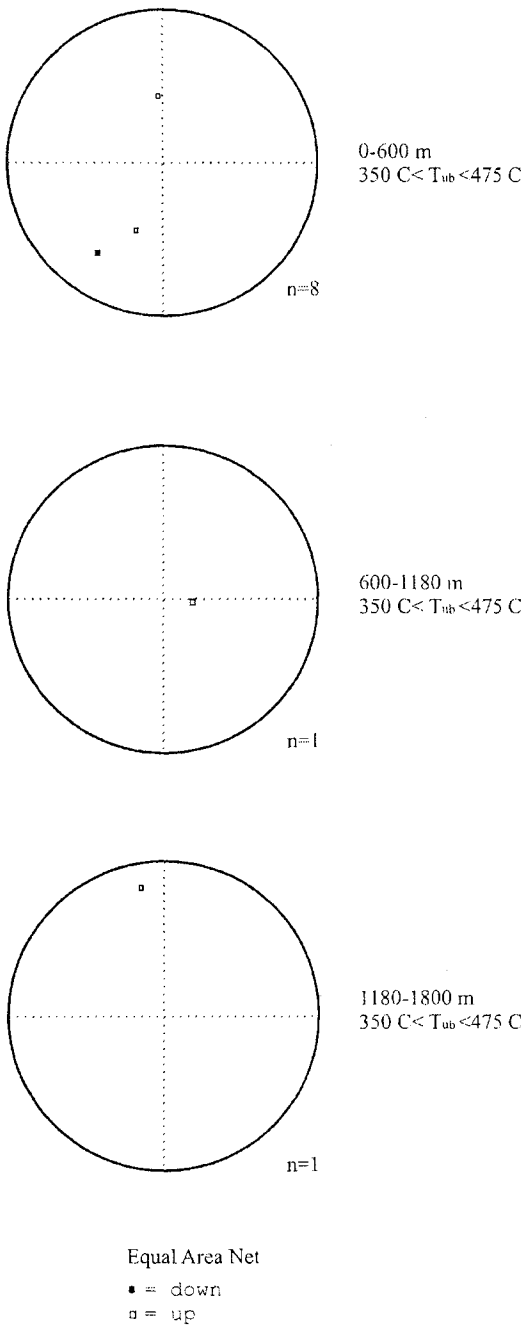

Figure 7.2. Stereonets showing the B component of NRM for the CY-4 drill hole. No statistics could be completed on these components since there are less then the required number of samples (i.e. >3) which fall within these T_{ub}'s.

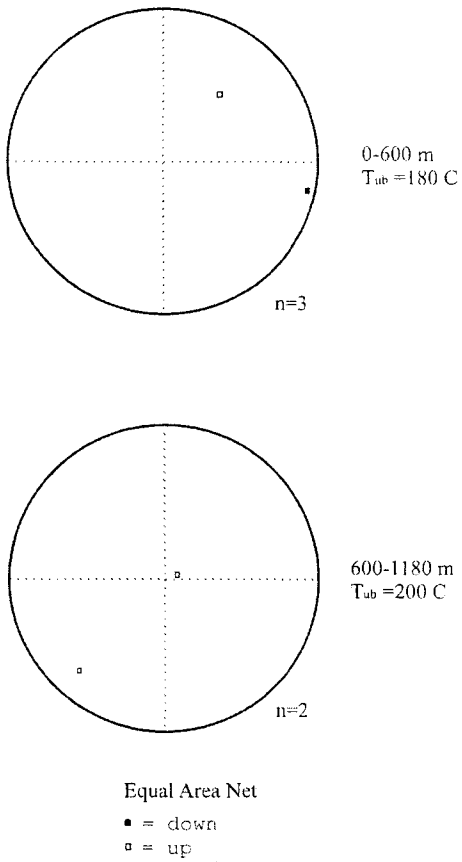

Figure 7.3. Stereonets showing the C component of NRM for the CY-4 drill hole. Statistics could not be completed on these components since there are less the required amount of samples within these T_{ub}'s.

Let us now expand on the two main components. Component A is defined by the following PCAs for each lithology group. The diabase dikes, defined by 13 samples, had an α_{95}=31.1 and the Bingham mean 234/78, which were used to calculate the palaeopole numbered 7 on the APWP (Fig. 7.6). There were 12 upper gabbronorite rock samples used to determine the Bingham mean 76/25, shown well by the density distribution and had an α_{95}=54.7. This palaeopole was number 8 on the APWP. The Fisher mean 320/22, also defined by the density distribution, and α_{95}=14.1 of the 11 samples in the lower gabbronorite rock lithology group were used to calculate palaeopole number 9 on the APWP. There were 8 samples used to determine the Bingham mean 360/34 and the α_{95}=27.8 for the ultramafic rocks which were palaeopole number 10 on the APWP. Figure 7.4 illustrates the statistics and density distributions that define component A.

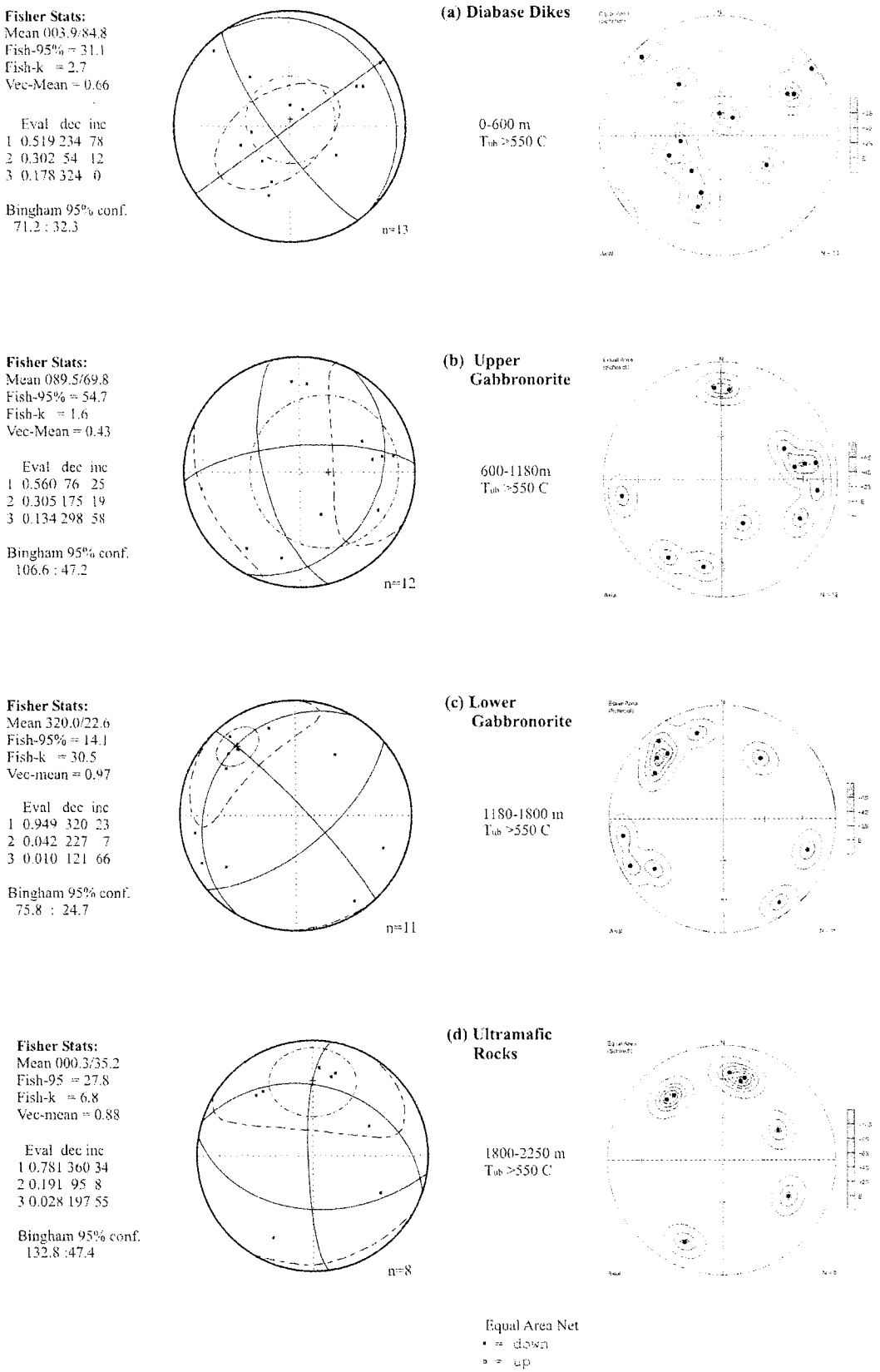

Figure 7.4. Stereonets showing the Fisher and Bingham statistics, as well as the density distribution (contours) for the A component of NRM for the CY-4 drill hole.

Component D is given by the following PCA's. The diabase dikes had a total of 26 samples to define the Fisher mean 147/78 and α_{95}=16.6. This was palaeopole number 1 on the APWP. Three populations for the upper gabbronorite rocks were distinguished on the contoured stereonet. Each population had its statistics calculated separately for the number of samples that fell within that area identified on the density distribution. These three populations were labelled a, b, and c on Figure 7.5. The Fisher mean 352/23 and α_{95}=5.5, determined by 4 samples, calculated palaeopole number 2 on the APWP. The Fisher mean 84/33 and α_{95}=10.4, defined by 10 samples, calculated pole number 3 on the APWP. Palaeopole number 4 was calculated using 10 samples that generated the Fisher mean 208/47 and α_{95}=25.7. Note that each of these three populations had the same Fisher mean as it did Bingham statistical mean, although it was written that the Fisher mean was used to calculate the palaeopoles. The lower gabbronorite unit was made up of 19 samples which determined the Bingham mean 308/33 and α_{95}=19.3. This palaeopole was numbered 5 on the APWP. The ultramafic rocks had 10 samples that defined the Fisher mean 356/45 and an α_{95}=25.8 and were used to calculate the palaeopole number 6 on the APWP. Figure 7.5 illustrates the statistics and density distributions that define component D.

The vector components defined by CY-4 rocks totalled the 10 palaeopoles just described. These 10 poles were plotted on the APWP in Figure 7.6. The ages labelled on the APWP were taken from the formation-mean vectors of Clube and Robertson (1986). The Palaeopoles at the high latitudes were distorted a small amount due to the map-projection. The following describes the results from the APWP. The A component for palaeopoles 8, 9 and 10 fell nicely along the APWP for the Troodos microplate. These three primary palaeopoles plotted according to age of cooling. The upper gabbronorites, 8, plotted as the oldest on the path, the lower gabbronorites, 9, cooled next at approximately 75 Ma and then the ultramafic rocks, 10, at about 55 Ma. The primary component for the dikes, 7, was far removed, over 30° away from the path. The inverse of the dike, 7**I** was also plotted to see if it would plot near the inverse Troodos wander path. However, it also plotted away from the inverse path.

The secondary, D component for the palaeopoles 2,3,4,5 and 6 fell along the APWP for Troodos. Poles 2-4 represented the three vector populations found within the upper gabbronorite unit. These also showed a trend related to age and cooling rates. Pole 3 was the oldest and fell directly on the path in same location as its primary pole, 8, for the upper gabbronorite group. However, 2 and 4 plotted as younger poles on the APWP. Palaeopole 2 fell close to the primary pole 10, for the ultramafic rocks, at 55 Ma whereas 4 plotted close to a bend (or cusp) on the path, not relating to any primary component. The lower gabbronorite group, 5, plotted within error to

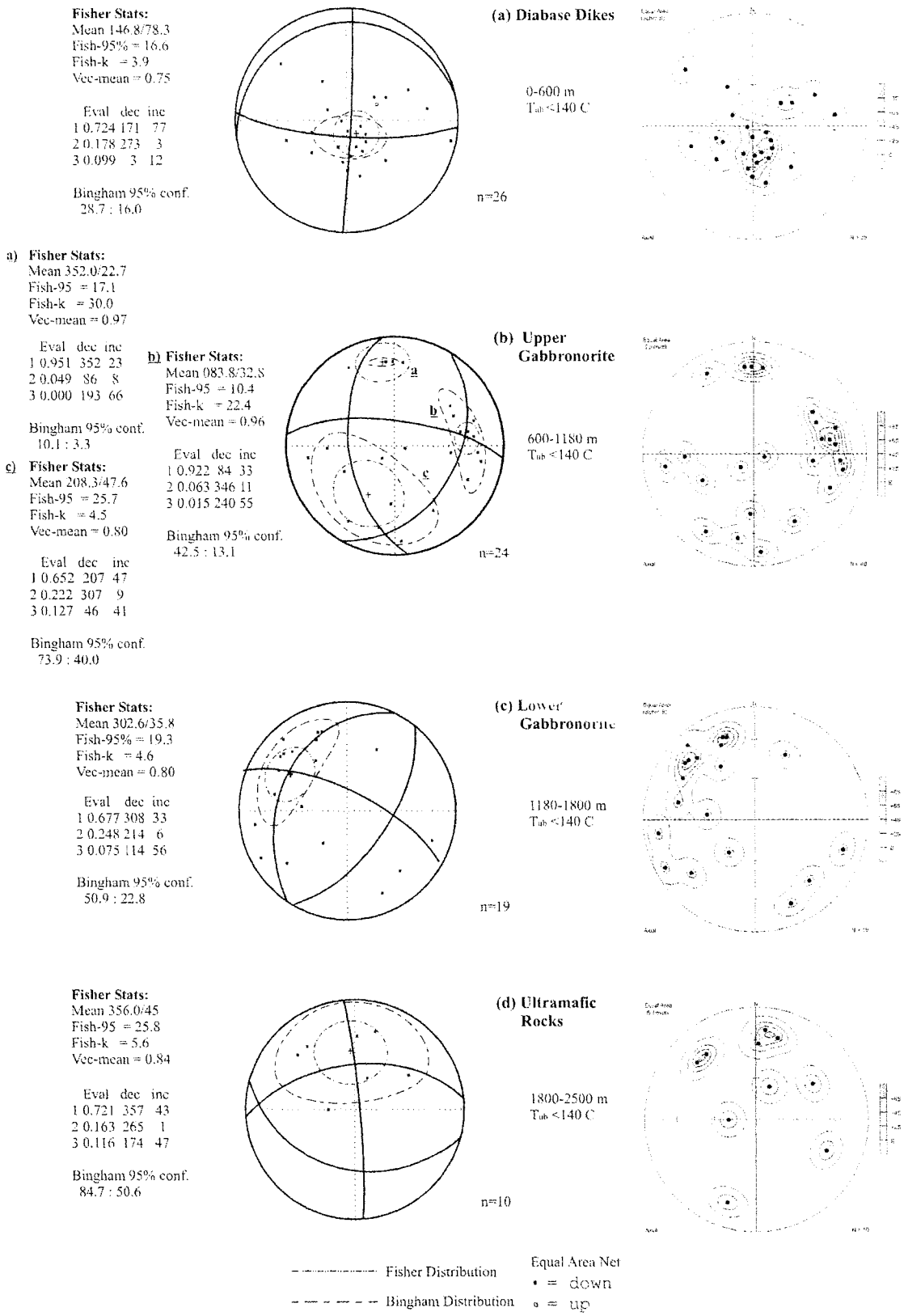

Figure 7.5. Stereonets illustrating the Fisher and Bingham statistics for the D component of NRM for the CY-4 drill hole. Contoured stereonets showing the concentration of the distribution are shown for each.

its primary component, 9, at 75 Ma. This D component for the ultramafic rocks, palaeopole 6, plotted on the path at 55 Ma next to pole 10, its primary component. The D component for the diabase dike group did not fall on the APWP, much like its primary component 7. It did however fall close to pole 7 on the map but again, over 30° away from the Troodos microplate path. The inverse 1I was plotted and once more, fell far from the inverse path for Troodos.

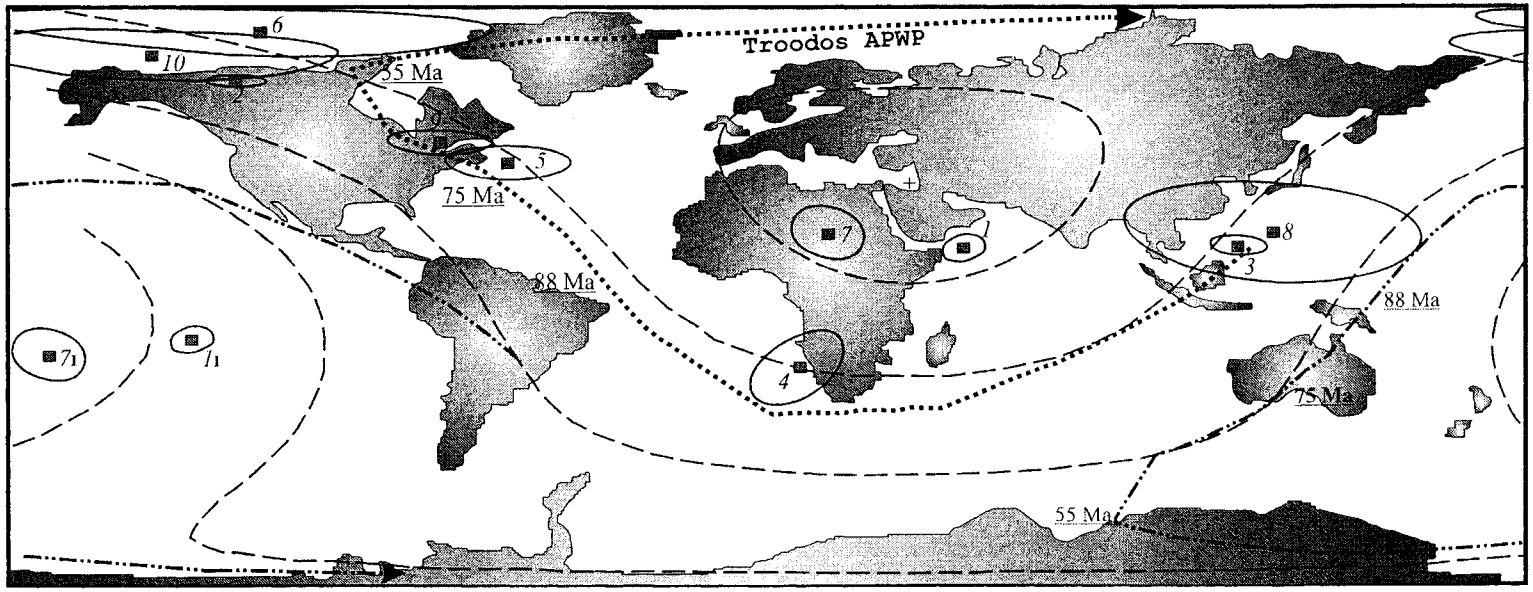

Troodos APWP
Inverse Troodos APWP
Co-latitude lines
\+ Cyprus (34°54', 33°05')
Components of NRM & 95% confidence cone
7I Inverse component of NRM

1 Component D- T ub<140 0-600 m, dikes
7 Component A- T ub>550 0-600 m, dikes

2 Component D- T ub<140 600-1180 m, upper gabbronorites
3 Component D- T ub<140 600-1180 m, upper gabbronorites
4 Component D- T ub<140 600-1180 m, upper gabbronorites
8 Component A- T ub>550 600-1180 m, upper gabbronorites

5 Component D- T ub<140 1180-1800 m, lower gabbronorites
9 Component A- T ub>550 1180-1800 m, lower gabbronorites

6 Component D- T ub<140 1800-2500 m, ultramafics
10 Component A- T ub>550 1800-2500 m, ultramafics

Figure 7.6. The apparent polar wander path for the Troodos ophiolite. The palaeopoles, shown by the square, represent the two main components of NRM found in this study.

Chapter 8. Conclusions

Magnetic properties vary systematically with distance from the spreading ridge and with depth due to the displacement of the spreading ocean crust relative to the ridge-parallel zone of hydrothermal metamorphism. Hydrothermal metamorphism extended to the depths of the gabbronorite in the case of the Troodos ophiolite; the underlying rocks were fresh. Alteration to a depth of approximately 1060 m was due to the hydrothermal metamorphism which principally oxidized the titanomagnetites, creating the rock magnetic variations through the stratigraphically higher lavas and diabase dikes studied here. Lower gabbros and ultramafic rocks were altered by serpentinization rather than by classical shallow hydrothermal ocean floor metamorphism.

Magnetite was common throughout the CY-4 rocks. This was shown by the Curie Balance and hysteresis experiments. The results from the Curie Balance experiments using the critical temperature points showed that hematite was also common throughout the entire CY-4 drill hole. Ti-rich magnetites were found to be present in both in 'fresh' and oxidized states within the diabase dikes and upper gabbro rocks to a depth of 1060 m. However, the original "sea-floor" TM_{60}'s were limited to the diabase dikes.

Hysteresis results show an obvious trend of decreasing ferromagnetic grain size with depth. However, the majority of samples fall within the PSD range. PSD behaviour is common in both magnetite and TM_{60}. The squareness (M_{rs}/M_s) versus H_c plot showed all specimens have slopes most similar to Ti-poor magnetite. Indicating that there is really no fresh TM_{60} present within the drill hole. The ferromagnetic minerals at the bottom of the drill hole had strong magnetic memories (H_{cr}/H_c), representing magnetite and oxidized TM_{60}, possibly secondary, whereas the top of the hole had minerals with weaker memories in which pure magnetite dominated.

The critical temperatures and hysteresis results indicate that TM_{60} or Ti-rich magnetite was a primary mineral in the diabase. TM_{60} was present in one ultramafic sample at the bottom of the CY-4, a likely survivor through serpentinization. Magnetite was found to be primary throughout the entire sequence and secondary in the serpentinized mantle rocks.

AMS and palaeomagnetic methods were used to understand the palaeomagnetic and metamorphic history of the Troodos ophiolite in the area of CY-4 drill hole. AMS results showed predominately oblate magnetic fabrics which were contributed by the large amounts of chlorite, magnetite, biotite and amphiboles present in the CY-4 rocks. AMS foliations and lineations were steep. The bulk susceptibility (κ) discriminated well between the four lithology zones. The diabase dikes had the highest κ and the gabbros had the lowest κ. Generally, the overall κ

decreased with from the top to the bottom of the drill hole, mainly due to the varying abundance of magnetite.

The AMS tensor means showed the overall magnetic fabric to be a strong L>S vertical fabric in the CY-4 drill hole with lineation and foliation both approximately vertical. The diabase dike group had such a similar resemblance to the overall magnetic fabric it was interpreted that the dikes had the largest influence on the CY-4 average AMS fabric. The mantle and upper gabbroic rocks showed a weak normalized fabric and a strong foliation fabric in the ferromagnetic minerals. This stronger magnetite subfabric was due to the periodic dikes that cut into the gabbros. The magnetic fabric became less anisotropic with depth, indicating less strain or plutonic flow to bottom mantle lithological groups. The lower gabbroic rocks showed a fabric parallel to the strike of the Mitsero graben in the normalized tensors and displayed a mantle flow fabric in the non-normalized results. The ultramafic rocks showed weak fabrics, consistent with a mantle flow magnetic fabric.

Palaeomagnetic experiments show two main vector components for the CY-4 rocks. The relative ages of cooling and alteration for the different lithology groups used in this study were evident in the palaeomagnetic record, except for the diabase dikes. The primary components of NRM for the upper gabbroic, lower gabbroic and ultramafic rocks all fell along the APWP with their respective secondary NRM components. Component A had a T_{ub} >550°C and component D had a T_{ub} <140°C. Component A was the stable and primary component of NRM within the CY-4 rocks. D was the secondary VRM component which was easily removed. Most palaeopoles for the diabase dikes were anomalous and ambiguous. They did not fall along the APWP for the Troodos microplate and no explanation can be uttered yet. However, as Dr. M. Jackson has suggested to us (personal communication, March 28 2006) this may be an artefact of palaeofield refraction by the steep dikes. The anomalously steep NRM of the dikes is related to their anisotropy which have steep magnetic lineations and could have been frozen in a biased record of the palaeomagnetic field. Three other lithology groups, lower and upper gabbros and ultramafic rocks, fell nicely along the APWP. Their palaeopoles showed the relative order in which these rocks acquired their magnetism and therefore the time they would have cooled or altered during microplate rotation. The upper gabbros plotted as the oldest rocks and consequently the first to cool. The lower gabbros cooled next at about 75 Ma. The ultramafic rocks acquired their characteristic component of NRM at 55 Ma, at the end of microplate rotation.

As Kusznir (1980) has shown, intrusive rocks have a greater magnetization than the plutonic or mantle rocks; this is true for the CY-4 rocks used in this study. Hydrothermal alteration occurred in a cell which affected the four 'stratigraphic' layers defined in this study,

differently. Since the Troodos ophiolite had an intermediate spreading rate of approximately 50-150 mm/year, a large volume of intrusive rocks was remagnetized strongly and deeper into the oceanic crust. Gills and Roberts (1999) placed the depth to which hydrothermal alteration took place in the Troodos ophiolite at the boundary between the dikes and upper gabbros. The curie temperatures verify this statement since it is at this depth, about 1060 m, that the evidence for TM_{60} (oxidized and original) disappears below which magnetite due to primary causes or serpentinization is found.

Alteration of the NRM of the Troodos rocks varied largely with time so that each stratigraphic/lithology group acquired NRM differently. The range in temperatures in the hydrothermal cell also varied largely with depth and pressure on the fluids and fracture-permeability. These factors all influenced the palaeomagnetic results observed in this study. During microplate rotation different rocks were magnetized at different stages. The upper gabbros cooled and acquired their magnetizations before the rotation of the Troodos microplate. The lower gabbros were affected by the first anticlockwise microplate rotation of around 60° whereas the ultramafic rocks were magnetized during the final rotation of approximately 30°.

References

Aktas, G. and Robertson, A.H.F., 1984. The Maden Complex, SE Turkey: evolution of a Neotethyan continental margin. In: Dixon, J.E., Robertson, A.H.F (Eds.), The Geological Evolution of the Eastern Mediterranean. Special Publication-Geological Society of London, vol. **17**, 375-402.

Bear, L., 1960. The geology and mineral resources of the Akaki-Lythrodondha area. Geolocial Survey Department, Cyprus, Memoir 3.

Ben-Avraham, Z., Shoham, Y., and Ginsburg, A., 1976. Magnetic anomalies in the Eastern Mediterranean and the tectonic setting of the Eratosthenes Seamount. Geophysical Journal of the Royal Astronomical Society, vol. **45**, 313-331.

Ben, K., and Allard, B., 1988. Preferred mineral orientations related to magnetic flow in ophiolite layered Gabbros. Journal of Petrology, **30**, 925-946.

Ben-Avraham, Z., Tibor, G., Limonov, A.F., Leybov, M.B., Ivanov, M.K., Tokarev, M.Yu., and Woodside, J.M., 1995. Structure and tectonics of the Eastern Cyprean arc. Marine and Petroleum Geology, vol.**12**, 263-271.

Borradaile, G.J., 1988. Magnetic susceptibility, petrofabrics and strain. Tectonophysics, **156**, 1-20.

Borradaile, G.J., 1991. Correlation of strain with anisotropy of magnetic susceptibility (AMS). Pure and Applied Geophysics, **135**, 15-29.

Borradaile, G.J., 1994. Paleomagnetism carried by crystal inclusions: the effect of preferred crystallographic orientations. Earth and Planetary Science Letters, **126**, 171-182.

Borradaile, G.J., 2001. Magnetic fabrics and petrofabrics: their orientation distributions and anisotropies. Journal of Structural Geology, **23**,1581-1596.

Borradaile, G.J., 2003. *Statistics of Earth Science Data. Their Distribution in Time, Space and Orientation.* Springer-Verlag, Burlin, Berlin.

Borradaile, G.J., and Dehls, J.F., 1993. Regional Kinematics inferred from magnetic subfabrics in Archean rocks of Northern Ontario. Canadian Journal of Structural Geology, **15**, 887-894.

Borradaile, G.J. and Gauthier, D., 2001. AMS-detection of inverse fabrics without AARM, in ophiolite dikes. Geophysical Research Letters, **28**, no. 18, 3517-3520.

Borradaile, G.J. and Gauthier, D., 2003. Interpreting anomalous magnetic fabrics in ophiolite dikes. Journal of Structural Geology, **25**, 171-182.

Borradaile, G.J., and Henry, B., 1997. Tectonic applications of magnetic susceptibility and its anisotropy. Earth-Science Reviews, **42**, 49-93.

Borradaile, G.J., and Jackson, M. J., 1993, Changes in magnetic remanence during simulated deep sedimentary burial: Physics of the Earth and Planetary Interiors, vol. **77**, p. 315–327.

Borradaile, G.J., and Jackson, M., 2004. Anisotropy of magnetic susceptibility (AMS): magnetic petrofabrics of deformed rocks from *Magnetic Fabric: Methods and Applications.* Geological Society, London, Special Publications, **238,** 299-360.

Borradaile, G.J and Kukkee, K., 1996. Rock-magnetic study of gold mineralization near a weakly deformed Archean syenite, Thunder Bay, Canada. Exploration Geophysics **27**, 25-31.

Borradaile, G.J., and Lagroix, F., 2000. Thermal enhancement of magnetic fabrics in high grade gneisses. Geophysical Research Letters, **27**, 2413-2416.

Borradaile, G.J., and Lagroix, F., 2001. Magnetic fabrics reveal Upper Mantle flow fabrics in the Troodos Ophiolite Complex, Cyprus. Journal of Structural Geology, **23**, 1299-1317.

Borradaile, G.J., and Lucas, K., 2003. Tectonics of Akamas and Mamonia ophiolites, Western Cyrus: magnetic petrofabrics and Paleomagnetism. Journal of Structural Geology, **25**, 2053-2076.

Borradaile, G.J., and Stupavsky, M., 1995. Anisotropy of magnetic susceptibility: Measurement schemes. Geophysical Research Letters, vol.**22**, 1957-1960.

Borradaile, G.J., Keeler, W., Alford, C., and Sarvas, P., 1987. Anisotropy of magnetic susceptibility of some metamorphic minerals. Physics of the Earth and Planetary Interiors, **48**, 161-166.

Borradaile, G. J. Stewart, R.A. & Werner, T. 1994. Archean uplift of a subprovince boundary in the Canadian Shield revealed by magnetic fabrics. Tectonophysics, **227**, 1-15.

Borradaile, G.J., Lucas, K. and Middleton, R.S, 2004. Low-temperature demagnetization isolates stable magnetic vector components in magnetite-bearing diabase, *Geophysics J. Int.,* **157**, 526-536.

Bown, J.W., White, R.S., 1994. Variations with spreading
rates of oceanic crustal thickness and geochemistry. Earth Planet Sci. Lett. **121**, 435-449.

Butler, R.F., 1992. *Paleomagnetism: Magnetic Domains to Geologic Terranes,* Blackwell Scientific Publications, United States of America, p.319.

Calvert, A., 1995. Seismic evidence for a magma chamber beneath the slow-spreading Mid-Atlantic Ridge. Nature, **377**, 410-414.

Cann J., Oakley, R.J., Richards, H.G., and Richardson, C.J., 1987. Geochemistry of hydrothermally altered rocks from Cyprus Drill Holes Cy-2 and Cy-2a compared with other Cyprus stockworks. Geological Survey Department, No. **2**, 79.

Cannat, M., 1993. Emplacement of mantle rocks in the seafloor at mid-ocean ridges. J. Geophysics Res. **98**, 4163-4172.

Cannat, M., Mevel, C., Maia, M., Deplus, C., Durand, C., Gente, P., Agrinier, P., Belarouchi, A. and Dubuisson, G., 1995. Thin crust, ultramafic exposures and rugged faulting patterns at the Mid-Atlantic Ridge. Geology **23**, 49-52.

Chen, Y.J., 1992. Oceanic crustal thickness versus spreading rate. Geophysics Res.Lett. **19**, 753-756.

Clube, T., Creer, K. and Robertson, A.H., 1985. Paleorotation of the Troodos microplate, Cyprus. Nature (London), **317**, 522-525.

Clube, T. and Robertson, A.H., 1986. The paleorotation of the Troodos microplate, Cyprus, in the Late Mesozoic-Early Cenozoic plate tectonic framework of the Eastern Mediterranean. Sureys in Geophysics, **8**, 375-437.

Constantinou, G., 1980. Metallogenesis associated with the Troodos ophiolite. In: Panayiotou, A., (Ed.), Ophiolites: Proceedings of the International Ophiolite Symposium, Cyprus 1979: Cyprus Geological Survey Department, 663-673.

Day, R., Fuller, M. and Schmidt, V.A., 1977. Hysteresis properties of titanomagnetites: Grain size and composition dependence. Phys. Earth Planetary Interiers, **13**, 260-267.

Delaloye, M. and Wagner, J.J., 1984. Ophiolites and volcanic activity near the western edge of the Arabian plate. In: Dixon, J.E., Robertson, A.H.F. (Eds.), The Geological Evolution of the Eastern Mediterranean. Special Publication-Geological Society of London, vol. **17**, 225-233.

Dilek, Y., Thy, P., Moores, E.M. and Ramsden, T.W., 1990. Tectonic evolution of the Troodos ophioloite within the Tethyan framework: Tectonics, **9**, 811-823.

Dunlop, D.J., 2002a. Theory and application of the Day plot (M_{rs}/M_s versus H_{cr}/H_c) 1.Theoretical curves and tests using titanomagnetite data. J.Geophys. Res., **107**, 4-1 – 4-22.

Dunlop, D.J., 2002b. Theory and application of the Day plot (M_{rs}/M_s versus H_{cr}/H_c) 2.Application to data for rocks, sediments, and soils. J. Geophys. Res., **107**, 5-1 – 5-15.

Dunlop, D.J., and Özdemir, O., 1997. *Rock Magnetism: Fundamentals and Frontiers, Cambridge Studies in Magnetism*, Cambridge University Press, Cambridge, 573 pp.

Elthon, D., and Stern, C.R., 1978. Metamorphic petrology of the Sarmiento ophiolite complex, Chile. Geology , vol.**6**, 464-468.

Escartun, J., Lin, J., 1995. Ridge offsets, normal faulting and gravity anomalies of slow spreading ridges. J. Geophysics Res. **100**, 6163-6177.

Ferré, E.C., 2002. Theoretical models of intermediate and inverse AMS fabrics. Geophysical Research Letters, vol. **29**, no. 7.

Fisher, R.A., 1953. Dispersion on a sphere. Proc. Roy. Soc., A217, 295-305.

Flinn, D., 1965. On the Symmetry Principal and the Deformation Ellipsoid. Geol. Mag. vol.**102**. No.1.

Garfunkel, Z., 2004. Origin of the Eastern Mediterranean basin: a reevaluation. Tectonophysics **391**, 11-34.

Gauthier, D., 2002. Magnetic Fabrics from Sheeted Dikes Reveal Regional Magma Flow Patterns and the Spacing and Dimensions of Ophiolite Magma-Chambers, Troodos Ophiolite, Cyprus. Unpublished M.Sc. Thesis, Lakehead University, 229pp.

Gass, I., 1968. Is the Troodos Massif of Cyprus a fragment of Mesozoic ocean floor? Nature, **220**, 39-42.

Gass, I. and Smewing, J., (1973). Intrusion, extrusion and metamorphism at constructive margins: evidence from the Troodos Massif, Cyprus. Nature, **220**, 39-42.

Gee, J. and Kent, D.V., 1999. Calibration of magnetic granulometric trends in oceanic basalts. Earth and Planetary Science Letters **170**, 377-390.

Gills, K.M., and Robinson, P.T., 1988. Distribution of alteration zones in the upper oceanic crust. Geology, vol.**16**, 262-266.

Gills, K.M., and Roberts, M.D., 1999. Cracking at the magma-hydrothermal transition: evidence from the Troodos Ophiolite, Cyprus. Earth and Planetary Science Letters **169**, 227-244.

Hall, J.M., Fisher, B., Walls, C., Ward, T., Hall, L., Johnson, H.P. and Pariso, J., 1989. The physical properties of diabase, gabbros and ultramafic rocks from CCSP drill hole CY-4 at Palekori, Cyprus. *In:*

Cyprus Crustal Study Project: Initial Report, Hole CY-4; Energy, Mines and Resources Canada, Paper 88-9, p. 235-278.

Hargraves, R.B., Johnson, D., and Chan, C.Y., 1991. Distribution anisotropy: the cause of AMS in igneous rocks? Geophysical Research Letters, vol. **18**, 2193-2196.

Haymon, R.M., 1996. Hydrothermal System Response to Ridge Segmentation. Tectonic, Magmatic, Hydrothermal and Biological Segmentation of Mid-Ocean Ridges, Geological Society Special Publication No. **118**, 157-168.

Henry, B., 1983. Interpretation quantitative de l'anisotropie de susceptibilitie magnetique. Tectonophysics, **91**, 165-177.

Hirt, A.M., Lowrie, W., Clendenen, W.S., and Kligfield, R., 1988. The correlation of magnetic anisotropy with strain in the Chelmsford Formation of the Sudbury Bason, Ontario. Tectonophysics, **145**, 177-189.

Hirt, A.M., Lowrie, W., Clendenen, W.S., and Kligfield, R., 1988. Correlation of strain and the anisotropy of magnetic susceptibility in the Onaping Formation: evidence for a near-circular origin of the Sudbury basin. Tectonophysics, **225**, 231-254.

Hrouda, F., 1982. Magnetic anisotropy of rocks and its application in geology and geophysics: Geophysical Surveys, vol.**5**, 37-82.

Hrouda. F., 1986. The effect of quartz on the magnetic anisotropy of quartzite. Studia Geophys. Geod. **30**, 39-45.

Hrouda, F., 2002. The use of the anisotropy of magnetic remanence in the resolution of the anisotropy of magnetic susceptibility into its ferromagnetic and paramagnetic components. Tectonophysics, **347**, 269-281.

Hrouda. F., Jelinek, V. and Zapletal, K., 1985. Use of magnetic properties of rocks in ore and petroleum geophysics (in czech). Res. Rep. Geofyz. Brno, 54-75.

Hunt, C.P., Moskowitz, B.M., and Banerjee, S.K., 1995. Magnetic properties of rocks and minerals. In Rock Physics and Phase Relations. AGU Reference Shelf, **3**:189-204

King, J.G., and Williams, W., 2000. Low temperature magnetic properties of magnetite. Journal of geophysics research, vol.**105**, 16427-16436

Klein, E. M., Langmuir, C. H., 1987. Global correlations of ocean ridge basalt chemistry with axial depth and crustal thickness. J. Geophysics Res.**92**, 8089-8115.

Kosterov, A., 2001. Magnetic hysteresis of pseudo-single-domain and multidomain magnetite below the Verwey transition. Earth and Planetary Science Letters **186**, 245-253.

Kusznir, N.J., 1980. Thermal evolution of the oceanic crust; its dependence on spreading rate and effect on crustal structure. Geophys. J.R.astr.Soc. **61**, 167-181.

Jelinek, V., 1981. Characterization of the magnetic fabric of rocks. Tectonophysics, **79**, 63-67.

Jelinek, V., 1978. Statistical processing of anisotropy of magnetic susceptibility measured on groups of specimens. Studia Geophysica. et Geodetica., **22**: 50-62.

Lagroix, F., and Borradaile, G.J., 2000. Magnetic fabric interpretation complicated by inclusions in mafic silicates. Tectonophysics, **325**, 207-255.

Landau L. and Lifshitz, E., 1953. On the Theory of the Dispersion of Magnetic Permeability in Ferromagnetic Bodies. Physik Z. Sowjetunion, vol. **8**, 153.

Lienert, B.R., 1991. Monte Carlo simulation of errors in the anisotropy of magmatic susceptibility: a second –rank symmetric tensor. Journal of Geophysical Research, **96**, 19539-19544.

Lin, J. and Phipps Morgan, J., 1992. The spreading rate dependence of three-dimensional mid-ocean ridge gravity structure. Geophysics Res.Lett. **19**, 13-16.

Livermore, R.A. and Smith, A.G, 1984. Some boundary conditions for the evolution of the Mediterranean region. In: Stanley, D.J., Wezel, F.-C. (Eds.), Geological Evolution of the Mediterranean Basin. Sringer-Verlag, 83-100.

Lowell, R.P., and Rona, P.A., 2002. Seafloor hydrothermal systems driven by the serpentinization of peridotite. Geophysics Res.Lett. **29**, no.11, 1-.4.

Kempler, D., 1994. *Tectonic patterns in the Eastern Mediterranean.* Unpublished PhD thesis, Hebrew University of Jerusalem.

Kempler, D., 1998. Eratosthenes Seamount: the possible spearhead of incipient continental collision in the Easternmost Mediterranean. In Robertson, A.H.F., Emeis, K.C., Richter, C, and Camerlenghi, A., eds., Proceedings ODP, Scientific Results, vol. **160**, 709-722.

Lauer, J.P., 1981. *L'evolution geodynamique de la Turquie et de la Chypre deduite de l'etude paleomagnetique.* Unpubl. Doctorat-Es-Sciences these, University of Strasbourg, France, 292.

Malpas, J., Brace, T. and Dunsworth, S.M., 1989a. Structural and petrologic relationships of the CY-4 drill hole of the CCSP. *In:* Cyprus Crustal Study Project: Initial Report, Hole CY-4; Energy, Mines and Resources Canada, Paper 88-9, p. 39-68.

Malpas, J., Case, G. and Moore, P., 1989b. The geology of the area immediately surrounding the CY-4 borehole of the CCSP. *In:* Cyprus Crustal Study Project: Initial Report, Hole CY-4; Energy, Mines and Resources Canada, Paper 88-9, p. 31-38.

Malpas, J., Robinson, P.T. and Salisbury, M., 1989c. Geology and geophysics of borehole CY-4 of the CCSP: Summary. *In:* Cyprus Crustal Study Project: Initial Report, Hole CY-4; Energy, Mines and Resources Canada, Paper 88-9, p. 381-393.

Malpas, J., Calon, T. and Squires, G., 1993. The development of late Cretaceous microplate suture zone in SW Cyprus. *In:* Prichard, H. (ed.), Magmatic processes and plate tectonics, Geological Society, Special Publications **76**, 117-195.

Mart, Y. and Robertson, 1998. Eratosthenes Seamount: an oceaniographic yardstick recording the Late Mesozoic-Tertiary geological history of the Eastern Mediterranean. In: Robertson, A.H.F., Emeis, K.C., Richter, C., Camerlenghi, A. (Eds.), Proceddings of the ODP. Scientific results, Vol. **160**, 701-708.

McCulloch, M.T. and Cameron, W.E. 1983. Nd-Sr isotopic study of primitive lavas from the Troodos ophiolite, Cyprus: evidence for a subduction-related setting. Geology, **11**: 727-731.

McElhinny, M. W., and P. L. McFadden, 2000. *Paleomagnetism: Continents and Oceans*, Academic Press, San Diego, California, 386 pp.

McKenzie, D.P., 1972. Active Tectonics of the Mediterranean region: Royal Astronomical Society Geophysical Journal, vol. **30**, 109-185.

Mehegan, J., 1988. Temporal, spatial, and chemical evolution of the Troodos ophiolite lavas, Cyprus: Supra-subduction zone volcanism in the Tethys Sea: unpublished Ph.D. thesis. Dalhousie University, Halifax, 700 p.

Merrill, R.T., 1970. Low-temperature treatments of magnetite and magnetite-bearing rocks. Journal of Geophysics Research **75**, 3343-3349.

Miyashiro, A., 1973. *Metamorphism and Metamorphic Belts.* George Allen and Unwin, 492 pp.

Moores, E.M., and Vine, F.J., 1971. The Troodos massif, Cy7rus and other ophiolites as oceanic crust: evolution and implications. Philosophical Transactions of the Royal Society, London, A**268**, 443-466.

Morris, A., 1996. A review of palaeomagnetic research in the Troodos ophiolite, Cyprus. Palaeomagnetism and Tectonics of the Mediterranean Region. Special Publication-Geologiccal Society of London, vol. **105**, 311-324.

Morris, A and Tarling, D, 1996. Paleomagnetism and tectonics of the Mediterranean region. Geological Society of London, Special Publications **105.**

Moskowitz, B.M., Jackson, M. and Kissel, C., 1998. Low-temperature magnetic behavior of titanomagnetites. Earth Planet.Sci. Letters, **157**, 141-149.

Mukasa, S.B. and Ludden, J.N., 1987. Uranium-lead ages of plagiogranites from the Troodos ophiolite, Cyprus, and their tectonic significance. Geology **1**, 82-828.

Murton, B., 1986. The tectonic evolution of the western Limassol Forest Complex, Cyprus. Unpublished Ph.D. Thesis, Open University, 322pp.

Murton, B. and Gass, I.G., 1986. Western Limassol Forest Complex, Cyprus. Part of an Upper Cretaceous leaky transform fault. Geology, vol. **14**, 255-258.

Mutter, J.C. and Karson, J.A., 1992. Structural process at slow spreading ridges. Science **257**, 627-634.

Muxworthy, A.R. and McClelland, E., 2000. The causes of low-temperature demagnetization of remanence in multidomain magnetite. Geophysics J. Int., **140**, 115-131

Natland, J. H., 1980. Effects of axial magma chambers beneath spreading centres on the compositions of basaltic rocks. Initial Rep. Deep Sea Drill, Proj. LIV, 833-850.

Noiret, G., Montigny, R. and Allegre, C.J., 1981. Is the Vourinos complex an island arc ophiolite? Earth and Planetary Science Letters, **56**, 375-386.

O'Reilly, W., 1976. Magnetic minerals in the crust of the earth. Rep. Prog. Phys., **39**, 857-908.

O'Reilly, W., 1984. *Rock and Mineral Magnetism*, Blackie and Sons, Glasgow, p.220.

Oudin, E. and Constantinou, G., 1984. Black smoker chimney fragments in Cyprus sulphide deposits. Nature, vol. **308**, 349-353.

Özdemir, Ö. and O'Reilly, 1981. High-temperature hysteresis and other magnetic properties of synthetic monodomain titanomagnetites. Physics of the Earth and Planetary Interiors, **25**, 406-418.

Özdemir, Ö. and O'Reilly, 1982. Magnetic hysteresis properties of synthetic monodomain titanomaghemites. Earth and Planetary Science Letters, **57**, 437-447.

Pearce, J.A., 1975. Basalt geochemistry used to investigate past tectonic environments on Cyprus. Tectonophysics, **25**, 41-75.

Pearce, J.A. and Cann, J.R., 1973. Tectonic setting of basic volcanic rocks determined using trace element analysis. Earth and Planetary Science Letters, **19**, 290-300.

Pearce, J.A. and Lippard, S.J., and Roberts, S., 1984. Characteristics and tectonic significance of supra-subduction zone ophiolites. Special Pulb. Geol.Soc.London.

Pariso, J. and Johnson, H.P., 1989. Magnetic properties of an analog of the lower oceanic crust: magnetic logging and palaeomagnetic measurements from drill hole CY-4 in the Troodos ophiolite. *In:* Cyprus Crustal Study Project: Initial Report, Hole CY-4; Energy, Mines and Resources Canada, Paper 88-9, p. 279-294.

Parry, L.G., 1982. Magnetization of immobilized particle dispersions with two distinct particle sizes. Phys. Earth Planetary Interiors, **28**, 230-241.

Phipps Morgan, J, and Chen, Y., 1993. The Genesis of Oceanic Crust: Magma Injection, Hydrothermal Circulation, and Crustal Flow. Journal of Geophysical Research, vol. **98**, 6283-6297.

Purdy, G.M., Kong, L.S.L., Christeson, G. L. and Solmon, S., 1992. Relationship between spreading rate and the seismic structure of mid-oceanic ridges. Nature, **335**, 815-817.

Rautenschlein, M., Jenner, G., Hertogen, J., Hofmann, A., Kerrich, J., Schmincke, H. and White, W., (1985). Isotopic and trace element composition of volcanic glass from the Akaki Canyon, Cyprus. Earth Planetary Science Letters, **75**, 369-383.

Raymond, L.A. 1995. *Petrology the study of Igneous sedimentary, metamorphic rocks.* Dubuque, IA:Wn.C. Brown Publishers.

Raymond, C.A and LaBreque, J.L., 1987. Magnetization of the Oceanic Crust: Thermoremanent Magnetization of Chemical Remanent Magnetization? Journal of Geophysical Research, **92**, no B8, 8077-8088.

Richardson, C.J., Cann, J.R., Richards, H.G., and Cowan, J.G., 1988. Metal depleted root zones of the Troodos ore-forming hydrothermal systems, Cyprus. Earth and Planetary Science Letters, **84**, 243-253.

Robertson, A.H.F., 1990. Tectonic evolution of Cyprus. In: Malpas, J., Moores, E.M., Panayioutou, A., and Xenophontos, C., eds., Ophiolites: Ocean Crustal Analogues. Proc. 'Troodos 87' Symposium. Cyprus Geological Survey Department, 235-250

Robertson, A.H.F., 2000. Tectonic evolution of Cyprus in its Eastern Mediterranean setting. In Panayides, I., Xenophontos, D., and Malpas, J., eds., Proceedings of the Third International Conference on the Geology of the Eastern Mediterranean, 11-42.

Robertson, A.H.F., 2002. Overview of the genesis and emplacement of Mesozoic ophiolites in the Eastern Mediterranean Tethyan region. Lithos **65**, 1-67.

Robertson, A.H.F., 2004. Development of concepts concerning the genesis and emplacement of Tethyan ophiolites in the Eastern Mediterranean and Oman regions. Earth Science Reviews **66**, 331-387.

Robertson, A.H.F., and Dixon, J.E., 1984. Introduction: aspects of the geological evolution of the Eastern Mediterranean. Geological Society, London, Special publications, **17**, 1-74.

Robertson, A.H.F., and Woodcock, N., H., 1986. The geological evolution of the Kyrenia Range: a critical lineament in the Eastern Mediterranean, in Reading, H.G., Watterson, J., and White, S.H., eds., Major

crustal lineaments and their influence on the geological history of the continental lithosphere. Philosophical Transactions of the Royal Society of London, vol. A**317**, 141-171.

Robertson, A.H.F. and Xenophontos, C., 1993. Development of concepts concerning the Troodos ophiolite and adjacent units in Cyprus. *In*: Prichard, H.M., Alabaster, T., Harris, N.B.W and Neary, C.R. (eds), Magmatic Processes and Plate Tectonics, Geological Society Special Publication **76**, 85-119.

Robertson, A.H.F., Clift, P.D., Degnan, P.J. and Jones, G., 1991. Palaeogeographical and palaeotectonic evolution of the eastern Mediterranean Neotethys. Palaeoceanography, Palaeoclimatology and Palaeoecology **87**, 289-343.

Robertson, A.H.F., Dixon, J., Brown, S., Collins, A., Morris, A., Pickett, E., Sharp, I. and Ustaomer, T., 1996. Alternative tectonic models for the Late Paleozoic-Early Tertiary development of Tethys in the eastern Mediterranean region. *In:* Morris, A. and Tarling, D. (eds), Paleomagnetism and tectonics of the Mediterranean region. Geological Society of London, Special Publications 105, p. 239-263.

Robinson, P.T., 1987. The Troodos ophiolite of Cyprus: new perspectives on its origin and emplacement. In: Troodos 87, Ophiolites and oceanic lithosphere. Abstracts. Cyprus Geological Survey Department, 3.

Robinson, P.T., and Malpas, J., 1987. The Cyprus Crustal Study Project: Ophiolites and Oceanic Lithosphere, Troodos. 15-26.

Robinson, P.T., 1989. Hole CY-4 of the Cyprus Crustal Study Project: background and objectives. *In:* Cyprus Crustal Study Project: Initial Report, Hole CY-4; Energy, Mines and Resources Canada, Paper 88-9, p.1-4.

Rochette, P., 1987. Metamorphic control of the mineralogy of black shales in the Swiss Alps: toward the use of "magnetic isograds:. Earth and Planetary Science International, **82**, 113-123.

Rochette, P., 1988. Inverse magnetic fabric carbonate bearing rocks. Earth and Planetary Science Letters, **90**, 229-237.

Rochette, P., and Vialon, P., 1984. Development of planar and linear fabrics in Daupinois shales and slates (French Alps) studied by magnetic anisotropy and its mineralogical control. Journal of Structural Geology, **6**, 33-38.

Rochette, P., Jackson, J., and Aubourg, C., 1992. Rock magnetism and the interpretation of anisotropy of magnetic susceptibility. Reviews of Geophysics, **30**: 209-226.

Rochette, P., Aubourg, C., and Perrin, M., 1999. Is this magnetic fabric normal? A review and case studies in volcanic formations. Tectonophysics, **307**, 219-234.

Schiffmah, P., Smith, B.M., Varga, R.J., and Moores, E.M., 1987. Geometry, conditions and timing of off axis hydrothermal metamorphic and ore deposition in the Solea graben, N. Troodos ophiolite, Cyprus. Nature vol. **325**, 423-425.

Schirmer, W., 2000. Neogene submarine relief and Troodos uplift in southeastern Cyprus. *In*: Panayides, I., Xenophontos, C. and Malpas, J., (eds), Proceedings of the Third International Conference on the Geology of the Eastern Mediterranean.

Schmincke, H. and Bednarz, U., 1990. Pillow, sheet flows and breccia flow volcanoes and volcano-tectonic hydrothermal cycles in the extrusive series of the northeastern Troodos ophiolite, Cyprus. In: Malpas, J., Moores, E.M., Panayiotou, A., Xenophontos, C. (Eds.), Ophiolites: Oceanic Crustal Analogues. Cyprus Geological Survey Department, 207-216.

Schmincke, H., Rautenschlein, M., Robinson, P.T. and Mehegan, J., 1983. Troodos extrusive series of Cyprus: a comparison with oceanic crust. Geology, **11**, 405-409.

Şengör, A.M.C., 1985. The story of Tethys: how many wives did Okeanos have? Episodes **8**, 3-12.

Siddans, A.W.B., Henry, B., Klingfield, R., Lowrie, W., Hirt, A and Percevault, M.N., 1984. Finite strain patterns and their significance in Permian rocks of the Alpes Maritimes (France). Journal of Structural Geology, **6**, 339-368.

Simonian, K.O. and Gass, I., 1978. Arakapas fault belt, Cyprus: A fossil transform fault. Geological Society, American Bulletin. **89**, 1220-1230.

Sleep, N.H., and Barth, G.A. 1997. The Nature of Oceanic Lower Crust and Shallow Mantle Emplaced at Low Spreading Rates. Tectonphysics, **279**, 181-191.

Smewing, J., 1975. Metabasalts of the Troodos massif, Cyprus. Ph.D. thesis, Open University, Milton Keynes.

Smith, A.G., and Spray, J.G., 1984. A half-ridge transform model for the Hellenic-Dinaric ophiolites. In Dixon, J.E., and Robertson, A.H.F., eds, The geological evolution of the Eastern Mediterranean: Geological Society of London Special Publications: No. **17**, 629-644.

Spray, J.G., and Roddick, J.C., 1981. Evidence for Upper Cretaceous transform fault metamorphism in West Cyprus. Earth and Planetary Science Letters, **55**, 273-291.

Stacey, F.D., 1962. A generalized theory of thermoremanence, covering the transition from single domain to multi-domain magnetic grains. Philos. Mag., **7**, 1887-1900.

Stampfli, G., Mosar, J., Faure, P., Pillevuit. and Vannay, J.C., 2001. Permo-Mesozoic evolution of the western Tethys real: the Neotethys East Mediterranean basin connection. In: Ziegler, P., Cavazza, W., Robertson, A.H.F., Crasquin-Soleau, S., (Eds.), Peri-Tethys Memoir no. 5 Peri-Tethyan Rift/Wrench Basins and Passive Margins, Memoirs du Museum National, D'Histoire Naturelle, 51-108.

Steiner, M.B., 1983. Mesozoic apparent polar wander and plate motion of North America. In: Reynolds, N.W., and Dolly, E.D., eds, Mesozoic paleogeography of West-Central United States. Soc. Econ. Paleont. Mineral, Special Publication Rocky Mountain Sect., Denver, Colorado, 1-11.

Stephenson, A., 1994. Distribution anisotropy: two simple models for magnetic lineation and foliation. Physics of the Earth and Planetary Interiors, **82**, 49-53.

Syono, Y., 1960. Magnetic susceptibility of some rock forming silicate minerals such as amphiboles, biotites, cordierites and garnets: Journal of Geomagnetism and Geoelectricity, **11**, no.3, p.85-93.

Tarling, D.H., 1983. Palaeomagnetism: Principles and applications in geology, geophysics and archaeology. Chapman and Hall, London, UK, 379 pp.

Tarling, D.H., and Hrouda, F., 1993. *The Magnetic Anisotropy of Rocks*. Chapman and Hall, London, UK, 217 pp.

Tarney, J. and Marsh, H.G., 1991. Major and trace element geochemistry of Holes Cy-1 and Cy-4: implications for petrogenetic models. In: Gibson, I.L., Malpas, J., Robinson, P.T., and Xenophontos, C., (Eds.), Initial Reports of the Cyprus Crustal Study. Geological Survey of Canada, Paper 90-20, 133-176.

Tauxe, L., Mullender, T.A.T. and Pick, T., 1996. Potbellies, wasp-waists, and superparamagnetism in magnetic hysteresis. J. Geophys. Res., **101**, 571-583.

Tauxe, L., Bertram, H.N. and Seberino, C., 2002. Physical interpretation of hysteresis loops: Micromagnetic modeling of fine particle magnetite. Geochem. Geophys. Geosys. **3**. 1055.

Thy, P., Brooks, C.K. and Walsh, J.N., 1985. Tectonic and petrogenetic implications of major and rare earth element chemistry of Troodos glasses, Cyprus. Lithos, **18**, 165-178.

Ustaömer, T. and Robertson, A.H.F., 1994. Late Palaeozoic marginal basin and Subduction-accretion: evidence from the Palaeotethyan Kure Complex, Central Pontides, N. Turkey. Journal of the Geological Society (London) **151**, 291-305.

Uyeda, S., Fuller, M.D., Belshe, J.C. and Girdler, R.W., 1963. Anisotropy of magnetic susceptibility of rocks and minerals. J. Geophys. Res., **68**, 279-291.

Van Der Voo, R., 2004. *Paleomagnetism of the Atlantic, Tethys and Iapetus oceans.* Cambridge University PressCambridge, UK, 411 pp.

Varga, R.J. and Moores, E.M., 1985. Spreading structure of the Troodos ophiolite, Cyprus. Geology, vol. **13**, 846-850.

Verwey, E.J.W., 1939. Nature, **144**, 327-328.

Voight, W. and Kinoshita, S., 1907. Bestimmung absoluter Werte von Magnetisierungszahlen, insbesondere fur Kristalle. Ann. Phys. **24**, 492-514.

Wang, D. and Van der Voo, R., 2004. The hysteresis properties of multidomain magnetite and titanomagnetite/titanomaghemite in mid-ocean ridge basalts. Earth and Planetary Science Letters **220**, 175-184.

Wasilewki, P.J., 1973. Magnetic Hysteresis in natural materials. Earth and Planetary Science Letters **20**, 67-72.

Weiss, P., 1907. L'hypothese du champ moleculaire et la propriete ferromagnetique. Journ. Phys. **6**, 661.

Werner, T. and Borradaile, G.J., 1996. Paleoremanence Dispersal across a transpressed Archean Terrain: Deflection by anisotropy or by late compression? Journal of Geophysical Research, **10**, 5531-5545.

Wilson, M., 1991. *Igneous Petrogenesis: A Global Tectonic Approach.* Harper Collins Academic, London.

Appendix A: AMS Data

	Kmin. (μ SI)			Kint. (μ SI)			Kmax. (μ SI)					
Sample	Dec.	Inc.	Intensity	Dec.	Inc.	Intensity	Dec.	Inc.	Intensity	Bulk k	Pj	Tj
CY40010A	282.5	2.7	30732	12.5	0.8	30876	118.0	87.2	31178	30928	1.015	-0.350
CY40010B	119.0	1.6	25290	29.0	1.2	25375	261.9	88.0	25682	25449	1.016	-0.561
CY40010C	84.4	3.5	26392	174.4	1.2	26580	282.7	86.3	26900	26623	1.019	-0.254
CY40072A	215.7	32.1	121690	122.0	5.8	125774	22.9	57.3	127514	124969	1.049	0.412
CY40072B	232.2	3.6	135225	326.5	50.3	136582	139.2	39.5	138361	136717	1.023	-0.129
CY40115	250.8	49.9	88801	134.8	20.3	107332	31.0	32.9	111660	102097	1.278	0.655
CY40151A	50.9	22.4	64518	308.9	26.7	67008	175.2	53.9	67447	66312	1.049	0.706
CY40151B	51.0	17.0	67757	153.5	35.4	70778	300.0	49.6	71207	69897	1.056	0.757
CY40151C	49.8	29.9	56752	305.2	23.7	59331	183.4	50.2	59569	58537	1.055	0.835
CY40151D	44.1	28.7	68858	226.7	61.3	71792	134.7	1.1	72146	70916	1.053	0.789
CY40187A	184.6	0.6	80746	276.0	65.2	84900	94.3	24.8	85258	83609	1.062	0.845
CY40187B	183.2	0.0	80431	273.1	73.7	84482	93.2	16.3	85007	83281	1.063	0.776
CY40187C	9.5	1.5	81551	277.4	55.1	85546	100.5	34.9	85945	84324	1.060	0.823
CY40187D	3.3	1.2	78051	271.0	61.9	81981	93.9	28.0	82517	80825	1.063	0.766
CY40224A	332.3	2.8	69506	241.3	19.9	73242	70.0	69.9	75280	72636	1.084	0.312
CY40224B	316.3	10.4	94693	224.6	8.9	98975	94.9	76.2	101830	98455	1.076	0.217
CY40224C	330.0	2.5	88857	238.6	29.1	94293	64.4	60.7	96845	93272	1.092	0.380
CY40250A	217.1	7.7	137033	122.2	32.8	149481	318.7	56.1	153520	146507	1.126	0.531
CY40250B	214.5	3.9	118770	122.0	32.8	130942	310.5	56.9	133850	127683	1.136	0.632
CY40297A	200.2	44.5	55233	45.9	42.5	59741	303.5	13.2	61624	58804	1.119	0.433
CY40297B	178.1	55.3	53788	46.9	24.5	56820	305.8	22.9	59224	56567	1.101	0.139
CY40297C	265.7	35.5	51264	59.4	51.5	52841	166.2	13.0	54868	52970	1.070	-0.108
CY40297D	265.2	39.9	53093	51.7	45.0	56012	160.0	17.4	57232	55418	1.080	0.426
CY40349A	352.1	1.6	58493	82.6	17.2	62405	257.0	72.7	64408	61719	1.103	0.344
CY40349B	170.0	2.5	56660	77.4	46.4	61305	262.4	43.5	62322	60044	1.107	0.655
CY40349C	351.7	0.1	58879	81.7	13.6	62629	261.2	76.4	64852	62071	1.103	0.278
CY40349D	175.3	1.2	58083	85.0	13.5	61967	270.3	76.4	63585	61168	1.098	0.430
CY40382A	171.1	0.6	81221	81.0	3.6	86927	270.6	86.3	90415	86103	1.115	0.266
CY40382B	42.9	31.9	67597	139.0	9.8	109172	243.9	56.3	118535	95637	1.842	0.707
CY40382C	339.7	1.2	59097	69.7	0.3	60802	172.9	88.8	65361	61697	1.109	-0.435
CY40382D	343.1	1.7	47105	252.8	8.6	48305	84.3	81.2	51495	48934	1.096	-0.435
CY40407A	359.2	11.7	103170	91.0	8.6	110002	216.4	75.4	114093	108994	1.107	0.274
CY40407B	358.4	13.4	106349	89.0	2.3	113721	188.7	76.4	118258	112668	1.113	0.263
CY40407C	2.6	13.1	101936	95.3	11.1	108736	224.4	72.7	112336	107582	1.104	0.329
CY40490A	37.9	14.1	139415	130.5	10.3	150218	255.6	72.4	161703	150170	1.160	0.006
CY40490B	42.8	14.1	137300	134.5	6.7	146393	249.3	74.3	156581	146547	1.141	-0.024
CY40490C	28.0	13.4	149745	120.8	11.6	159951	250.3	72.1	174279	161013	1.164	-0.131
CY40553A	300.6	18.8	137543	35.2	13.1	158664	158.0	66.8	161002	152025	1.190	0.814
CY40553B	308.5	19.5	142938	52.7	34.7	159036	194.7	48.8	166654	155891	1.171	0.390
CY40553C	303.5	23.5	146683	34.2	1.6	163503	127.8	66.4	165908	158462	1.144	0.763
CY40553D	301.2	20.1	128669	47.0	36.7	153872	188.6	46.4	162772	147708	1.279	0.522
CY40589A	251.0	4.0	72442	347.2	56.8	76920	158.4	32.9	79586	76258	1.100	0.275
CY40589B	235.2	7.0	99930	327.9	21.0	106125	127.8	67.7	107993	104625	1.085	0.550
CY40589C	228.1	19.9	79610	2.5	62.6	85368	131.3	18.0	86596	83802	1.094	0.660
CY40589D	250.7	16.6	97218	352.5	34.4	103078	139.4	50.7	104503	101550	1.080	0.620
CY40629A	27.1	11.2	5159	123.2	28.4	5386	277.8	59.0	5641	5392	1.093	-0.038
CY40629B	30.9	18.5	5159	131.5	28.8	5340	272.6	54.8	5529	5341	1.072	-0.004
CY40629C	21.5	7.6	3971	115.3	26.2	4188	276.6	62.6	4360	4170	1.098	0.139
CY40629D	27.1	11.3	4417	120.5	16.4	4539	264.1	69.9	4738	4563	1.073	-0.222
CY40681A	2.2	26.5	24079	100.3	15.8	25474	217.8	58.4	26457	25318	1.099	0.196
CY40681B	3.3	30.6	14851	106.5	21.1	15526	225.4	51.4	16032	15462	1.080	0.162
CY40681C	6.2	34.3	22898	129.8	39.0	24381	250.6	32.3	24923	24052	1.092	0.482
CY40681D	6.0	35.4	24950	110.5	19.4	27011	223.6	48.1	27758	26546	1.117	0.488
CY40726A	134.5	38.2	2379	226.2	2.1	2463	318.9	51.7	2535	2458	1.066	0.099
CY40726B	150.1	34.7	1078	45.1	20.5	1099	290.5	48.1	1108	1095	1.029	0.401
CY40726C	136.6	68.9	5448	1.5	15.3	5605	267.5	14.2	5768	5605	1.059	-0.004
CY40726D	157.2	40.9	3106	63.7	4.1	3274	329.0	48.8	3356	3244	1.082	0.360
CY40726E	141.3	33.2	1273	248.4	24.2	1296	7.1	46.8	1328	1299	1.043	-0.133
CY40781A	100.8	8.6	69300	191.6	5.0	79702	311.2	80.0	81167	76535	1.189	0.770
CY40781B	99.2	11.1	44071	196.8	33.9	51327	353.6	53.8	52718	49221	1.213	0.702
CY40781C	116.7	22.0	29424	218.6	27.1	33645	353.0	53.9	35281	32688	1.207	0.477
CY40781D	110.2	10.0	41118	204.0	20.7	46076	356.0	66.8	47042	44668	1.156	0.692
CY40812A	332.5	44.8	5660	77.1	14.3	5778	180.2	41.7	5905	5780	1.043	-0.030
CY40812B	283.1	35.5	6754	27.5	19.2	6917	140.5	48.1	7227	6963	1.071	-0.298

Appendix A: AMS Data

	Kmin. (μ SI)			Kint. (μ SI)			Kmax. (μ SI)					
Sample	Dec.	Inc.	Intensity	Dec.	Inc.	Intensity	Dec.	Inc.	Intensity	Bulk k	Pj	Tj
CY40812C	298.4	30.0	16769	54.0	36.8	18017	180.9	38.7	18547	17762	1.109	0.425
CY40812D	308.2	11.1	10735	50.6	47.6	10894	208.6	40.2	11425	11014	1.067	-0.529
CY40812E	291.9	15.6	30031	76.3	71.1	31226	199.0	10.5	32606	31270	1.086	-0.051
CY40862A	295.2	9.1	1602	201.8	19.9	1675	48.5	68.0	1733	1669	1.082	0.140
CY40862B	285.7	7.6	1659	192.5	23.0	1727	32.8	65.7	1775	1720	1.071	0.197
CY40892A	160.6	21.4	4096	63.2	18.2	4431	296.2	61.3	4661	4390	1.139	0.217
CY40892B	158.6	24.4	3401	60.0	18.1	3668	297.3	58.8	3861	3638	1.136	0.192
CY40892C	166.5	19.2	4678	265.8	25.0	5023	43.2	57.7	5087	4926	1.095	0.699
CY40957A	318.8	40.1	2981	169.3	45.7	3337	62.5	15.8	3353	3219	1.142	0.919
CY40957B	319.4	42.1	2485	74.1	24.8	2770	185.1	37.8	2784	2676	1.137	0.912
CY40957C	308.2	39.4	4699	209.6	10.4	5484	107.6	48.8	5647	5259	1.219	0.682
CY40957D	308.1	33.4	3296	45.9	11.6	3809	152.4	54.1	3908	3661	1.202	0.699
CY40994A	255.4	36.0	3182	135.9	34.1	3402	16.8	35.7	3525	3367	1.110	0.303
CY40994B	266.1	39.3	3152	142.2	34.4	3438	26.9	32.0	3521	3366	1.124	0.567
CY40994C	267.2	37.8	3143	148.2	32.0	3446	31.3	35.9	3550	3375	1.136	0.514
CY41036A	313.3	26.0	5730	218.3	10.2	6190	108.7	61.8	6358	6087	1.114	0.485
CY41036B	320.6	29.8	7129	230.0	1.0	7702	138.2	60.2	8007	7604	1.125	0.332
CY41036C	250.4	50.6	1910	133.5	20.4	1994	30.1	32.1	2029	1977	1.064	0.419
CY41060A	326.8	26.2	71143	61.3	9.0	74112	168.7	62.1	78585	74551	1.105	-0.178
CY41060B	325.2	22.4	65448	62.4	16.9	68893	186.1	61.4	72384	68850	1.106	0.018
CY41060C	324.3	25.7	67169	61.5	14.5	70292	178.1	59.9	74444	70572	1.109	-0.116
CY41129A	125.0	8.3	58784	218.6	23.3	68283	16.7	65.1	73771	66653	1.260	0.319
CY41129B	118.1	10.6	52811	211.3	16.5	61738	356.7	70.2	64791	59557	1.239	0.528
CY41129C	119.6	7.6	56704	212.9	23.4	66462	12.8	65.3	69561	64001	1.240	0.554
CY41129D	125.1	5.6	58287	217.9	26.5	67391	24.2	62.9	72950	65927	1.256	0.294
CY41179A	309.7	20.6	24506	132.2	69.4	26960	40.0	0.8	27096	26160	1.120	0.900
CY41179B	326.1	25.0	22490	200.8	51.1	25006	70.3	27.7	25372	24255	1.141	0.759
CY41179C	326.1	25.6	22571	196.1	53.2	25161	68.6	24.4	25513	24379	1.144	0.773
CY41237A	48.5	15.8	9518	308.7	31.0	10435	161.7	54.4	10951	10284	1.153	0.311
CY41237B	51.0	13.9	11309	311.4	34.0	12346	159.8	52.5	12823	12143	1.138	0.396
CY41237C	45.5	19.9	11000	296.6	41.8	12104	154.1	41.5	12655	11900	1.154	0.365
CY41237D	40.3	17.0	12844	295.0	40.8	13639	147.6	44.3	14389	13609	1.120	0.057
CY41294A	210.0	16.3	18906	106.3	39.0	21097	317.8	46.4	22029	20635	1.171	0.435
CY41294B	220.6	17.6	16097	119.4	31.4	17834	335.4	52.9	19033	17613	1.184	0.224
CY41294C	204.7	17.0	12400	103.9	31.6	14135	318.8	53.1	14846	13754	1.205	0.455
CY41294D	207.9	19.9	7834	108.6	24.0	8509	333.3	58.0	9280	8521	1.185	-0.024
CY41305A	207.5	25.3	1731	99.0	33.8	1796	326.3	45.4	1835	1787	1.060	0.272
CY41305B	200.4	25.1	2024	95.0	29.7	2118	323.4	49.3	2161	2100	1.069	0.382
CY41305C	203.1	23.7	1912	98.0	30.6	1988	324.1	49.5	2032	1977	1.064	0.282
CY41345A	181.0	19.9	2127	89.4	4.4	2188	347.6	69.5	2191	2168	1.034	0.910
CY41345B	175.4	31.1	1938	291.3	35.8	1998	56.6	38.6	2005	1980	1.038	0.794
CY41423A	57.4	39.7	13539	158.7	13.3	17666	263.5	47.3	19958	16838	1.489	0.371
CY41423B	62.4	37.3	6931	158.3	7.6	8564	257.9	51.6	9527	8270	1.383	0.330
CY41423C	32.0	24.4	4986	139.2	33.1	5798	273.1	46.8	6121	5614	1.237	0.471
CY41469A	213.4	26.8	2947	313.4	19.0	3157	74.4	56.3	3221	3106	1.098	0.549
CY41469B	214.3	26.5	2813	317.6	24.7	3002	84.1	52.3	3076	2962	1.097	0.456
CY41469C	209.3	26.9	2288	325.0	40.5	2450	96.2	37.7	2503	2412	1.098	0.521
CY41469D	224.7	30.5	3789	131.2	5.8	4020	31.5	58.8	4084	3962	1.082	0.578
CY41520A	19.5	39.9	903	241.3	41.7	940	129.7	22.4	1010	950	1.120	-0.291
CY41520B	52.1	45.3	1088	152.1	9.7	1189	251.2	43.1	1230	1167	1.135	0.442
CY41520C	295.4	14.8	860	187.9	48.9	864	37.0	37.4	885	869	1.031	-0.679
CY41594A	257.5	4.8	4281	162.9	43.7	4478	352.4	45.9	4591	4448	1.074	0.291
CY41594B	80.8	0.5	3177	171.3	43.0	3322	350.3	47.0	3380	3292	1.066	0.440
CY41594C	254.1	4.0	3753	161.2	36.0	3939	349.7	53.7	4036	3907	1.077	0.331
CY41672A	32.4	19.1	2128	263.1	61.4	2178	129.9	20.5	2255	2186	1.060	-0.208
CY41672B	234.6	37.0	2387	24.5	48.9	2512	132.7	15.2	2633	2509	1.103	0.043
CY41672C	238.1	40.1	1957	351.4	25.2	2000	104.2	39.5	2084	2013	1.065	-0.304
CY41730A	222.8	9.6	2173	120.6	51.1	2232	320.2	37.2	2428	2275	1.123	-0.514
CY41730B	208.9	21.2	2487	94.4	47.0	2597	314.8	35.4	2803	2626	1.129	-0.275
CY41780A	244.0	1.5	1007	337.1	63.2	1047	153.3	26.7	1078	1043	1.070	0.142
CY41780B	60.6	16.9	1239	329.6	3.5	1296	228.2	72.8	1331	1288	1.075	0.264
CY41780C	142.1	59.5	756	278.7	23.2	764	17.0	18.7	809	776	1.076	-0.679
CY41810A	293.8	17.0	14897	27.4	11.8	16057	150.6	69.1	16321	15746	1.102	0.643
CY41810B	286.4	10.0	21123	19.3	16.1	21755	165.7	70.9	22650	21834	1.073	-0.155

Appendix A: AMS Data

	Kmin. (μSI)			Kint. (μSI)			Kmax. (μSI)					
Sample	Dec.	Inc.	Intensity	Dec.	Inc.	Intensity	Dec.	Inc.	Intensity	Bulk k	Pj	Tj
CY41810C	284.4	8.1	15157	15.6	8.4	16493	151.3	78.3	16734	16113	1.113	0.706
CY41915A	255.3	9.9	4874	160.3	26.6	6864	4.0	61.3	7591	6333	1.594	0.546
CY41915B	253.3	19.7	3100	149.6	33.5	4162	8.3	49.8	4468	3863	1.475	0.612
CY41995A	269.7	18.0	840	0.6	2.9	869	99.6	71.7	893	867	1.062	0.107
CY41995B	267.4	35.5	537	48.5	47.5	546	162.2	20.2	557	547	1.038	-0.045
CY42070A	278.0	36.5	16753	168.9	23.9	18533	53.6	44.0	20515	18537	1.225	-0.003
CY42070B	138.4	0.4	1240	230.2	77.2	1291	48.3	12.8	1302	1277	1.054	0.641
CY42070C	280.5	31.5	4701	170.2	29.6	6330	46.8	44.1	6450	5768	1.427	0.882
CY42097A	263.7	56.8	815	5.2	7.4	843	99.9	32.1	870	843	1.067	0.042
CY42097B	261.6	59.7	151	358.2	3.8	156	90.4	30.0	161	156	1.064	-0.089
CY42131A	79.5	39.8	1274	187.8	20.7	1294	298.4	43.0	1349	1306	1.061	-0.466
CY42131B	28.7	6.3	1407	124.8	43.7	1445	292.1	45.6	1472	1441	1.046	0.180
CY42158A	155.5	58.3	1183	332.5	31.7	1306	63.3	1.4	1454	1310	1.230	-0.039
CY42158B	235.8	72.8	1009	27.8	15.3	1087	119.9	7.7	1119	1071	1.112	0.452
CY42158C	355.3	62.1	1149	257.6	4.0	1222	165.5	27.5	1309	1225	1.140	-0.059
CY42250A	124.4	64.1	58466	348.4	19.3	68667	252.4	16.6	68978	65181	1.207	0.945
CY42250B	324.9	85.0	62789	125.6	4.7	72428	215.8	1.6	75496	70023	1.214	0.550

Appendix B: Critical temperature points

Sample	Temp. (C) during Heating
10	277
10	337
10	539
10	601
10	666
187	221
187	293
187	572
187	690
250	186
250	347
250	576
349	575
349	667
490	310
490	570
553	175
553	579
629	317
629	575
629	679
726	200
726	573
812	211
812	566
812	681
994	518
994	670
1060	148
1060	555
1060	650
1179	516
1179	571
1179	662
1294	511
1294	579
1294	675
1345	585
1345	664
1423	573
1423	668
1520	312
1520	563
1520	680
1672	358
1672	575
1810	580
1810	675
1915	579
1915	665
2070	520
2250	185
2250	298
2250	579
2250	663

Sample	Temp. (C) during Cooling
349	581
490	680
629	171
629	278
726	665
994	490
994	545
1060	240
1060	565
1179	500
1294	500
1294	592
1294	680
1345	680
1423	583
1520	325
1520	582
1672	314
1672	419
1672	670
1810	680
2070	678
2250	680

Appendix C: Hysteresis Data

1st Run

Sample	Hc (mT)	Mr/Ms	Hcr (mT)	Hcr/Hc
10	8.98	0.080	34.08	3.79
72	3.86	0.028	37.03	9.59
115	18.28	0.172	36.22	1.98
151	7.53	0.072	23.75	3.15
187	6.07	0.071	15.49	2.55
224	4.19	0.047	14.36	3.43
250	3.67	0.038	15.25	4.16
297	3.87	0.041	15.78	4.08
349	3.89	0.042	16.94	4.36
382	2.83	0.029	12.66	4.47
407	3.98	0.053	12.37	3.11
490	2.57	0.026	13.96	5.43
553	2.97	0.034	12.78	4.30
589	3.50	0.029	27.33	7.82
629	13.41	0.126	42.53	3.17
681	5.05	0.061	16.46	3.26
726	5.43	0.070	18.32	3.37
781	3.26	0.044	12.07	3.71
812	6.21	0.057	32.59	5.25
862	8.47	0.102	29.14	3.44
892	13.53	0.185	27.06	2.00
957	10.34	0.140	23.18	2.24
994	9.03	0.102	26.91	2.98
1036	6.16	0.072	22.29	3.62
1060	5.97	0.070	17.38	2.91
1129	4.18	0.035	23.04	5.51
1179	8.46	0.079	27.48	3.25
1237	5.67	0.082	15.56	2.74
1294	13.74	0.201	23.74	1.73
1305	9.16	0.096	25.71	2.81
1345	8.77	0.092	25.71	2.93
1423	9.00	0.132	17.15	1.91
1469	5.42	0.063	14.80	2.73
1520	2.78	0.020	27.18	9.77
1594	9.71	0.112	27.40	2.82
1672	5.96	0.063	23.43	3.93
1730	7.54	0.117	18.34	2.43
1780	7.06	0.066	13.97	1.98
1810	11.43	0.298	16.22	1.42
1915	8.81	0.179	14.36	1.63
1995	4.70	0.069	21.49	4.57
2070	14.28	0.234	23.70	1.66
2097	11.31	0.119	29.55	2.61
2131	12.59	0.281	20.43	1.62
2158	12.03	0.372	16.62	1.38
2250	14.36	0.272	20.05	1.40

Appendix C: Hysteresis Data

2nd Run

Sample	Hc (mT)	Mr/Ms	Hcr (mT)	Hcr/Hc
10	7.57	0.068	31.57	4.17
72	2.99	0.026	18.16	6.07
115	6.82	0.056	25.68	3.77
151	6.28	0.061	20.62	3.28
187	5.84	0.072	16.61	2.85
224	4.59	0.052	14.52	3.16
250	3.64	0.038	14.76	4.05
297	3.90	0.041	16.20	4.15
349	3.51	0.035	17.67	5.03
382	2.79	0.026	13.58	4.86
407	4.29	0.057	12.82	2.99
490	2.62	0.032	11.37	4.34
553	3.29	0.038	16.70	5.07
589	6.05	0.050	28.88	4.77
629	10.6	0.118	39.71	3.76
681	4.86	0.058	28.77	5.92
726	7.56	0.075	32.13	4.25
781	3.04	0.048	9.49	3.12
812	4.55	0.040	25.96	5.71
862	8.58	0.090	35.34	4.12
892	12.9	0.161	31.98	2.47
957	10.6	0.171	22.55	2.12
994	7.59	0.088	25.08	3.31
1036	6.85	0.065	26.71	3.90
1060	6.22	0.080	16.68	2.68
1129	4.37	0.036	24.42	5.59
1179	5.21	0.058	17.89	3.44
1237	10.9	0.143	23.96	2.20
1294	9.46	0.152	18.77	1.98
1305	9.79	0.097	29.75	3.04
1345	9.61	0.091	31.24	3.25
1423	6.46	0.168	11.15	1.72
1469	7.15	0.078	24.94	3.49
1520	5.03	0.059	19.80	3.94
1594	7.03	0.086	23.12	3.29
1672	8.01	0.072	31.17	3.89
1730	6.30	0.075	21.59	3.43
1780	9.18	0.113	24.58	2.68
1810	7.74	0.128	17.55	2.27
1915	11.9	0.209	17.32	1.45
1995	13.0	0.153	36.40	2.81
2070	13.6	0.228	23.17	1.7
2097	9.74	0.129	23.91	2.46
2131	9.96	0.124	32.06	3.22
2158	13.3	0.291	21.03	1.58
2250	15.0	0.269	21.55	1.44

Appendix C: Hysteresis Data

3rd Run

Sample	Hc (mT)	Mr/Ms	Hcr (mT)	Hcr/Hc
10	9.02	0.085	31.5	3.49
72	2.82	0.023	21.97	7.80
115	6.65	0.059	24.45	3.68
151	6.59	0.064	21.19	3.22
187	5.83	0.067	15.92	2.73
224	3.96	0.040	17.34	4.38
250	3.85	0.046	13.72	3.57
297	5.41	0.051	23.33	4.31
349	3.52	0.034	17.91	5.09
382	2.57	0.025	15.73	6.11
407	3.73	0.049	11.99	3.21
490	3.74	0.041	14.4	3.85
553	2.36	0.025	14.85	6.30
589	2.87	0.033	19.95	6.95
629	4.16	0.059	27.99	6.73
681	5.75	0.072	19.96	3.47
726	6.87	0.127	15.92	2.32
781	3.09	0.032	15.74	5.10
812	6.19	0.028	24.41	3.95
862	9.23	0.111	28.25	3.06
892	15.64	0.210	29.94	1.91
957	6.18	0.069	23.16	3.75
994	8.55	0.125	24.47	2.86
1036	5.68	0.052	24.09	4.24
1060	4.70	0.040	22.85	4.86
1129	5.00	0.039	24.58	4.91
1179	6.90	0.077	21.78	3.16
1237	10.28	0.107	26.92	2.62
1294	10.78	0.146	20.95	1.94
1305	6.28	0.058	23.31	3.71
1345	11.15	0.120	30.8	2.76
1423	7.86	0.078	39.25	4.99
1469	10.68	0.124	30.95	2.90
1520	40.98	0.516	50.59	1.23
1594	7.02	0.080	22.41	3.19
1672	8.70	0.063	31.74	3.65
1730	12.18	0.144	29.37	2.41
1780	21.10	0.272	63.93	3.03
1810	9.25	0.232	15.3	1.65
1915	14.28	0.185	31.66	2.22
1995	9.22	0.125	23.72	2.57
2070	10.37	0.208	16.48	1.59
2097	9.42	0.140	21.54	2.29
2131	14.87	0.208	28.83	1.94
2158	7.12	0.059	33.23	4.67
2250	10.98	0.178	18.36	1.67

Appendix C: Hysteresis Data

4th Run

Sample	Hc (mT)	Mr/Ms	Hcr (mT)	Hcr/Hc
10	7.59	0.063	34.18	4.50
72	2.92	0.026	16.69	5.72
115	7.24	0.064	25.40	3.51
151	6.09	0.063	19.81	3.25
187	5.44	0.072	13.89	2.55
224	4.29	0.049	14.67	3.42
250	3.66	0.042	14.63	4.00
297	3.68	0.040	14.56	3.96
349	3.87	0.041	17.79	4.60
382	2.73	0.031	11.07	4.05
407	3.78	0.047	12.71	3.36
490	3.10	0.038	13.08	4.22
553	2.34	0.022	17.60	7.51
589	6.77	0.057	36.18	5.35
629	9.16	0.105	35.73	3.90
681	4.37	0.051	17.96	4.11
726	12.97	0.119	45.13	3.48
781	3.18	0.036	17.51	5.51
812	5.55	0.068	18.66	3.37
862	4.90	0.048	29.86	6.10
892	13.37	0.165	29.37	2.20
957	6.73	0.092	19.62	2.92
994	8.20	0.094	27.87	3.40
1036	5.83	0.072	16.59	2.85
1060	5.47	0.053	19.22	3.51
1129	4.60	0.039	23.11	5.02
1179	5.66	0.073	16.67	2.94
1237	12.40	0.184	23.33	1.88
1294	9.55	0.147	20.86	2.18
1305	10.75	0.108	28.26	2.63
1345	10.61	0.161	21.73	2.05
1423	10.42	0.198	17.24	1.65
1469	8.75	0.116	26.26	3.00
1520	10.47	0.119	27.62	2.64
1594	4.40	0.039	21.09	4.80
1672	9.97	0.107	28.23	2.83
1730	7.74	0.074	28.23	3.65
1780	4.13	0.046	30.34	7.36
1810	9.55	0.171	17.42	1.82
1915	11.92	0.137	32.98	2.77
1995	6.33	0.078	24.31	3.84
2070	14.33	0.211	24.74	1.73
2097	7.73	0.086	30.65	3.97
2131	9.46	0.122	26.27	2.78
2158	11.88	0.154	26.10	2.20
2250	13.58	0.226	19.44	1.43

Appendix C: Hysteresis Data

Sample	StDEV of Mr/Ms	StDEV/Mean of Mr/Ms	StDEV/3 of Mr/Ms	StDEV of Hcr/Hc	StDEV/Mean of Hcr/Hc	StDEV/3 of Hcr/Hc	Mr/Ms Average	Hcr/Hc Average
10	0.010	0.139	0.00342	4.98	0.110	0.147	0.074	3.99
72	0.002	0.084	0.00072	35.99	0.244	0.594	0.026	7.29
115	0.056	0.637	0.01867	57.38	0.260	0.281	0.088	3.23
151	0.005	0.076	0.00165	75.49	0.017	0.019	0.065	3.23
187	0.002	0.032	0.00076	93.49	0.054	0.048	0.071	2.67
224	0.005	0.108	0.00169	111.98	0.149	0.179	0.047	3.60
250	0.004	0.096	0.00132	124.98	0.066	0.087	0.041	3.94
297	0.005	0.117	0.00168	148.48	0.036	0.049	0.043	4.13
349	0.004	0.109	0.00138	174.48	0.074	0.117	0.038	4.77
382	0.003	0.108	0.00099	190.98	0.182	0.297	0.028	4.87
407	0.004	0.084	0.00144	203.49	0.049	0.052	0.052	3.17
490	0.007	0.197	0.00225	244.97	0.153	0.227	0.034	4.46
553	0.008	0.251	0.00251	276.46	0.243	0.470	0.030	5.80
589	0.014	0.321	0.00453	294.44	0.226	0.469	0.042	6.19
629	0.030	0.296	0.01005	314.44	0.362	0.530	0.102	4.39
681	0.009	0.142	0.00288	340.47	0.288	0.403	0.061	4.19
726	0.029	0.302	0.00982	362.94	0.236	0.264	0.098	3.35
781	0.007	0.182	0.00242	390.47	0.259	0.376	0.040	4.36
812	0.018	0.370	0.00595	405.93	0.240	0.365	0.048	4.57
862	0.028	0.321	0.00939	430.94	0.323	0.450	0.088	4.18
892	0.023	0.125	0.00750	445.97	0.116	0.083	0.180	2.15
957	0.046	0.391	0.01537	478.42	0.271	0.249	0.118	2.76
994	0.016	0.159	0.00543	496.97	0.082	0.086	0.102	3.14
1036	0.009	0.145	0.00314	517.97	0.162	0.198	0.065	3.65
1060	0.018	0.290	0.00589	529.95	0.279	0.325	0.061	3.49
1129	0.002	0.059	0.00073	564.49	0.065	0.114	0.037	5.26
1179	0.010	0.134	0.00320	589.48	0.064	0.068	0.072	3.20
1237	0.044	0.343	0.01476	618.43	0.167	0.132	0.129	2.36
1294	0.026	0.164	0.00881	646.97	0.095	0.062	0.162	1.96
1305	0.022	0.246	0.00735	652.45	0.156	0.158	0.090	3.05
1345	0.033	0.286	0.01106	672.45	0.185	0.170	0.116	2.75
1423	0.051	0.358	0.01715	0.19	0.075	0.044	0.144	1.76
1469	0.029	0.310	0.00983	734.44	0.107	0.108	0.095	3.03
1520	0.229	1.283	0.07626	0.66	0.520	0.451	0.178	2.60
1594	0.030	0.380	0.01006	796.93	0.247	0.291	0.079	3.53
1672	0.021	0.277	0.00705	835.95	0.143	0.170	0.076	3.58
1730	0.034	0.335	0.01144	864.94	0.218	0.216	0.102	2.98
1780	0.102	0.824	0.03415	1027.42	0.209	0.178	0.124	2.56
1810	0.074	0.357	0.02467	904.92	0.200	0.119	0.208	1.79
1915	0.030	0.169	0.01002	957.47	0.297	0.199	0.178	2.02
1995	0.040	0.373	0.01320	997.43	0.269	0.309	0.106	3.45
2070	0.012	0.057	0.00415	1034.99	0.037	0.020	0.220	1.67
2097	0.023	0.194	0.00769	1048.46	0.272	0.256	0.119	2.83
2131	0.076	0.416	0.02546	0.21	0.283	0.199	0.184	2.11
2158	0.139	0.636	0.04644	0.32	0.247	0.142	0.219	1.72
2250	0.044	0.186	0.01466	1124.96	0.085	0.042	0.236	1.48

Appendix D: NRM Data

Sample	Dec.	Inc.	mA/m	Demagnetization Temperature (C)
10	230.6	66.0	693.5	NRM
72	173.8	60.8	637.2	NRM
151	162.2	45.7	472.2	NRM
187	228.7	64.2	1555.8	NRM
224	194.9	75.3	2341.0	NRM
250	133.4	77.0	3828.7	NRM
297	301.1	68.4	1105.8	NRM
349	84.4	65.9	1497.4	NRM
382	60.6	83.4	1421.6	NRM
407	102.5	51.7	1946.7	NRM
490	151.5	59.1	1773.9	NRM
553	128.4	73.1	1622.5	NRM
589	310.7	49.2	2818.7	NRM
629	105.3	21.2	1165.2	NRM
681	188.6	25.8	2692.4	NRM
726	356.2	23.0	761.0	NRM
781	209.7	25.2	1680.4	NRM
812	113.0	29.6	1560.7	NRM
862	62.9	38.9	605.3	NRM
892	261.2	22.0	1455.5	NRM
957	81.4	27.2	1323.7	NRM
994	0.4	23.9	854.8	NRM
1036	83.2	32.6	670.0	NRM
1060	154.3	41.5	844.7	NRM
1129	248.9	50.1	511.6	NRM
1179	80.2	18.5	609.9	NRM
1237	158.0	22.4	1286.6	NRM
1294	24.2	36.0	4613.7	NRM
1305	324.1	25.6	222.1	NRM
1345	263.8	15.2	191.0	NRM
1423	232.7	27.5	470.6	NRM
1469	318.5	13.3	959.3	NRM
1520	245.2	10.8	657.6	NRM
1594	341.2	25.5	381.9	NRM
1672	113.8	21.7	440.6	NRM
1730	303.6	30.3	703.8	NRM
1780	309.7	23.8	263.0	NRM
1810	118.7	34.2	1348.7	NRM
1915	326.1	34.0	505.9	NRM
1995	4.5	24.4	98.9	NRM
2070	205.2	22.5	333.9	NRM
2097	317.5	28.8	36.2	NRM
2131	63.1	42.3	307.4	NRM
2158	15.1	26.6	515.3	NRM
2250	7.6	39.9	6967.6	NRM

Appendix D: NRM Data

Sample	Dec.	Inc.	mA/m	Demagnetization Temperature (C)
10	252.0	62.0	401	LTD
72	199.0	69.0	251	LTD
151	181.0	53.0	349	LTD
187	252.0	42.0	877	LTD
224	228.0	54.0	974	LTD
250	139.0	69.0	1110	LTD
297	327.0	56.0	613	LTD
349	63.0	39.0	592	LTD
382	59.0	57.0	362	LTD
407	82.0	28.0	1296	LTD
490	137.0	49.0	898	LTD
553	50.0	64.0	517	LTD
589	310.0	23.0	1563	LTD
629	100.0	21.0	969	LTD
681	191.0	25.0	2220	LTD
726	354.0	23.0	621	LTD
781	212.0	20.0	1296	LTD
812	114.0	27.0	1303	LTD
862	63.0	38.0	527	LTD
892	262.0	21.0	1281	LTD
957	83.0	28.0	1156	LTD
994	6.0	24.0	753	LTD
1036	79.0	32.0	564	LTD
1060	149.0	31.0	594	LTD
1129	268.0	38.0	262	LTD
1179	72.0	25.0	545	LTD
1237	157.0	20.0	1135	LTD
1294	25.0	37.0	3990	LTD
1305	317.0	26.0	186	LTD
1345	262.0	14.0	179	LTD
1423	230.0	27.0	4540	LTD
1469	318.0	12.0	902	LTD
1520	242.0	10.0	659	LTD
1594	339.0	23.0	350	LTD
1672	109.0	19.0	394	LTD
1730	300.0	27.0	607	LTD
1780	312.0	22.0	245	LTD
1810	114.0	32.0	1288	LTD
1915	323.0	28.0	505	LTD
1995	6.0	21.0	105	LTD
2070	199.0	23.0	341	LTD
2097	314.0	28.0	35	LTD
2131	58.0	40.0	308	LTD
2158	15.0	26.0	528	LTD
2250	2.0	33.0	6080	LTD

Appendix D: NRM Data

Sample	Dec.	Inc.	mA/m	Demagnetization Temperature (C)
10	256.4	45.9	359.4	100
72	147.7	25.0	333.2	100
151	171.7	51.5	306.5	100
187	314.4	16.2	661.7	100
224	197.6	8.2	1042.8	100
250	153.3	82.6	1399.3	100
297	311.2	12.3	456.9	100
349	47.0	42.6	757.4	100
382	68.8	5.0	259.1	100
407	61.2	28.9	1300.1	100
490	91.8	22.3	564.8	100
553	31.8	5.3	549.3	100
589	316.7	4.8	1263.0	100
629	102.7	20.1	995.8	100
681	192.1	28.8	2167.4	100
726	355.7	22.9	628.0	100
781	216.1	19.6	137.9	100
812	116.0	25.4	1277.2	100
862	64.3	39.3	526.6	100
892	264.9	14.5	1166.5	100
957	79.6	27.5	1170.1	100
994	5.1	24.3	755.5	100
1036	85.3	29.2	522.4	100
1060	164.3	4.8	601.0	100
1129	289.2	-75.8	610.3	100
1179	70.8	19.0	511.8	100
1237	148.1	6.3	1104.4	100
1294	33.2	35.1	4051.7	100
1305	319.6	25.6	177.8	100
1345	260.6	11.9	161.9	100
1423	234.2	26.1	4314.0	100
1469	319.9	11.9	829.9	100
1520	243.4	6.5	618.9	100
1594	343.1	22.2	327.7	100
1672	108.3	19.5	362.0	100
1730	303.9	28.5	582.3	100
1780	312.7	21.9	227.7	100
1810	119.0	38.2	1391.4	100
1915	326.9	27.8	467.2	100
1995	7.5	22.3	98.0	100
2070	202.9	21.4	325.0	100
2097	315.2	27.6	35.8	100
2131	61.8	43.8	280.5	100
2158	13.8	24.1	500.9	100
2250	13.0	30.0	6046.9	100

Appendix D: NRM Data

Sample	Dec.	Inc.	mA/m	Demagnetization Temperature (C)
10	261.9	47.3	424.9	120
72	171.7	12.6	246.3	120
151	170.0	48.1	447.3	120
187	290.9	13.9	681.5	120
224	191.7	13.2	1193.5	120
250	359.5	74.8	1180.3	120
297	299.5	20.4	593.5	120
349	47.0	19.5	699.8	120
382	54.5	4.8	199.4	120
407	54.9	12.3	911.4	120
490	73.2	43.8	649.9	120
553	26.9	46.3	427.7	120
589	281.8	19.1	1105.8	120
629	100.8	20.2	951.6	120
681	191.8	25.1	2171.3	120
726	356.4	23.4	622.2	120
781	214.8	19.2	1368.5	120
812	112.5	26.2	1257.1	120
862	63.7	38.1	531.7	120
892	260.7	15.4	1179.2	120
957	82.4	27.5	1157.7	120
994	7.5	23.6	758.5	120
1036	84.6	31.1	529.2	120
1060	161.0	-8.5	586.4	120
1129	301.1	-55.4	351.4	120
1179	79.3	23.2	535.0	120
1237	146.0	12.5	1130.4	120
1294	31.8	37.2	3927.4	120
1305	318.0	25.6	186.5	120
1345	261.6	11.1	161.5	120
1423	233.3	25.8	4673.0	120
1469	320.5	12.0	830.6	120
1520	243.6	8.4	611.4	120
1594	345.2	27.0	332.5	120
1672	110.0	21.3	376.0	120
1730	305.6	30.4	565.5	120
1780	313.6	23.1	225.3	120
1810	118.2	33.4	1504.8	120
1915	331.5	21.9	427.4	120
1995	6.4	23.4	97.7	120
2070	205.5	18.4	331.0	120
2097	319.3	28.7	32.0	120
2131	56.9	40.4	295.0	120
2158	16.8	25.8	502.6	120
2250	14.7	31.9	6038.9	120

Appendix D: NRM Data

Sample	Dec.	Inc.	mA/m	Demagnetization Temperature (C)
10	264.0	52.0	2847.2	140
72	182.9	31.7	2718.1	140
151	193.5	50.3	445.0	140
187	272.8	20.1	568.6	140
224	211.5	40.6	1870.1	140
250	9.4	77.4	7125.0	140
297	321.7	44.5	616.7	140
349	58.8	33.2	661.0	140
382	58.1	6.5	1081.5	140
407	49.6	45.0	855.5	140
490	70.7	43.1	677.1	140
553	43.6	51.6	414.8	140
589	276.3	17.1	5846.1	140
629	98.8	19.2	963.4	140
681	193.9	24.6	14143.1	140
726	356.9	23.6	621.4	140
781	213.7	16.2	1399.1	140
812	111.6	26.3	1249.5	140
862	63.2	37.4	527.9	140
892	257.5	15.8	1196.0	140
957	81.3	25.8	1181.3	140
994	3.1	24.7	750.7	140
1036	80.5	35.8	530.2	140
1060	143.9	-6.5	4593.8	140
1129	286.8	-61.1	1954.6	140
1179	78.7	17.7	3077.2	140
1237	146.7	12.2	7705.1	140
1294	28.8	39.9	24862.6	140
1305	317.3	26.6	1182.6	140
1345	260.1	13.8	162.2	140
1423	233.3	27.7	29413.6	140
1469	320.4	12.5	5225.9	140
1520	245.1	8.2	3921.3	140
1594	340.2	25.3	2146.6	140
1672	109.5	20.3	372.5	140
1730	303.7	30.7	3652.9	140
1780	314.4	22.8	1500.2	140
1810	115.4	21.6	8110.8	140
1915	326.5	29.6	3036.9	140
1995	8.9	23.3	629.4	140
2070	204.2	20.7	2084.4	140
2097	319.3	27.4	219.8	140
2131	59.1	41.6	1810.6	140
2158	16.9	24.9	3183.8	140
2250	11.5	36.1	41892.6	140

Appendix D: NRM Data

Sample	Dec.	Inc.	mA/m	Demagnetization Temperature (C)
10	262.2	63.1	500.2	160
72	197.3	37.9	365.5	160
151	201.8	52.2	428.7	160
187	248.6	52.5	1443.7	160
224	214.5	43.3	1764.4	160
250	28.2	77.2	802.8	160
297	316.0	41.5	502.4	160
349	59.5	31.9	608.4	160
382	57.2	27.1	304.7	160
407	56.5	33.1	758.6	160
490	94.6	22.4	604.9	160
553	106.1	82.9	563.3	160
589	301.6	4.1	1167.4	160
629	97.2	20.7	956.1	160
681	189.9	25.7	2160.9	160
726	356.8	24.7	616.9	160
781	212.5	17.3	1437.4	160
812	111.6	27.4	1224.0	160
862	62.4	38.4	513.6	160
892	260.5	15.7	1176.9	160
957	80.7	28.5	1151.9	160
994	3.5	24.7	750.8	160
1036	80.5	32.0	519.9	160
1060	149.0	-4.6	649.2	160
1129	304.5	-44.0	255.5	160
1179	72.1	18.0	608.2	160
1237	147.6	12.6	1172.2	160
1294	27.9	38.7	3939.4	160
1305	316.8	26.5	180.8	160
1345	256.5	8.9	160.5	160
1423	232.6	27.0	4627.8	160
1469	317.6	13.7	809.9	160
1520	242.3	6.3	618.1	160
1594	340.4	25.4	333.4	160
1672	110.7	20.0	374.3	160
1730	302.2	29.8	566.3	160
1780	312.4	22.0	227.5	160
1810	125.0	29.1	1274.5	160
1915	323.2	30.0	465.3	160
1995	6.2	22.2	97.8	160
2070	202.7	21.1	322.6	160
2097	315.8	28.0	34.5	160
2131	56.5	40.8	286.6	160
2158	15.1	25.9	494.9	160
2250	8.8	33.9	6275.0	160

Appendix D: NRM Data

Sample	Dec.	Inc.	mA/m	Demagnetization Temperature (C)
10	252.2	59.2	432.2	180
72	201.5	20.6	299.8	180
151	198.7	48.5	424.0	180
187	259.9	30.4	1134.6	180
224	194.8	41.0	1841.7	180
250	22.8	70.9	643.5	180
297	324.3	38.4	634.3	180
349	74.0	48.5	1132.8	180
382	67.9	47.1	265.1	180
407	62.6	24.4	661.4	180
490	92.0	8.2	713.7	180
553	9.2	72.6	463.5	180
589	303.0	0.3	927.9	180
629	98.1	19.8	961.2	180
681	191.4	24.9	2164.4	180
726	354.0	23.8	624.1	180
781	213.8	16.7	1339.3	180
812	114.4	27.0	1262.7	180
862	61.9	38.6	520.6	180
892	261.3	16.8	1196.2	180
957	76.4	26.5	1171.7	180
994	1.8	23.9	751.9	180
1036	78.5	30.6	525.8	180
1060	156.7	13.4	708.8	180
1129	282.0	-39.9	254.7	180
1179	78.4	20.1	590.3	180
1237	146.3	14.8	1109.3	180
1294	43.7	53.9	3309.2	180
1305	318.9	25.1	184.1	180
1345	259.1	9.2	159.7	180
1423	231.3	26.4	4625.0	180
1469	316.1	14.2	766.1	180
1520	239.1	6.6	641.0	180
1594	340.4	26.5	326.1	180
1672	106.2	17.9	369.2	180
1730	297.1	30.5	557.3	180
1780	312.8	22.5	234.3	180
1810	118.3	34.0	1236.7	180
1915	323.9	31.3	456.5	180
1995	6.8	22.9	98.0	180
2070	197.0	16.0	304.2	180
2097	312.3	28.1	34.5	180
2131	58.4	42.3	285.4	180
2158	15.0	25.9	502.4	180
2250	12.2	42.0	5981.0	180

Appendix D: NRM Data

Sample	Dec.	Inc.	mA/m	Demagnetization Temperature (C)
10	262.6	62.7	436.1	200
72	177.1	31.5	278.0	200
151	206.9	44.3	408.7	200
187	258.6	29.6	1202.8	200
224	193.1	39.8	1546.1	200
250	128.5	66.7	1082.4	200
297	318.9	43.5	595.1	200
349	74.0	31.9	815.2	200
382	55.6	80.0	439.7	200
407	69.2	24.5	951.8	200
490	108.2	68.6	2155.0	200
553	35.9	75.0	728.8	200
589	308.1	3.2	956.1	200
629	98.3	20.4	959.5	200
681	192.0	25.1	2169.9	200
726	355.5	23.0	627.0	200
781	214.5	20.7	1326.1	200
812	111.9	27.6	1268.4	200
862	66.9	39.1	509.6	200
892	261.1	17.6	1201.1	200
957	79.0	25.8	1167.9	200
994	3.6	23.4	758.4	200
1036	73.1	28.0	532.5	200
1060	160.4	10.8	699.7	200
1129	276.5	-17.8	222.6	200
1179	78.2	18.7	613.5	200
1237	151.2	13.0	1129.7	200
1294	31.1	43.6	3952.2	200
1305	319.5	26.0	182.5	200
1345	262.4	11.6	160.6	200
1423	234.0	28.7	4515.0	200
1469	318.9	13.1	850.4	200
1520	244.0	7.9	622.3	200
1594	340.4	19.9	330.4	200
1672	113.6	17.9	375.1	200
1730	304.2	30.5	567.0	200
1780	313.3	21.9	237.5	200
1810	126.1	30.6	1307.2	200
1915	317.3	29.4	515.1	200
1995	7.4	21.3	98.5	200
2070	196.1	15.3	308.2	200
2097	312.9	30.9	36.6	200
2131	58.0	40.9	290.8	200
2158	17.5	25.6	501.7	200
2250	14.5	38.8	5975.9	200

Appendix D: NRM Data

Sample	Dec.	Inc.	mA/m	Demagnetization Temperature (C)
10	253.7	58.5	343.0	300
72	205.2	47.2	244.0	300
151	192.9	41.0	203.4	300
187	258.0	68.2	1996.4	300
224	194.3	48.0	1287.7	300
250	152.6	58.2	1208.1	300
297	312.9	46.0	503.6	300
349	60.7	28.4	513.7	300
382	290.5	-36.9	44.3	300
407	79.7	8.0	1220.6	300
490	102.4	36.8	925.9	300
553	201.5	76.1	1552.0	300
589	324.4	4.8	922.9	300
629	97.8	20.1	949.0	300
681	190.5	27.6	2135.3	300
726	354.8	23.0	622.1	300
781	210.9	17.2	1192.3	300
812	110.6	27.0	1264.6	300
862	63.0	36.5	533.0	300
892	255.8	17.8	1225.6	300
957	79.6	27.1	1160.5	300
994	2.4	24.1	745.3	300
1036	73.4	27.9	542.6	300
1060	86.0	81.3	1442.8	300
1129	272.1	-12.9	153.5	300
1179	78.1	23.7	508.5	300
1237	153.5	13.2	1127.8	300
1294	28.7	41.5	3984.2	300
1305	317.9	26.0	179.3	300
1345	260.2	16.8	167.7	300
1423	232.9	26.4	4403.5	300
1469	318.3	13.4	839.2	300
1520	242.9	8.7	611.5	300
1594	341.3	24.2	323.2	300
1672	113.2	17.5	384.7	300
1730	302.3	29.4	561.8	300
1780	312.6	23.0	233.7	300
1810	119.0	31.1	1258.2	300
1915	319.5	29.3	460.5	300
1995	4.6	21.3	96.7	300
2070	198.2	18.9	297.8	300
2097	316.0	26.7	35.2	300
2131	60.8	42.6	282.7	300
2158	17.9	26.0	496.9	300
2250	10.0	38.1	5696.0	300

Appendix D: NRM Data

Sample	Dec.	Inc.	mA/m	Demagnetization Temperature (C)
10	254.8	54.7	353.3	350
72	144.3	48.9	245.2	350
151	201.2	55.7	358.9	350
187	245.9	38.0	1094.0	350
224	258.2	77.7	2659.6	350
250	117.0	69.4	590.4	350
297	324.0	37.2	424.9	350
349	64.8	30.8	482.8	350
382	87.4	-64.9	1215.7	350
407	77.5	12.8	761.3	350
490	121.8	51.7	1113.1	350
553	17.1	8.7	392.1	350
589	304.2	33.8	1303.0	350
629	96.4	20.5	949.4	350
681	192.3	25.7	2178.5	350
726	352.4	22.9	626.4	350
781	199.0	45.6	2062.3	350
812	112.1	28.2	1271.0	350
862	63.2	38.3	519.8	350
892	259.6	19.1	1218.8	350
957	78.0	29.1	1206.7	350
994	3.4	23.8	763.6	350
1036	76.3	28.0	523.4	350
1060	157.5	43.0	708.8	350
1129	272.0	-9.8	194.5	350
1179	72.6	22.9	560.5	350
1237	151.2	15.6	1095.2	350
1294	26.8	40.6	4032.8	350
1305	316.4	25.7	178.2	350
1345	260.3	13.3	163.0	350
1423	231.3	26.8	4504.6	350
1469	320.5	13.8	862.4	350
1520	238.9	7.7	636.7	350
1594	339.8	24.4	334.1	350
1672	111.2	18.7	378.2	350
1730	302.8	29.0	574.9	350
1780	310.8	21.9	232.3	350
1810	122.0	27.0	1243.6	350
1915	320.3	27.3	481.5	350
1995	4.1	24.0	97.6	350
2070	198.0	18.2	296.7	350
2097	316.1	26.5	34.0	350
2131	63.0	42.1	283.4	350
2158	16.6	26.8	500.3	350
2250	8.4	35.5	5499.9	350

Appendix D: NRM Data

Sample	Dec.	Inc.	mA/m	Demagnetization Temperature (C)
10	258.0	54.2	278.8	400
72	166.3	54.1	188.8	400
151	178.4	40.3	323.2	400
187	253.7	31.6	881.2	400
224	218.6	59.4	1122.0	400
250	133.6	66.3	964.7	400
297	308.4	36.9	447.3	400
349	72.2	34.6	502.9	400
382	107.5	51.2	252.7	400
407	79.1	20.0	918.2	400
490	126.7	82.6	2647.5	400
553	309.0	83.6	361.9	400
589	315.3	8.5	1169.4	400
629	101.0	20.2	946.9	400
681	193.7	23.9	2231.7	400
726	354.1	22.6	626.3	400
781	220.3	29.7	1147.6	400
812	111.8	28.4	1250.7	400
862	64.9	38.0	525.9	400
892	259.4	19.0	1226.4	400
957	83.0	28.4	1191.5	400
994	4.6	24.4	756.7	400
1036	76.7	28.0	535.6	400
1060	161.5	58.6	1904.5	400
1129	295.3	17.0	173.7	400
1179	77.1	46.1	882.6	400
1237	151.2	14.6	1108.0	400
1294	24.7	41.0	3892.9	400
1305	314.7	26.0	178.9	400
1345	262.6	14.9	162.1	400
1423	232.8	25.9	4466.8	400
1469	317.7	13.9	854.5	400
1520	243.3	9.3	553.1	400
1594	339.1	24.0	345.7	400
1672	110.3	16.1	375.6	400
1730	302.2	32.5	599.8	400
1780	311.8	24.4	236.2	400
1810	123.4	29.9	1199.5	400
1915	321.8	24.8	452.0	400
1995	8.1	22.3	97.8	400
2070	199.8	18.5	294.8	400
2097	315.4	27.2	34.0	400
2131	59.7	39.5	290.5	400
2158	16.6	25.0	503.5	400
2250	11.1	35.3	5445.7	400

Appendix D: NRM Data

Sample	Dec.	Inc.	mA/m	Demagnetization Temperature (C)
10	249.6	55.6	218.9	450
72	215.9	42.8	120.9	450
151	198.9	58.2	368.1	450
187	259.5	36.4	726.1	450
224	229.6	54.2	964.5	450
250	134.2	27.6	479.5	450
297	332.6	47.2	349.2	450
349	64.5	23.6	562.0	450
382	59.1	24.1	240.8	450
407	79.6	20.4	1026.7	450
490	122.0	51.4	952.4	450
553	29.4	30.9	400.3	450
589	311.0	10.9	1617.1	450
629	99.6	18.1	947.2	450
681	193.0	25.4	2188.0	450
726	357.5	22.1	605.8	450
781	209.6	19.2	1257.3	450
812	105.2	29.5	1217.9	450
862	63.2	36.8	524.3	450
892	261.2	19.3	1235.2	450
957	84.5	26.5	1185.4	450
994	5.0	25.3	752.3	450
1036	77.0	29.1	542.8	450
1060	176.6	64.3	2166.9	450
1129	284.3	1.1	147.2	450
1179	72.1	24.3	574.3	450
1237	154.9	28.7	1179.5	450
1294	30.0	40.2	3936.0	450
1305	320.4	22.9	178.6	450
1345	265.7	13.1	159.4	450
1423	231.5	27.3	4371.5	450
1469	317.1	13.7	805.7	450
1520	242.7	8.8	559.1	450
1594	340.6	23.5	334.9	450
1672	113.2	19.8	388.9	450
1730	304.2	29.2	574.4	450
1780	308.4	22.4	230.5	450
1810	121.2	32.3	1268.4	450
1915	322.9	25.5	425.8	450
1995	9.2	20.5	93.4	450
2070	202.2	8.6	263.5	450
2097	317.7	27.3	35.6	450
2131	61.2	41.0	280.6	450
2158	15.6	25.8	468.6	450
2250	8.8	33.3	5345.8	450

Appendix D: NRM Data

Sample	Dec.	Inc.	mA/m	Demagnetization Temperature (C)
10	261.3	59.5	204.2	475
72	213.5	3.9	117.6	475
151	192.0	47.7	184.0	475
187	253.4	18.8	808.7	475
224	227.1	48.2	539.7	475
250	19.1	-34.5	828.5	475
297	343.0	44.5	320.0	475
349	79.2	-34.5	689.3	475
382	182.0	77.7	387.1	475
407	73.2	77.4	3368.6	475
490	126.9	55.9	681.5	475
553	339.0	1.8	114.9	475
589	326.2	3.1	1491.2	475
629	98.7	21.1	944.5	475
681	191.2	25.4	2211.1	475
726	359.4	23.7	600.1	475
781	223.9	68.8	2437.3	475
812	116.5	25.0	1321.4	475
862	63.4	37.7	528.1	475
892	259.0	18.6	1216.7	475
957	84.4	26.5	1177.1	475
994	8.0	27.0	781.5	475
1036	73.7	28.3	538.7	475
1060	161.5	40.9	765.7	475
1129	280.1	71.7	1026.7	475
1179	74.5	21.7	602.1	475
1237	153.3	17.2	1101.3	475
1294	27.6	41.1	3944.1	475
1305	318.9	25.9	173.0	475
1345	257.7	12.4	162.3	475
1423	233.7	25.3	4420.2	475
1469	318.4	14.1	855.5	475
1520	240.2	6.8	558.0	475
1594	338.3	24.4	340.5	475
1672	109.4	19.0	372.1	475
1730	304.4	28.9	595.5	475
1780	311.5	22.6	233.0	475
1810	121.3	29.6	1106.6	475
1915	323.4	27.3	434.2	475
1995	7.9	22.5	94.7	475
2070	198.0	15.6	259.1	475
2097	314.6	25.0	31.2	475
2131	59.2	40.9	273.8	475
2158	16.3	26.6	474.4	475
2250	18.0	38.6	5522.5	475

Appendix D: NRM Data

Sample	Dec.	Inc.	mA/m	Demagnetization Temperature (C)
10	224.1	70.2	425.7	500
72	308.4	54.8	30.0	500
151	168.2	37.2	245.7	500
187	271.3	13.9	595.2	500
224	224.3	64.2	2715.2	500
250	127.4	45.4	577.7	500
297	328.2	48.7	373.3	500
349	62.9	15.5	532.3	500
382	52.5	78.7	301.6	500
407	73.0	14.3	995.0	500
490	125.9	46.9	762.0	500
553	358.6	-22.7	142.8	500
589	314.2	25.7	1301.0	500
629	99.2	19.4	940.0	500
681	194.1	23.3	2212.5	500
726	356.6	22.3	601.5	500
781	206.3	55.9	2179.9	500
812	115.2	28.2	1232.6	500
862	67.2	38.5	521.6	500
892	256.9	19.4	1226.4	500
957	80.6	26.3	1173.3	500
994	3.3	25.0	738.4	500
1036	75.8	34.5	615.0	500
1060	153.6	56.0	704.6	500
1129	272.0	37.8	213.2	500
1179	72.9	24.2	535.1	500
1237	150.3	13.3	1030.8	500
1294	26.2	41.3	3957.1	500
1305	318.1	25.6	170.5	500
1345	262.2	13.8	156.4	500
1423	235.6	25.8	4189.6	500
1469	319.3	13.5	830.6	500
1520	237.1	7.4	564.2	500
1594	338.1	29.3	367.9	500
1672	106.1	18.3	352.5	500
1730	303.3	30.6	573.8	500
1780	308.1	22.2	223.6	500
1810	116.0	28.8	1041.0	500
1915	321.6	28.3	427.3	500
1995	9.3	19.7	90.8	500
2070	197.4	14.6	245.6	500
2097	315.3	26.1	31.1	500
2131	57.5	42.4	254.5	500
2158	14.6	24.5	479.4	500
2250	17.2	33.3	5249.9	500

Appendix D: NRM Data

Sample	Dec.	Inc.	mA/m	Demagnetization Temperature (C)
10	258.1	62.1	189.4	525
72	61.9	70.9	100.3	525
151	191.2	49.6	170.3	525
187	251.9	34.9	795.0	525
224	207.8	78.6	2613.3	525
250	145.3	62.5	221.6	525
297	321.0	35.6	356.2	525
349	62.5	9.4	597.3	525
382	36.5	-17.9	99.4	525
407	61.8	14.3	985.8	525
490	109.5	24.1	570.1	525
553	13.7	88.0	2406.6	525
589	310.6	13.1	1724.5	525
629	103.0	19.3	908.8	525
681	191.1	25.2	2164.8	525
726	354.8	22.4	598.1	525
781	219.2	24.2	1179.5	525
812	114.2	24.8	1262.0	525
862	62.1	37.3	528.7	525
892	262.0	17.5	1190.1	525
957	82.9	30.2	1194.3	525
994	4.3	22.5	733.6	525
1036	74.0	28.2	563.2	525
1060	153.4	41.9	648.5	525
1129	290.2	16.6	171.5	525
1179	73.3	23.0	538.4	525
1237	152.0	15.7	1067.1	525
1294	25.9	38.9	3741.6	525
1305	317.1	26.0	167.4	525
1345	255.8	14.2	158.3	525
1423	232.1	26.2	4261.5	525
1469	319.9	12.0	829.1	525
1520	239.6	9.4	552.5	525
1594	340.2	28.2	355.9	525
1672	108.5	18.9	376.2	525
1730	303.4	28.3	580.7	525
1780	301.0	22.3	208.9	525
1810	112.1	29.7	929.1	5[illegible]
1915	320.8	28.5	425.8	[illegible]25
1995	9.7	22.2	85.0	525
2070	196.9	15.3	241.6	525
2097	314.0	27.2	30[illegible]	525
2131	55.5	42.4	224.8	525
2158	15.2	24.3	487.3	525
2250	13.0	34.2	5201.7	525

Appendix D: NRM Data

Sample	Dec.	Inc.	mA/m	Demagnetization Temperature (C)
10	256.7	67.2	182.0	550
72	99.2	-39.8	94.7	550
151	167.0	47.5	288.5	550
187	253.2	35.1	935.6	550
224	214.8	60.3	1089.6	550
250	118.0	32.4	460.7	550
297	337.4	46.4	284.5	550
349	97.4	63.0	1209.9	550
382	66.4	6.2	194.8	550
407	68.6	3.9	747.9	550
490	118.2	22.8	497.1	550
553	8.5	27.4	180.1	550
589	301.2	20.6	1199.4	550
629	98.0	20.5	865.5	550
681	191.8	24.1	2180.1	550
726	354.9	22.6	596.1	550
781	214.5	19.5	1258.4	550
812	119.4	27.4	1270.9	550
862	61.3	38.7	523.5	550
892	260.9	20.1	1207.4	550
957	81.0	27.6	1159.1	550
994	2.0	29.5	755.7	550
1036	77.9	29.0	550.7	550
1060	156.7	27.7	467.9	550
1129	288.7	14.0	144.9	550
1179	76.5	24.7	510.7	550
1237	151.3	13.9	1087.3	550
1294	26.5	37.6	3837.6	550
1305	320.5	35.6	186.7	550
1345	257.1	13.1	136.7	550
1423	234.4	25.5	3987.6	550
1469	320.3	15.1	796.5	550
1520	239.9	8.4	546.6	550
1594	338.3	25.1	331.2	550
1672	110.2	18.9	351.3	550
1730	305.0	30.3	562.5	550
1780	309.1	23.9	224.0	550
1810	109.5	33.0	919.5	550
1915	327.2	26.2	391.9	550
1995	9.9	22.6	76.0	550
2070	196.8	16.2	196.0	550
2097	313.0	25.9	25.2	550
2131	62.9	43.6	238.6	550
2158	15.0	26.2	478.1	550
2250	13.8	31.5	5125.0	550